Computational and Experimental Study of Structure-Property Relationships in NiAl Precipitate-Strengthened Ferritic Superalloys

A Dissertation Presented for the
Doctor of Philosophy
Degree
The University of Tennessee, Knoxville

Shenyan Huang
December 2011

DEDICATION

This dissertation is dedicated to my mother and father, Xin Dai and Yi Huang, who always love, understand, and encourage me under any circumstances. Their endless support helped me keep strong through stressful times. They are proud of me for becoming the first female doctorate in our big families of Huang, Dai, Sun, and Wang.

ACKNOWLEDGEMENTS

I want to pay my sincere gratitudes to all those who helped me complete the Ph.D. degree in Materials Science and Engineering. I would like to thank my academic advisor Prof. Peter Liaw for his instructions on my graduate study and guidance on my professional career. I am grateful to Profs. Yanfei Gao and James Morris for their helpful discussions and suggestions on my dissertation work. I greatly appreciate the guidance on first-principles calculations from Prof. Mark Asta at University of California, Berkeley. I'd like to thank Dr. Edward Kenik for helping me characterize the particle-dislocation interactions by TEM through the SHARE program at Oak Ridge National Laboratory. The completion of this work would not be possible without the help from Dr. Xin Li at University of Indiana for instructions in small-angle scattering modeling, Dr. Gongyao Wang for his tutoring on mechanical testing, Dr. Zhenke Teng for the sample preparation and teamwork in writing journal papers/progress reports/proposals, Dr. Lili Zheng for her tutoring on finite element simulation, Prof. Claudia Rawn for sharing the high-temperature furnace in her laboratory, Prof. Carl Lundin for allowing me to use the dead-load creep frames, the machine shop members, Doug Fielden, Larry Smith, and Danny Hackworth, for their help on sample machining.

This work was financially supported by the U.S. Department of Energy (DOE), Office of Fossil Energy, under Grant No. DE-FG26-06NT42732, DE-09NT0008089, and DE-FE0005868. The use of the Advanced Photon Source, an Office of Science User Facility operated for the U.S. Department of Energy Office of Science by the Argonne National Laboratory, was supported by the U.S. DOE under Contract No. DE-AC02-06CH11357. The work has benefitted from the use of the Lujan Neutron Scattering Center at Los Alamos Neutron Science Center (LANSCE) which is funded by the Office of Basic Energy Sciences (DOE). Los Alamos National Laboratory is operated by the Los Alamos National Security LLC under the DOE contract of DE-AC52-06NA-25396. A portion of this Research at the Oak Ridge National Laboratory's Spallation Neutron Source was sponsored by the Scientific User Facilities Division, Office of Basic Energy Sciences, U.S. Department of Energy. I am grateful to Profs. Morris Fine, Gautam Ghosh, and David Dunand at Northwestern University, Prof. Mark Asta at the University of California, Berkeley, and Prof. Chain T. Liu at the City University of Hong Kong for their collaborations in these DOE programs.

ABSTRACT

Ferritic superalloys strengthened by coherent ordered NiAl *B2*-type precipitates are promising candidates for ultra-supercritical steam-turbine applications, due to their superior resistance to creep, coarsening, oxidation, and steam corrosion as compared to Cr ferritic steels at high temperatures. Combined computational and experimental tools have been employed to investigate the interrelationships among the composition, microstructure, and mechanical behavior, and provide insight into deformation micromechanisms at elevated temperatures.

Self and impurity diffusivities in a body-centered-cubic (bcc) iron are calculated using first-principles methods. Calculated self and impurity diffusivities compare favorably with experimental measurements in both ferromagnetic and paramagnetic states of bcc Fe. The calculated impurity diffusivities of W and Mo are larger than the self diffusivity of Fe, mainly owing to the lower activation energies.

The microstructural attributes of NiAl-type *B*2 precipitates are investigated in several designed ferritic superalloys. Ultra-small-angle X-ray scattering in conjunction with transmission electron microscopy is employed to quantify the average size, size distribution, inter-particle spacing, and volume fraction of the primary precipitates. It is observed that as the Al amount increases from 4 to 10 mass%, there is a decrease in the average inter-particle spacing and average particle diameter. An alloy with 6.5 weight percent Al exhibits the optimal creep resistance and an associated maximum Orowan stress at 973 K. The dislocations-particle interaction mode during the secondary creep regime is identified as a combination of Orowan looping and dislocation climb.

In-situ neutron diffraction experiments during tensile and creep deformations reveal the intergranular and interphase load-sharing mechanisms during plastic deformation at elevated temperatures. The change of deformation mechanisms from dislocation slip below 773 K to power-law creep above 873 K is well captured by the evolution of the different lattice strains. High-temperature deformation above 873 K is possibly assisted by the relaxation processes, e.g., grain-boundary sliding and/or diffusional flow along grain boundaries and matrix-particle interfaces. The evolution of lattice strains during high-temperature deformation is further verified by crystal-plasticity finite-element simulations.

The significant findings in the present work provide the crucial baseline information for further alloy optimization and improvement in high-temperature creep resistance of ferritic superalloys.

TABLE OF CONTENTS

LIST OF TABLES

LIST OF FIGURES

CHAPTER I
INTRODUCTION

Currently, the operating temperature of fossil energy power plants in US is below 943 K. The thermal efficiency of energy conversion from burning coal to electricity can be improved by more than 5%, if the steam temperature and pressure are adjusted from the normal condition (814 K/3500 psi/25 MPa) to the ultra supercritical (USC) condition (1033 K/5500 psi/35 MPa), as illustrated in Figure 1 [1]. A higher efficiency is beneficial to greater saving in fuel and less environment pollution attributed to CO_2 emission. Even a 1% efficiency increase can reduce 1,000,000 tons of CO_2 emission to the atmosphere over the lifetime of an 800 MW plant [2]. However, higher plant efficiency under USC steam condition is mainly limited by a need of appropriate structural materials demonstrating high-temperature strength at acceptable cost, corrosion/oxidation resistance, and a good match of thermal expansion and conductivity.

The USC Turbines Program sponsored by the Department of Energy (DOE) expects an increase of the operating steam temperature to 950 K by the year 2010, and to 1033 K by 2020. USC steam turbine requires a tolerable creep rate of 3×10^{-11}/s at 35 MPa (or 5000 psi) and 1033 K, which is equivalent to a 2% elongation over 30 years [3]. Figure 2 provides an overview on the creep rupture strength as a function of temperature for three categories of materials, ferrite steels, austenitic steels, and Ni-based alloys, which are considered as candidates for USC steam turbine applications [4]. The maximal steam application temperature is defined by the intersection of the 100 MPa horizontal

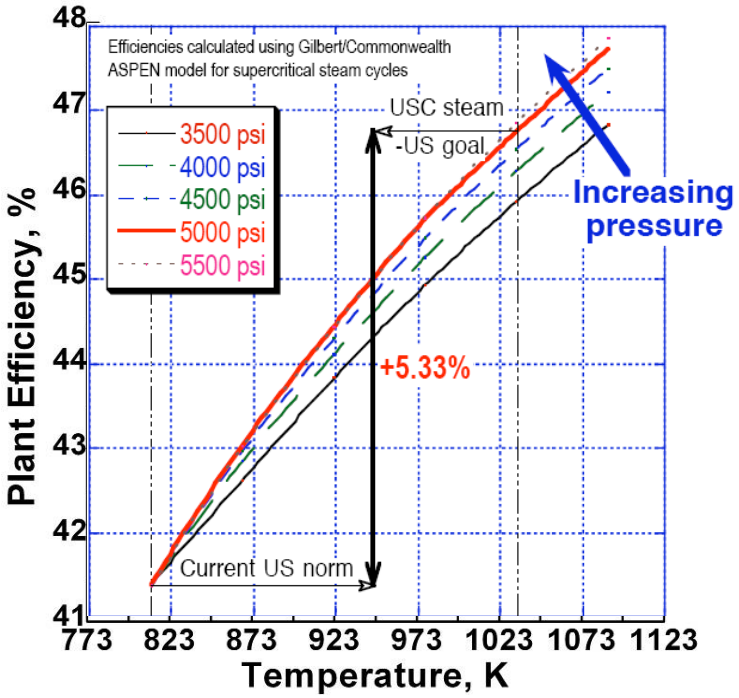

Figure 1. Effect of increasing steam temperature and pressure on cycle efficiency of fossil energy power plants [1].

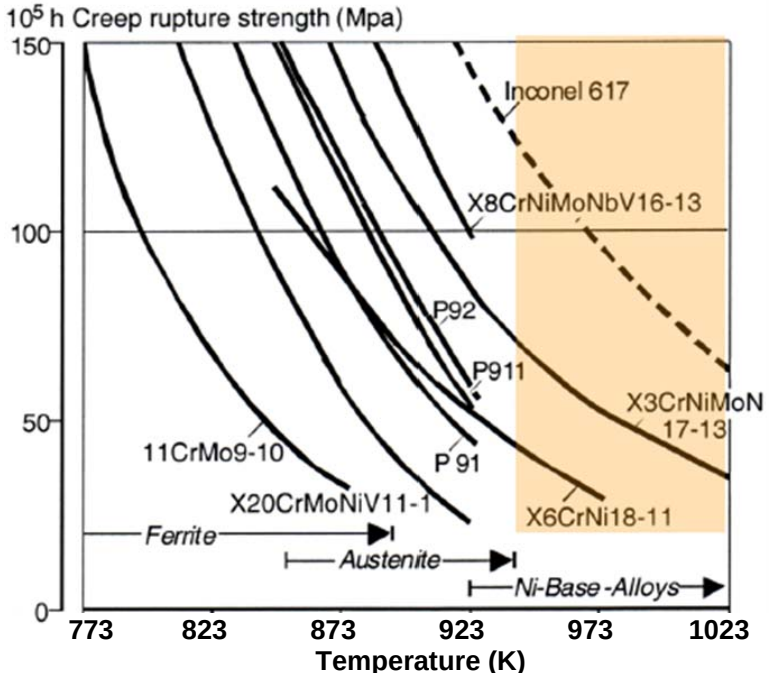

Figure 2. Creep rupture strength of ferritic steels, austenitic steels, and Ni-based alloys for main steam pipes in power plants [4]. Temperature range for USC steam turbines (948 ~ 1033 K) is highlighted.

line and creep rupture strength curves for various alloys. The successful development of T/P91 (Fe-9Cr-1MoVNb), T/P911 (Fe-9Cr-0.94Mo-0.9WVNb), and T/P92 (Fe-9Cr-0.5Mo-1.8WVNb) steels has pushed the steam-application temperature limit of ferritic steels into the range of austenitic steels ~ 893 K. However, their application at higher temperatures is limited by their poor creep and steam-corrosion resistance. The carbides in these steels are incoherent or only partially coherent with the matrix, which results in a relatively high interfacial energy that enhances the capillary-driven coarsening of the carbides. Although austenitic steels have higher steam application temperatures, their use at USC turbines is not appropriate because of their poor thermal conductivity and large thermal-expansion coefficient that constrain the startup and shutdown rates of steam turbines. The Ni-based alloys, e.g., Inconel 617, enable the steam temperature to be raised considerably to 973 K.

Compared to austenitic steels and Ni-based alloys, ferritic steels have unique advantages for steam-turbine applications, including low raw-material cost, low thermal-expansion coefficients, and high thermal conductivity. Consequently, there is increasing research interest in pushing the application temperature of ferritic steels to a higher limit. Our design strategy is to develop a Fe-Ni-Al-Cr based ferritic alloy, a cheaper alternative, which has a microstructure analogous to γ/γ′ Ni-based superalloys and superior creep and steam-corrosion resistance. Nickel-based superalloys owe their excellent creep strength due to the presence of a high volume fraction of coherent-coplanar ordered γ′ precipitates. Similarly, the body-centered-cubic (bcc) Fe-matrix (β) with NiAl *B2*-

type precipitates (β') exhibit a coherent-coplanar orientation relationship, providing the possibility of achieving an Fe-based analogue to the Ni-based superalloy. A typical Fe-Ni-Al ternary phase diagram with an isothermal section at 1023 K is shown in Figure 3 [5]. The miscibility gap of Fe and NiAl (β and β' phases) covers a range of compositions with 20 - 60% Fe, 30 - 50% Ni, and 10 - 30% Al (in atomic percent). With decreasing temperature, the miscibility gap becomes wider, which enables the remarkable precipitation of NiAl from the supersaturated Fe solid solution. Such precipitation tends to enhance the material's high-temperature strength and mechanical properties. The coherent precipitates have low interfacial energies and, therefore, could improve the coarsening resistance of precipitates. Further, due to the combined effects of Cr in the Fe matrix and β´ precipitates, both corrosion and oxidation resistances can be improved for applications in superheated-steam environments. A detailed review concerning the existing knowledge of the Fe-Ni-Al or Fe-Ni-Al-Cr alloy systems will be described in Chapter II.

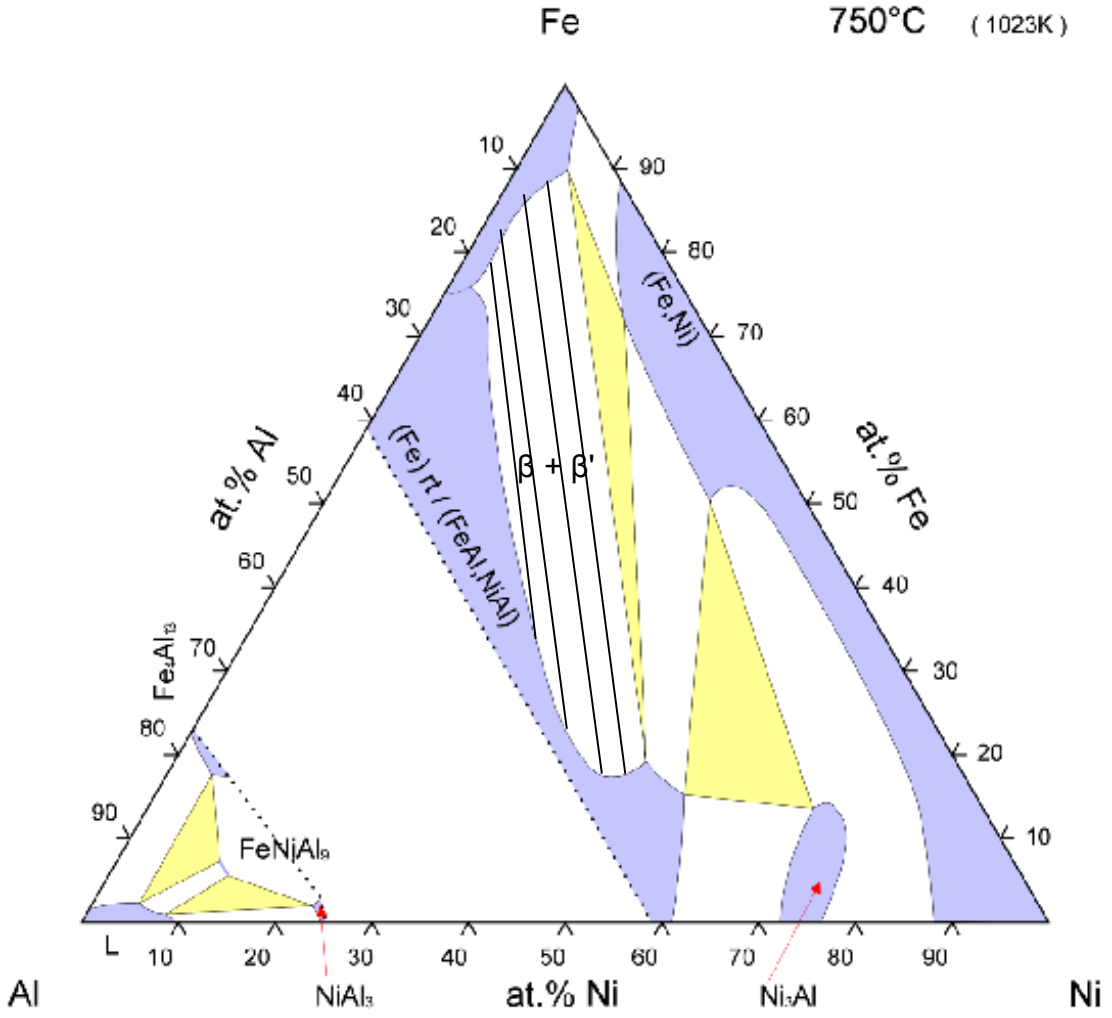

Figure 3. Ternary phase diagram of Fe-Al-Ni at 750 °C/1023 K. The miscibility gap of β and β' phases are marked by tie lines [5].

CHAPTER II
OVERVIEW OF THIS RESEARCH

2.1 Background: Literature Review

Much of the research on Fe-Ni-Al and related alloys has focused on the phase transformations, precipitation and coarsening kinetics, microstructure characterization, and room-temperature mechanical behavior [5-29]. The presence of NiAl-type *B2* precipitates has been observed and characterized in ferritic Fe-Ni-Cr-Al alloys.

Bradley [7-9] was the first to determine isothermal and vertical sections of the Fe-Ni-Al system showing a miscibility gap of Fe and NiAl-type phases in the temperature range from 1023 to 1673 K. The isothermal sections at temperatures between 1173 to 1200 K and compositions between 50 and 100 atomic percent (at.%) Al were studied recently [28-29]. Transmission-electron-microscopy (TEM) characterizations showed that spherically or cuboidally shaped precipitates with a *B2* (CsCl-type) crystal structure were uniformly distributed in the matrix [11-13,18]. Atom probe tomography (APT) was conducted to study the composition of NiAl *B2*-type precipitates in Fe-Ni-Al-Cr and Fe-Ni-Al-Mo alloys [6,10]. The NiAl precipitates were composed of mainly Ni and Al with a small amount of Fe. Mo was found to partition preferentially to the matrix. Depleted Cr was also observed in the precipitates of a PH13-8 stainless steel [14]. The lattice misfits between the matrix and the precipitate phases at room temperature were measured to be within a range of 0 ~ 0.7 % [19].

The precipitation kinetics of NiAl-type particles in Fe-Ni-Al and related alloys have been studied. The mean particle size follows the Lifshitz-Slyozov-Wagner (LSW) theory with a slightly broader size distribution [18,30]. The coarsening constant was measured to be on the order of 10^{-5} $\mu m^3/h$ at 1023 K in Fe-Ni-Al-(Cr) alloys. Calderon et al. [20-23] suggested that Mo can segregate to the precipitate-matrix interface and, thus, can reduce the lattice misfit and slow the coarsening process of NiAl-type precipitates. The coarsening constant measured in Mo-containing alloys is on the order of 10^{-7} $\mu m^3/h$ at 973 K. However, atom probe tomography (APT) characterizations found no evidence of the Mo enrichment at the interface [10]. An enhancement of the particle-coarsening kinetics was found during fatigue and creep deformation at 973 K, due to vacancies generated to stimulate diffusion and dislocation-particle interactions [19].

The evolution of the morphology of precipitates is found to be sensitive to several variables, such as composition, heat treatments, lattice misfit, and volume fraction. In Fe-Ni-Al-(Cr) alloys [21-23], the NiAl-type precipitates are initially spherical but become cuboidal during aging and finally turn to a sphere or plate with loss of coherency, similar to γ′ precipitates in Ni superalloys [20-23,31]. However, with the addition of Mo, the NiAl-type precipitates remain spherical at all particle sizes, irrespective of the mismatch in the lattice parameters between the precipitate and matrix over the range of compositions studied.

Rawers and Mattlin [32] investigated the oxidation resistance of Fe-Ni-Cr alloys over the temperature range of 1073 to 1273 K. When the Al content is

between 3 and 4.5 weight percent (wt.%), a substantial improvement in the oxidation resistance is observed due to the formation of a protective Al_2O_3 layer over an underlying Cr_2O_3 layer. Hence, the presence of a proper amount of Al may reduce the amount of Cr needed for achieving the desired oxidation resistance.

The influence of alloy composition on the room-temperature ductility has been investigated for Fe-Ni-Al-Cr-Mo alloys. Teng et al. [26] suggested that the volume fraction of NiAl precipitates and Al concentration in the matrix are the two major factors governing the ductility. Therefore, the cleavage resistance of the bcc-Fe matrix is influenced by the dissolved Ni and Al in solid solution, while the oxidation resistance of the Fe matrix is improved by the dissolved Al alone. It is implicit that conflicting issues arise as it is necessary to optimize the amount of Al (minimized for the ductility but maximized for the oxidation resistance) and Ni (to improve the cleavage resistance) in the Fe-based solid solution matrix.

However, in contrast to microstructural studies, limited work has been performed on the mechanical behavior of the alloys at elevated temperatures [30-31,33-35]. Stallybrass et al. [30] reported that the yield stress of Fe-Ni-Al-Cr alloys decreases dramatically above 873 K due to the dissolution of hyperfine precipitates formed during cooling. The yield stress of Fe-Ni-Al-Cr alloys is found to be higher than conventional heat-resistant steels but lower than Ni-based superalloys and intermetallic (Ni,Fe)Al phases [30,33].

Creep properties of several Fe-Ni-Al alloys have been examined by compressive and tensile creep tests in the stress range of 10 – 350 MPa and

temperature range of 873 – 1273 K for 9 ~ 40 volume fraction (vol. %) of β′ precipitates [31,33-35]. The steady-state creep rate is ~ 10^{-8} /s at a compressive stress level of 50 MPa and at 1023 K, in Fe-Ni-Al and Fe-Ni-Al-Cr alloys containing a 20 ~ 24 vol. % of precipitates [34-35]. This is not likely to achieve the target of 3 x 10^{-11} /s at 35 MPa and 1033K for USC turbines [3]. The dependence of the secondary creep rate on the applied stress can be described by a power law, if a threshold stress (a stress below which creep does not appear to occur, or is at least very slow) is introduced [31,33-35]. This threshold stress increases with the precipitate volume fraction and decreases rapidly with temperature [34]. The magnitude of the threshold stress is on the order of the Orowan stress as reported by Jung [33], and is approximately half of the Orowan stress reported in Zhu's study [35]. However, the dependence of the precipitate size, volume fraction, and stress on the threshold stress was not systematically investigated for this alloy. Controversy also exists on the observed creep mechanisms. Jung et al. [31,33] suggested that the creep mechanism in Fe-Ni-Al alloys is the diffusion-controlled dislocation-climb creep at high stresses and diffusional creep at low stresses. However, Zhu et al. [35] claimed that the creep mechanism is dislocation climb with a single slope of the stress dependence on the secondary creep rate in the same temperature and stress ranges for Fe-Ni-Al-Cr alloys with a comparable volume fraction and coarse grain size.

To summarize, creep resistance remains a major issue to be further investigated. The addition of Al and its partition in the matrix and precipitates need to be optimized to achieve the optimal microstructural attributes (e.g., NiAl

precipitate volume fraction, precipitate size, inter-particle spacing, element partition) as well as excellent properties (e.g., room-temperature ductility, high-temperature creep resistance, and oxidation/steam-corrosion resistance).

2.2 Objectives

The overall purpose of the sponsored DOE program is to design an Fe-based superalloy with excellent creep, coarsening, and steam-corrosion resistance in superheated steam environments. As a part of the program, the objective of my Ph.D. research is to (1) investigate the correlations among composition, microstructure, and mechanical behavior in several designed alloys with various amounts of Al, and (2) study the deformation micromechanism at high temperatures in the selected alloys which show the optimal creep resistance. Both computational and experimental tools are employed to pursue this research, including first-principles calculations (Chapter III), ultra-small-angle X-ray scattering, transmission electron microscopy, mechanical testing (Chapter IV), neutron diffraction, and crystal-plasticity finite-element simulations (Chapter V). A schematic outline of the proposed research is shown in Figure 4. The methodologies used and the conclusion drawn from the different studies will be elaborately described in the following chapters.

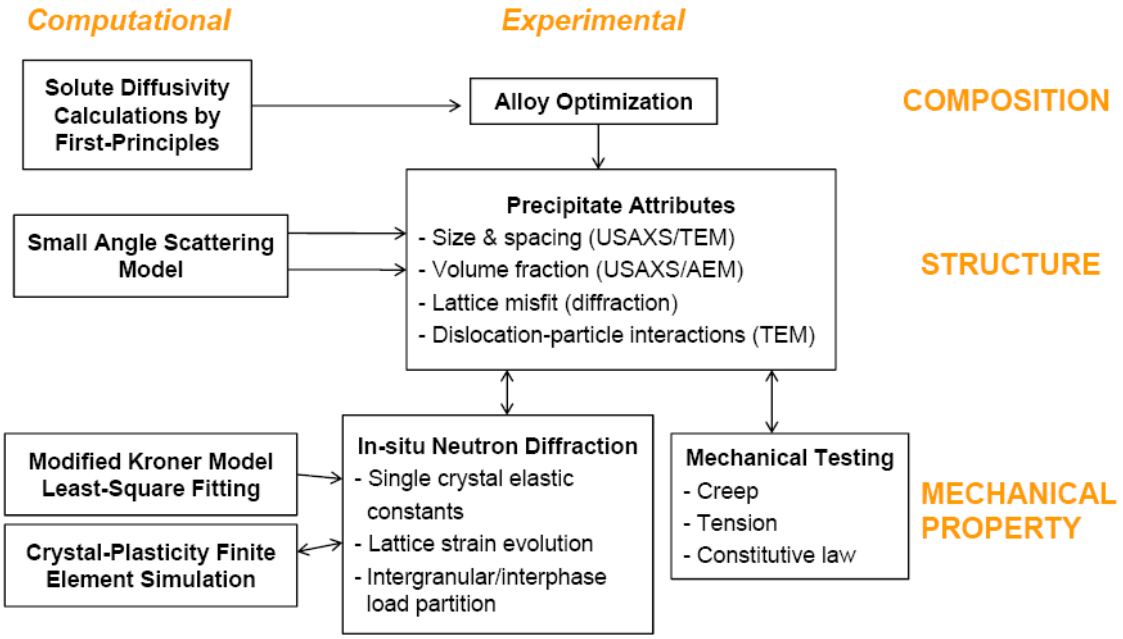

Figure 4. Schematic outline of the proposed research to study the interrelationship among the composition, microstructure, and mechanical properties using combined computational and experimental tools.

CHAPTER III
FIRST-PRINCIPLES CALCULATIONS OF IMPURITY DIFFUSIVITIES IN α-FE

3.1 Introduction

In recent years, first-principles computational methods, based on the electronic density-functional theory (DFT), have found widespread applications in the modeling of alloy thermodynamic properties and phase stability. First-principles methods have been applied extensively in calculations of alloy-formation energies, entropies, and phase boundaries, for a wide variety of binary and some ternary systems [36-41]. The results of such calculations are also increasingly incorporated within the CALculation of Alloy PHAse Diagrams (CALPHAD) formalism (e.g., [40,42-43]) for modeling complex multicomponent phase equilibria (e.g., [36,38,40,44-45]). The integration of thermodynamic, kinetic, and thermo-physical properties of solid solutions and intermetallic compounds calculated from first-principles and CALPHAD modeling has been outlined in a recent publication [44]. Such an approach allows simultaneous calculations of phase equilibria and relevant properties of the phase(s) in conjunction with suitable software(s) and database(s) facilitating accelerated alloy design and rapid prototyping. In the context of alloy design, an equally important area of applications for DFT methods is the calculation of alloy diffusivities. In comparison to the extensive amount of work devoted to thermodynamic properties, far fewer diffusion calculations for alloys have been

undertaken to date [46-58]. While the number of applications is currently limited, impressive agreement with experimental measurements has been demonstrated in recent calculations for a variety of solute species in Al and Ni based alloys [50-51,53,59]. For expanded applications of DFT techniques in modeling alloy-diffusion kinetics, further diffusivity calculations would be useful to assess the accuracy of these methods for other technologically-important systems, more generally.

In the present work, DFT methods are applied in calculations of impurity-diffusion constants for substitutional transition-metal (TM) solute species in a body-centered-cubic (bcc) ferritic Fe. This work is motivated by an effort aimed at the development of high-temperature, creep-resistant Fe-Ni-Al-Cr based ferritic alloys, containing fine dispersions of coherent, nanoscale (*B2*-NiAl based) precipitates in a bcc Fe matrix [26-27,34-35]. To optimize the properties of ferritic alloys for such high-temperature applications, it is desirable to identify slow-diffusing solute additions that can act to reduce the precipitate-coarsening kinetics, and help optimize creep strength.

Figure 5 presents a compilation of available experimental data for impurity diffusivities [60-97] in a bcc Fe. The results are presented at a representative temperature of 1050 K, and are plotted as relative values, i.e., as ratios of the solute-impurity diffusivities to the self-diffusivity of Fe at the same temperature. The results are plotted as a function of the electron to atom ratio for available transition metal ™ species, as well as a few non-TM elements. In cases where more than one data point is plotted for a given species, different measured

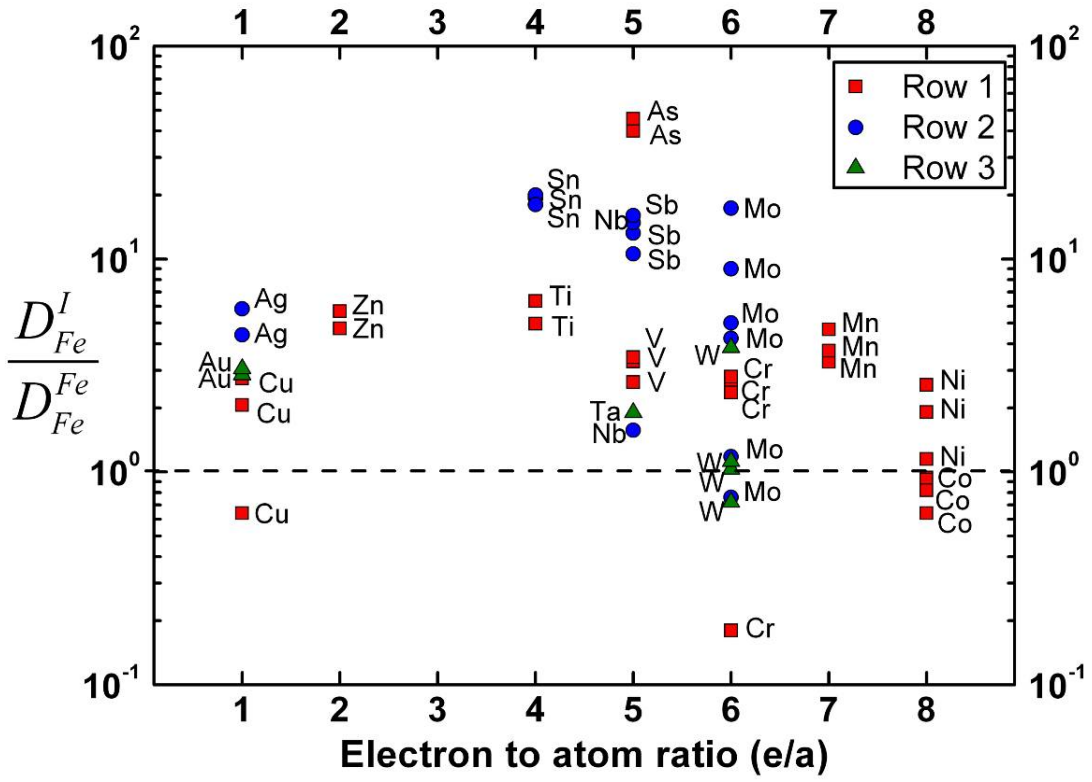

Figure 5. Ratio of diffusivities for impurity diffusion relative to self diffusion in α-Fe plotted for a variety of solutes as a function of the electron to atom ratio. The results correspond to a temperature of T = 1050 K and are obtained from published measurements [60-97]. Rows 1, 2, and 3 in the legend refer to the position of the element in the periodic table, corresponding to 3d, 4d, and 5d transition metal elements, respectively.

values are reported in the literature. In the context of the present work, three points related to Figure 5 are noteworthy. First, there is significant discrepancy between the values derived from independent measurements for several of the elements – an example is Mo where the reported values vary by more than an order of magnitude. Second, published results for most 5d TM elements are absent in the current database. Third, there are no clearly apparent slow-diffusing species, with diffusivities that are several orders of magnitude lower than that of pure Fe. The goal of the present work is to pursue the application of DFT methods as a framework for augmenting the database of impurity-diffusion constants in a bcc Fe, and to help guide the search for candidate slow-diffusing solutes in this material.

To this end, we present here a framework for calculating impurity-diffusion coefficients in a bcc Fe, and assess its accuracy through calculations of self-diffusion, and impurity-diffusion coefficients for W and Mo solutes. These two TM solute species are chosen due to the availability of recent measurements of impurity diffusivities over a wide temperature range [90,94]. The computational approach employed here is based on the nine-frequency formalism of Le Claire [98], which accounts for all of the distinct jump frequencies when the solute and vacancy display appreciable interactions at both first and second neighbor distances in the bcc lattice. Within this formalism, the computational approach combines first-principles calculations of saddle-point, vacancy-formation, and solute-vacancy binding energies and entropies in the ordered ferromagnetic state, with a semi-empirical model for the effects of magnetic disorder on the activation

energy [99-101] at temperatures up to and above the Curie temperature. Calculations of the relevant hopping frequencies are performed within the framework of the harmonic transition-state theory [102-103], following an approach similar to that employed in recent calculations of impurity diffusivities in a face-centered-cubic (fcc) Al [53]. The overall computational approach shares features in common with the methods employed in recent first-principles calculations of Cu, P, Ni, and Cr diffusion in a bcc Fe [46,48,57-58] – the current work extends these previous studies by including direct calculations of the vibrational frequencies required to compute diffusivity prefactors.

The remainder of this Chapter is organized as follows. In Section 3.2, we review the formalism employed to model effects of magnetic disorder on the temperature dependence of the measured diffusion data in a bcc Fe; relevant expressions from the harmonic transition-state theory, and the Le Claire formalism for impurity diffusivities on a bcc lattice are then reviewed, followed by the details of the first-principles calculations. Results are presented and compared with the experimental data and previous calculations in Section 3.3. A discussion and suggestions for further work are given in Section 3.4, followed by a summary in Section 3.5.

3.2 Computational Methodology

Measured self- and impurity-diffusion constants in a bcc Fe are often observed to display appreciably non-Arrhenius temperature dependencies in the ferromagnetic phase (e.g., [100] and references therein). This effect is generally

attributed to the dependence of the diffusion activation energy (*Q*) on the bulk magnetization (*M*), which is often modeled to have the following form [100]:

$$Q^F(T) = Q^P\left[1 + \alpha s(T)^2\right] \quad (1)$$

In Eq. (1), Q^P denotes the activation energy in the paramagnetic state (i.e., where *M = 0*), and *s = M(T) / M (T = 0 K)* is the reduced magnetization at the temperature, *T*, which varies continuously in the ferromagnetic phase between one at zero temperature, and zero at 1043 K, the Curie temperature [*s(T)=0* for all *T* in the paramagnetic phase]. α is a species-dependent parameter that quantifies the dependence of *Q* on magnetization. Equation (1) is derived based on a mean-field analysis of the effects of magnetic disorder on diffusion activation energies in ferromagnetic materials [99,101]; in this analysis the leading order correction to *Q* is quadratic in *s(T)*. In terms of the parameter, α, the activation energy in the fully-ordered ferromagnetic state, $Q_0^F = Q^F(T = 0\,K)$, is related to that in the paramagnetic phase through the relation, $Q_0^F = Q^P(1+\alpha)$.

In the present work, Eq. (1) is used to extend the zero-temperature DFT calculations, to account for the effects of magnetic disorder at a finite *T*. Specifically, all of the first-principles calculations are performed in the fully ordered ferromagnetic state, where both the diffusion prefactor (D_0) and activation energy (Q_0^F) are computed within the framework of the harmonic-transition-state theory. To account for the effects of magnetic disorder, Eq. (1) is used along with the published temperature-dependent values of *s(T)* [104-105], and the measured values of α for Fe self diffusion (α = 0.156), W-impurity

diffusion (α = 0.086) and Mo-impurity diffusion (α = 0.074) reported in Refs. [94,100]. As discussed in Refs. [58,100], for impurity species where the parameter, α, has not been measured, its value can be estimated from first-principles calculations employing a semi-empirical linear relationship between α and the induced changes in the local moments of the first and second-neighbor Fe atoms surrounding a solute impurity.

3.2.1 Self Diffusion

In all of the diffusivity calculations discussed in this chapter, we assume that diffusion is governed by a mono-vacancy mechanism mediated by nearest-neighbor vacancy hops. For self-diffusion governed by such a mono-vacancy mechanism on a bcc lattice, the diffusion coefficient can be expressed as (e.g., [106]):

$$D = a^2 f_0 C_v \Gamma \tag{2}$$

where a is the bcc lattice parameter, f_0 = 0.727 is the correlation factor for the bcc lattice, C_v denotes the equilibrium vacancy concentration, and Γ is the vacancy hopping frequency.

The equilibrium vacancy concentration can be expressed as:

$$C_v = \exp\left(\frac{\Delta S_v^f}{k_B}\right) \times \exp\left(-\frac{\Delta H_v^f}{k_B T}\right) \tag{3}$$

where ΔH_v^f and ΔS_v^f denote the vacancy formation enthalpy and entropy, respectively, and k_B is Boltzmann's constant. Considering only vibrational (phonon) contributions to the free energy, and employing the high-temperature

limit of the harmonic approximation for the lattice dynamics, ΔH_v^f and ΔS_v^f are constants, independent of temperature. In this limit, the vacancy-formation enthalpy at zero pressure can be calculated from first principles as $\Delta H_v^f = E(N-1) - [(N-1)/N]E(N)$, where *E(N-1)* denotes the energy of a supercell containing *N* lattice sites with *N-1* atoms and one vacancy, while *E(N)* represents the energy for the same supercell containing *N* atoms. Similarly, ΔS_v^f can be calculated as the difference in the high-temperature values of the vibrational entropy for a defected and non-defected supercell, yielding:

$$\Delta S_v^f = k_B \left[\sum_{i=1}^{3(N-1)} \ln\left(k_B T / h\nu_i^{vac}\right) - \frac{N-1}{N} \sum_{i=1}^{3N} \ln\left(k_B T / h\nu_i^{bulk}\right) \right] \quad (4)$$

where ν_i^{vac} denotes the vibrational frequencies in a supercell containing *N-1* atoms and a vacancy, while ν_i^{bulk} corresponds to the frequencies in a non-defected supercell containing *N* atoms. In this work, the vibrational frequencies entering Eq. (4) are computed from first principles employing a frozen-phonon methodology described below.

On the basis of the Vineyard's harmonic transition-state theory [102-103], the hopping frequency, Γ, can be written as:

$$\Gamma = \left[\prod_{i=1}^{3N-3} \nu_i^{vac} \Big/ \prod_{i=1}^{3N-4} \nu_i^{sad} \right] \times \exp\left(-\Delta H_v^{mig} / k_B T\right) \quad (5)$$

where ΔH_v^{mig} is the migration enthalpy, computed as the difference in the energy between an *N-1* atom supercell with the hopping atom in its saddle-point configuration, versus in its normal (stable) configuration. Similarly, ν_i^{vac} and ν_i^{sad}

are the phonon frequencies in the normal and saddle-point configurations, and the product in the denominator excludes the unstable mode for the transition state.

By combining Eqs. (1) - (5), the Fe self-diffusion coefficient is written as follows:

$$D = D_0 \exp\left\{- Q_0^F \left[\left(1 + \alpha s(T)^2\right)/(1+\alpha)\right] / k_B T\right\} \tag{6}$$

where the activation energy, Q_0^F, is given as the sum of the vacancy formation and migration energies in the fully-ordered ferromagnetic state:

$$Q_0^F = \Delta H_v^f + \Delta H_v^{mig} \tag{7}$$

The pre-factor, D_0, is expressed as:

$$D_0 = a^2 f_{bcc} \exp\left(\Delta S_v^f / k_B\right) \times \left[\prod_{i=1}^{3N-3} \nu_i^{vac} \Big/ \prod_{i=1}^{3N-4} \nu_i^{sad}\right] \tag{8}$$

where, as in Eq. (7), the vacancy formation entropy and vibrational frequencies are evaluated in the fully-ordered ferromagnetic state.

3.2.2 Impurity Diffusion

For impurity diffusion governed by a mono-vacancy mechanism on a bcc lattice, the diffusion coefficient can be expressed as (e.g., [98,106]):

$$D = a^2 f_2 C_v \exp\left(-\Delta G_b / k_B T\right) \Gamma_2 \tag{9}$$

In Eq. (9), the correlation factor, f_2, depends on the relative jump rates for a vacancy to different sites neighboring the solute atom [see Eqs. (11)-(12) below]. ΔG_b denotes the binding free energy between a solute atom and a nearest-neighbor vacancy, with the sign convention that negative (positive) values

correspond to attractive (repulsive) interactions. In this work, Γ_2, which denotes the frequency for a solute impurity to exchange with a nearest-neighbor vacancy, is calculated within the framework of the harmonic transition-state theory. This hopping frequency can, thus, be expressed analogously to Eq. (5) in terms of the migration energy for the vacancy-solute exchange, and the vibrational frequencies in the binding and saddle-point configurations.

The solute-vacancy binding free energy can be written as $\Delta G_b = \Delta H_b - T\Delta S_b$ in terms of a binding enthalpy (ΔH_b) and entropy (ΔS_b). Considering only phonon contributions to the binding entropy, and employing the high-temperature limit of the harmonic approximation for the lattice dynamics, ΔH_b and ΔS_b are again temperature-independent constants. The binding enthalpy is, thus, computed from first-principles calculations employing *N*-site supercells as ΔH_b = *E(N-2,1,1) - E(N-1,1,0) - E(N-1,0,1) + E(N,0,0)*, where *E(N-i,j,k)* denotes the total energy of a supercell containing *N-(j+k)* Fe atoms, *j*(= 0 or 1) solute atoms, and *k*(= 0 or 1) vacancies [with the vacancy and solute atom being nearest-neighbors for *E(N-2,1,1)*]. Similarly, the binding entropy can be written analogously to Eq. (4) as:

$$\Delta S_b = k_B \left[\sum_{i=1}^{3(N-1)} \ln\left(\nu_i^{vac} / \nu_i^{vac,sol}\right) + \sum_{i=1}^{3N} \ln\left(\nu_i^{sol} / \nu_i^{bulk}\right) \right] \quad (10)$$

where ν_i^{sol} denotes one of the *3N* phonon frequencies of a supercell containing *N-1* Fe atoms and one solute atom, and $\nu_i^{vac,sol}$ represents one of the *3N-3* frequencies of a supercell containing *N-2* Fe atoms and one nearest-neighbor solute-vacancy pair.

To compute values for the correlation factor (f_2) in Eq. (9) we employ the nine-frequency model of Le Claire [98]. The approach is based on the consideration of the relative rates of the eight different vacancy hops around the solute impurity illustrated Figure 6, plus the hop rate (Γ_0) for the bulk bcc lattice, far from the impurity. The nine frequencies labeled in Figure 6 correspond to all of the distinct hop rates, under the assumption that the vacancy-solute interaction is appreciable only for first and second neighbors, and negligible beyond. The results of first-principles calculations performed in this work indicate that the neglect of vacancy-solute interactions beyond the second neighbor is a reasonable assumption for both Mo and W solutes.

In the formalism of Le Claire [98] the correlation factor is written as follows:

$$f = \frac{1+t_1}{1-t_1} \tag{11}$$

where t_1 is expressed in terms of the jump frequencies labeled in Figure 6 as:

$$t_1 = -\frac{\Gamma_2}{\Gamma_2 + 3\Gamma_3 + 3\Gamma_3^{'} + \Gamma_3^{''} - \dfrac{\Gamma_3\Gamma_4}{\Gamma_4 + F\Gamma_5} - \dfrac{2\Gamma_3^{'}\Gamma_4^{'}}{\Gamma_4^{'} + 3F\Gamma_0} - \dfrac{\Gamma_3^{''}\Gamma_4^{''}}{\Gamma_4^{''} + 7F\Gamma_0}} \tag{12}$$

with F = 0.512. The jump frequencies in Eq. (12) can be expressed as:

$$\Gamma_i = \nu \exp\left(-\Delta H_i^{mig} / k_B T\right) \tag{13}$$

Where ν and ΔH_i^{mig} are the attempt frequency and associated migration energy for jump i, respectively. In the present work the migration energies, for each of the hops in Eq. (12), are derived from first-principles supercell calculations, as described below. The attempt frequencies are assumed constant for all of the

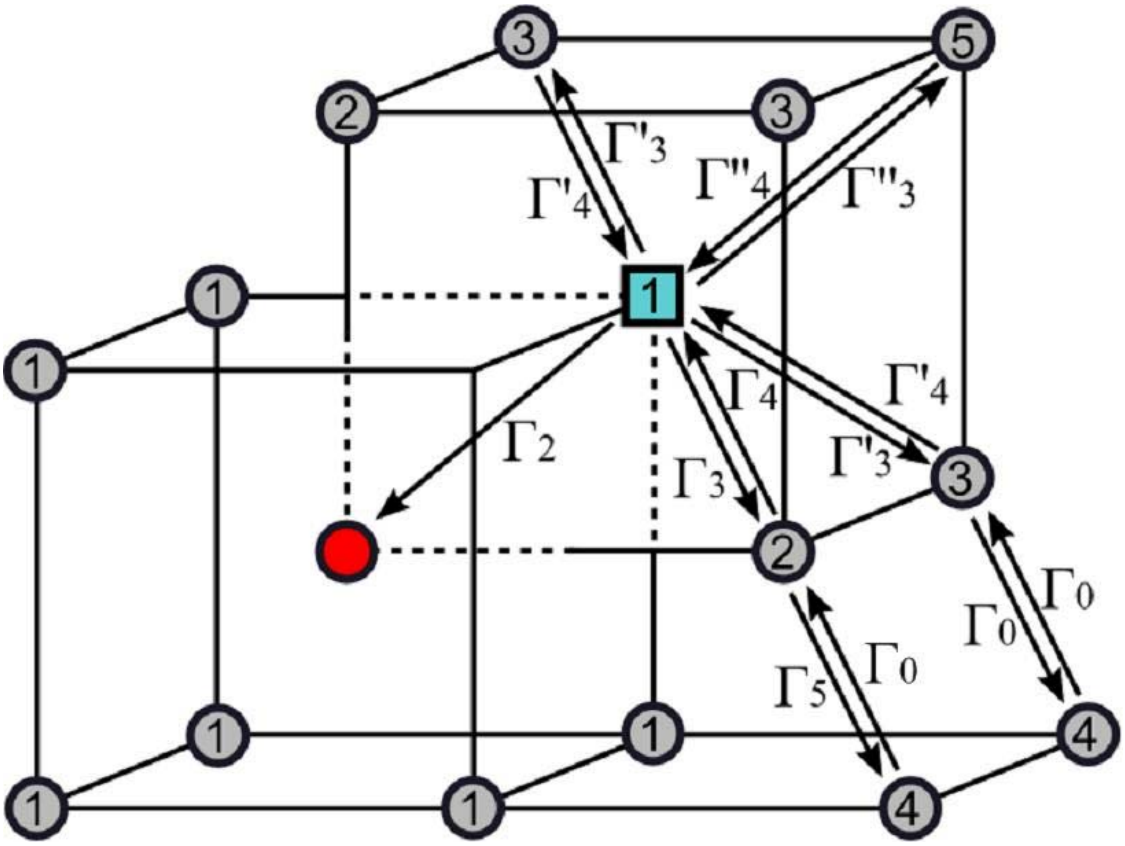

Figure 6. Illustration of the nine distinct jump frequencies considered in the calculation of the correlation factor for impurity diffusion [98,106]. The solute impurity is denoted by the red circle, the vacancy by the green square, and the solvent (Fe) atoms by grey circles. The numbers in the circles and squares correspond to the neighboring site of the solute atom. Figure adapted from Philibert [106].

jumps and thus drop out of the expression for t_1. Since the correlation factors for the W and Mo solutes considered here were found to be relatively insensitive to small variations in the Γ values, no attempt was made to refine the calculations of f_2 through direct calculations of the different attempt frequencies.

Over the temperature range of interest, the calculated values of f_2 for W and Mo solutes were found to display relatively weak dependencies on T. To a good approximation, the correlation factor for these solutes can thus be considered as a constant over the relevant temperature range, and the impurity-diffusion coefficient can then be written using Eqs. (3)-(5) and (9)-(10) in the same form as Eq. (6), with the activation energy for the fully-ordered ferromagnetic state given as:

$$Q_0^F = \Delta H_v^f + \Delta H_v^{mig} + \Delta H_b \tag{14}$$

and a prefactor given as follows:

$$D_0 = a^2 f_2 \exp\left[\left(\Delta S_v^f + \Delta S_b\right)/k_B\right] \times \left[\prod_{i=1}^{3N-3} \nu_i^{vac,sol} \Big/ \prod_{i=1}^{3N-4} \nu_i^{sad}\right] \tag{15}$$

In Eq. (14), the migration energy corresponds to the energy barrier for the exchange of the solute impurity with a nearest-neighbor vacancy.

3.2.3 Electronic Contributions

Equations (2)-(5), (10), and (13) account only for vibrational contributions to the vacancy formation, binding, and migration free energies. In earlier first-principles studies of vacancies in bcc transition metals [98,107] it was demonstrated that the additional contributions to these free energies associated

with electronic excitations can be significant in some cases. In the present study, electronic contributions to the vacancy formation, binding and migration free energies (for Γ and Γ_2) were computed using standard expressions formulated in terms of the calculated electronic densities of states (e.g., [108]). These electronic contributions were found to be relatively small, giving rise to increases in the calculated diffusion constants no larger than a factor of three over the temperature range investigated. These contributions are nevertheless included in the results presented in Section 3.3 below.

3.2.4 First-Principles Calculations

The vacancy formation, migration and binding energies, as well as the associated vibrational frequencies defined above, were computed within the framework of DFT as follows. All calculations made use of the projector augmented wave (PAW) method [109-110] and the Perdew-Burke-Ernzerhof (PBE) generalized-gradient approximation (GGA) [111], as implemented in the Vienna Ab initio Simulation Package (VASP) code [112-114]. We note that it is important to account for spin-polarization in these calculations for bcc Fe, as the bcc structure is not dynamically stable in non-magnetic DFT calculations [115]. A cutoff of 300 eV was used for the plane-wave expansion of the electronic wave functions. The PAW potentials used in this work are those labeled Fe, Mo, W, Hf and Ta in the VASP library; these potentials treat $4s^2 4p^0 3d^6$ electrons as valence for Fe, $5s^2 5p^0 4d^4$ as valence for Mo, and $6s^2 6p^0 5d^n$ (with n = 2,3,4) as valence for Hf, Ta and W. For each of the supercells considered in this work the

electronic states were sampled using a k-point density equivalent to a 12 x 12 x 12 mesh for a conventional bcc unit cell, and employing the Methfessel-Paxton [116] scheme with a broadening of 0.1 eV. All calculations were performed spin polarized, with a ferromagnetic ordering of the Fe moments. In all calculations the positions of the ions within the supercell were fully relaxed at constant volume and cell shape.

For the calculations of the vacancy formation, migration and solute-binding energies, use was made of periodic supercell geometries containing 128 lattice sites (4 x 4 x 4 conventional bcc unit cells). For the representative cases of vacancy formation and migration energies in pure Fe, and W solute-binding and migration energies, several tests were performed to estimate the convergence of the calculated results with respect to the supercell size, plane-wave cutoff and k-point density. On the basis of these tests, the vacancy formation, migration and binding energies are each estimated to be converged to within a precision of approximately 0.05 eV.

Vibrational frequencies were computed using the frozen-phonon approach [117] described in Ref. [118]. Use was made of supercells containing 54 lattice sites (3 x 3 x 3 conventional bcc unit cells), for which all of the **q**=0 phonon states were computed from the dynamical matrix, constructed as follows. For each cell, all symmetry-inequivalent rows of the **q**=0 dynamical matrix were determined, with the remaining rows given via symmetry-group transformations [119]. Elements $D^{ij}_{\alpha\beta}$ of the dynamical matrix are proportional to the force acting on the

atom *i* along the Cartesian direction α if the atom *j* is displaced by a small amount along the direction **β**, $F_\alpha^i = -\sqrt{M_i M_j} D_{\alpha\beta}^{ij} u_\beta^j$. For each symmetry-inequivalent choice of μ_β^i, the forces F_α^i were obtained for a set of five evenly distributed displacements around the equilibrium positions, from μ_β^i = -0.1 to 0.1 Å. The calculated forces were fit using a third-order polynomial, and the linear terms were used to extract $D_{\alpha\beta}^{ij}$. As in the energy calculations, the forces required for the dynamical matrix calculations were computed using a plane-wave cutoff of 300 eV and k-point sampling equivalent to a 12 x 12 x 12 mesh for a conventional bcc unit cell. Convergence tests were performed, examining the effects of the system size, k-point density and plane-wave cutoff on the vibrational entropy (computed from the **q**=0 phonon states) for pure Fe, yielding an estimated precision of 0.05 k_B/atom. The effect of system size was also explored for the vacancy formation entropy in pure Fe, through a comparison of results obtained from supercells containing 54 and 128 lattice sites. The effect of the supercell size on the vacancy-formation entropy was a change of approximately 20 percent.

For the calculation of migration energies and associated vibrational frequencies, an important issue concerns the location of the saddle-point position for the diffusing atom. As illustrated in Figure 6, nearest-neighbor vacancy hops involve the displacement of a neighboring atom along the <111> direction in the bcc lattice. In recent work involving the development of classical interatomic potentials models for Fe [120], the energy as a function of position for an Fe

atom exchanging with a vacancy on the bcc lattice was performed with three different potentials. One potential gave rise to an energy versus displacement plot containing a single maximum (saddle point) at the high-symmetry location a[1/4,1/4,1/4]. In contrast, the other two potentials produced two maxima along this path, separated by a local minimum at the same high-symmetry point – these potentials thus predicted saddle-point positions away from the a[1/4,1/4,1/4] position.

To determine the location of the saddle point predicted by DFT, for Fe self diffusion as well as for impurity diffusion of representative solute atoms, calculations were undertaken in the present work employing the nudged-elastic band (NEB) method [121-122]. Such calculations were performed for the nearest-neighbor exchange of Fe, W and Hf ions with vacancies in bcc Fe. In all cases the energy was found to display a single maximum, corresponding to a saddle point at the high-symmetry position located half way between neighboring sites. For Fe self-diffusion the results are in good agreement with those obtained by Fu *et al*. [123]. For nearest-neighbor vacancy exchanges with Mo and Ta ions, and for all of the other migration-energy calculations required in the calculation of the correlation factor [c.f., Eq. (12) above], the saddle point configurations were determined as follows. The diffusing atom was initially placed at the position half way between neighboring sites, and the structure of the supercell was subsequently relaxed using a quasi-Newton algorithm based on the calculated forces. In all cases where frozen-phonon calculations were performed using the resulting relaxed structures, the saddle-point nature of the solution was verified

by the fact that the vibrational spectra contained a single imaginary frequency with an associated eigenvector corresponding to a displacement of the diffusing ion along the transition path.

3.3 Results

Table 1 lists vacancy formation, migration and binding energies computed in the present study, as well as the associated activation energies for self- and impurity-diffusion in the paramagnetic and fully-ordered ferromagnetic state. Results are presented for pure bcc Fe as well as for W, Mo, Ta, and Hf impurities.

The binding energies reported in Table 1 refer to nearest-neighbor solute-vacancy pairs, and all are found to be negative (attractive) and appreciable in magnitude. These binding energies can be compared to those derived from first-principles calculations for Cr [57-58,124-125], Ni [58,124], Cu [47,124], P [48,124], and Sc, Ti, V, Cr, Mn, Co, Zn, Si, S, and Mo (in Ref. [124]) substitutional impurities in Fe. For all of these elements the vacancy-solute binding energy is calculated to be attractive, as found here for W, Mo, Ta and Hf. The magnitudes of the binding energies published for Cr (0.05-0.06 eV), Ni (0.07-0.19 eV), V (0.04eV), Cr (0.05eV), and Co (0.1eV) are somewhat smaller than those for the solute species considered here, while the values for Cu (0.16-0.24 eV), P (0.32-0.36 eV), Sc (0.63 eV), Ti (0.22 eV), Mn (0.16 eV), Zn (0.33 eV), Si (0.29eV), and S (0.53 eV) are comparable to those computed for W, Mo, and Ta, respectively. The calculated value of the binding energy for Mo (0.33 eV)

Table 1. Calculated energetics for self and impurity diffusion in bcc Fe. Vacancy formation energies (ΔH_v^f), migration energies (ΔH_v^{mig}), and solute-binding energies (ΔH_b) are calculated in the fully ordered ferromagnetic state and used to compute the corresponding value of the diffusion activation energy (Q_0^F). The variable α parameterizes the dependence of the activation energy on magnetization – the values for Fe, W and Mo are taken from experimental measurements, while the values for Ta and Hf have been estimated from first-principles calculations of induced magnetization as discussed in the text. The activation energy in the paramagnetic state (Q^P) is derived as $Q^P = Q_0^F /(1+\alpha)$.

	Fe	W	Mo	Ta	Hf
ΔH_v^f (eV)	2.23	-	-	-	-
ΔH_b (eV)	-	-0.14	-0.17	-0.32	-0.65
ΔH_v^{mig} (eV)	0.64	0.71	0.54	0.44	0.18
α	0.156	0.086	0.074	0.057	0.047
Q_0^F (eV)	2.87	2.80	2.60	2.35	1.75
Q^P (eV)	2.48	2.58	2.42	2.22	1.67

reported in Ref. [124] is somewhat higher than the magnitude of 0.17 eV obtained in the present work. Relative to the other substitutional impurities considered in this and previous studies, the Hf impurity is found to display anomalously large binding to a neighboring vacancy.

For pure Fe the vacancy formation and migration energies obtained here are consistent with the range of values of ΔH_v^f =1.93-2.18 eV and ΔH_v^{mig} =0.64-0.71 eV published previously from GGA-based DFT calculations [47,57-58,125-127]. The migration energies for the solutes in Table 1 correspond to a nearest-neighbor exchange with a vacancy. Of the solutes considered here, only W shows a larger value of ΔH_v^{mig} than that for Fe self diffusion, while Hf shows the lowest value. When the vacancy formation, binding and migration energies are combined to compute the ferromagnetic activation energies (Q_0^F) from Eqs. (7) and (14), it is seen that all solutes have a smaller calculated value than that for Fe self diffusion in the ordered ferromagnetic state.

For the high-temperature paramagnetic phase, the estimated values of the activation energy (Q^P) are derived from the first-principles-calculated value of Q_0^F through the relation $Q^P = Q_0^F/(1+\alpha)$, expressed in terms of the parameter α defined above. For Fe, Mo and W the value of this parameter has been obtained with the published measurements [94,100] given above, while for Ta and Hf the values quoted in Table 1 are estimated based on an empirical linear correlation between α and $\Delta M_{1\text{-}2}$, the induced change in the local magnetic moments for the first and second neighbor Fe atoms surrounding the solute impurity [58,100].

Specifically, the values of $\Delta M_{1\text{-}2}$ were computed for Nb, W, Mo, Cr, Fe, and Co from first-principles calculations employing the methods described in Section 3.4; a linear relation was then fit between the measured values of α for these solutes, and the first-principles calculated values of $\Delta M_{1\text{-}2}$. The resulting fit reproduced the measured values of α to better than 20 percent. Using the resulting fit, the values of α given in Table 2 for Ta and Hf were estimated from calculated values of $\Delta M_{1\text{-}2}$. Comparing the predicted values of Q^P, it is seen that only W is predicted to have a slightly larger value of the activation energy in the paramagnetic phase than that for Fe self diffusion, while Hf is again seen to display the lowest value.

We focus for the remainder of this section on W and Mo impurity diffusion. For both species the vibrational frequencies, and all of the migration energies required to compute the correlation factor (f_2) have been calculated. We are thus able to compute the diffusion prefactors as well as activation energies for these solutes, allowing a direct comparison of the first-principles results for temperature-dependent diffusion constants with experimental measurements.

Table 2 lists the calculated values of f_2 for W and Mo at representative temperatures of 800, 1000, and 1200 K. While for W the values are very similar to the correlation factor for pure Fe ($f_0 = 0.727$), for Mo the values are roughly a factor of 2 to 3 smaller. As mentioned above, the temperature dependencies of the calculated values of f_2 are relatively weak in comparison to the Arrhenius terms in the associated diffusion constants. For Mo the calculated results for f_2 in

Table 2. Correlation factors (f_2) for Mo and W solute-diffusion at representative temperatures of 800, 1000, and 1200 K. The results are calculated within the Le Claire formalism using first-principles-calculated migration energies, as discussed in the text. The calculated value of f_2, as well as the ratio of f_2 to the constant value of the correlation factor for bcc self-diffusion ($f_0 = 0.727$), is listed for each solute.

	W		Mo	
T (K)	f_2	f_2 / f_0	f_2	f_2 / f_0
800	0.77	1.06	0.22	0.30
1000	0.74	1.02	0.28	0.39
1200	0.73	1.00	0.33	0.46

Table 2 are noted to be significantly smaller than the range of values of 0.87 - 0.90, for temperatures between 823 and 1173 K, obtained in a recent analysis by Nitta *et al.* [128]. In their analysis, Nitta *et al.* made use of measurements of the concentration dependencies of the intrinsic diffusivities of Fe and Mo in bcc Fe-Mo solid solutions. The data was analyzed in the framework of the nine-frequency model described in Section 3.2, but with some simplifying assumptions including: $\Gamma_3' = \Gamma_3''$, $\Gamma_4' = \Gamma_4'' = \Gamma_0$, and $\Gamma_3 / \Gamma_3' = \Gamma_4 / \Gamma_5$. The discrepancy between the estimated values for f_2 obtained by Nitta *et al*. and those derived in the present study is attributed to the fact that the relations between the hopping frequencies assumed in Ref. [128] are not found to hold in the first-principles calculations. For example, Γ_4 is calculated to be more than twice larger than $\Gamma_4^{"}$ at 1200 K.

Tables 3 - 5 list the calculated diffusion prefactors (D_0) and activation energies (Q^P and Q_0^F) for Fe self diffusion and W- and Mo-impurity diffusion. Each is compared to available published values, based on analyses of experimental data. For Fe self diffusion, the calculated value of Q_0^F is roughly in the middle of the range of published values, while the present calculated value for Q^P is on the lower end of the range reported from experimental measurements. The magnitude of the prefactor of Fe self diffusion calculated here is on the order of 10^{-4} m^2/s and is comparable to a number of published values in this same range, while being inconsistent with the higher values of around 10^{-2} m^2/s derived in some analyses.

Table 3. Activation energies in the fully ordered ferromagnetic state (Q_0^F) and paramagnetic state (Q^P) are listed, along with diffusion prefactors for self diffusion in bcc Fe. Results obtained from the present calculations are compared with available published experimental measurements. The calculated prefactors in this work are weakly temperature dependent and the result listed in this Table and Tables 4 and 5 correspond to T = 1050 K.

	Q_0^F (kJ/mol)	Q^P (kJ/mol)	D_0 (m^2/s)
Present work	277	239	6.7×10^{-5}
Iijima et al. [85]	289.7 ± 5.1	250.6 ± 3.8	2.8×10^{-4}
Borg et al. [80]	-	281.5	1.2×10^{-2}
Geise et al. [83]	-	281.6	1.2×10^{-2}
Graham et al. [61]	-	239.7	2.0×10^{-4}
Walter et al. [96]	-	240.6	2.0×10^{-4}
Buffington et al. [82]	-	239.3	1.9×10^{-4}
Hettich et al. [84]	283.7	-	1.0×10^{-4}
James et al. [67]	254.0	240.6	2.0×10^{-4}
Lübbehusen et al. [89]	284.7 - 299.1	248.0 - 258.6	$6.8 - 12.3 \times 10^{-4}$
Kucera et al. [88]	-	261.5	1.1×10^{-3}

Table 4. Activation energies in the fully ordered ferromagnetic state (Q_0^F) and paramagnetic state (Q^P) are listed, along with diffusion prefactors for impurity diffusion of W in bcc Fe. Results obtained from the present calculations are compared with available published experimental measurements.

	Q_0^F (kJ/mol)	Q^P (kJ/mol)	D_0 (m^2/s)
Present work	270	249	1.4×10^{-4}
Takemoto et al. [94]	312.0 ± 27.0	287.0 ± 22.0	1.5×10^{-2}
Kucera et al. [87]	-	246.2 ± 3.2	2.0×10^{-4}
Gruzin et al. [62]		292.9	3.8×10^{-1}
Alberry et al. [78]	-	243.5 ± 7.1	1.6×10^{-4}
Keiszniewski et al. [86]	-	265.7	6.9×10^{-3}
Davenport et al. [97]	298	-	2.5×10^{-3}

Table 5. Activation energies in the fully ordered ferromagnetic state (Q_0^F) and paramagnetic state (Q^P) are listed, along with diffusion prefactors for impurity diffusion of Mo in bcc Fe. Results obtained from the present calculations are compared with available published experimental measurements.

	Q_0^F (kJ/mol)	Q^P (kJ/mol)	D_0 (m^2/s)
Present work	251	234	6.3×10^{-5}
Nitta et al. [90]	-	282.6 ± 6.4	1.5×10^{-2}
Kucera et al. [87]	-	216.3	5.7×10^{-5}
Alberry et al. [78]	-	225.5 ± 4.6	7.9×10^{-5}
Borisov et al. [81]	-	205.0	3.0×10^{-5}
Nohara et al. [91]	284.5 ± 6.7	272.8 ± 5.4	3.1×10^{-3}
Davenport et al. [97]	238	-	4.4×10^{-5}

For W-impurity diffusion both Q_0^F and Q^P are on the lower end of the range of measured values. For Mo-impurity diffusion the calculated activation energies in the ferromagnetic and paramagnetic states display values in the middle of the range of experimentally derived estimates. The magnitudes of the prefactors for W and Mo impurity diffusion obtained from the first-principles calculations are similar to those derived for Fe self diffusion, on the order of 10^{-4} to 10^{-5} m^2/s, which is consistent with some of the published values with the same order of magnitude, while being much smaller than the values in the range of 10^{-2} to 10^{-1} m^2/s reported in others.

Figures 7-9 present a direct comparison between calculated and measured temperature dependent diffusion coefficients for Fe self diffusion (Figure 7), and W and Mo impurity diffusion (Figures. 8 and 9, respectively). The diffusivities are calculated up to 1184 K, the α→γ transition temperature. For Fe self diffusion the agreement between calculations and measurements in the ferromagnetic phase is excellent, while the calculated values underestimate slightly (by a factor of 2-4) the measured values in the paramagnetic phase at the highest temperatures due to an apparent slight underestimation of the slope on the Arrhenius plot (i.e., the activation energy).

We focus next on a comparison of the calculated and experimentally measured impurity diffusion coefficients for Mo and W. The most recent measurements have been undertaken by the Iijima group [90,94], and should be used as the basis for quantitative comparisons with the calculations. Considering first W impurity diffusion, the measurements in Ref. [94] made use of high-purity

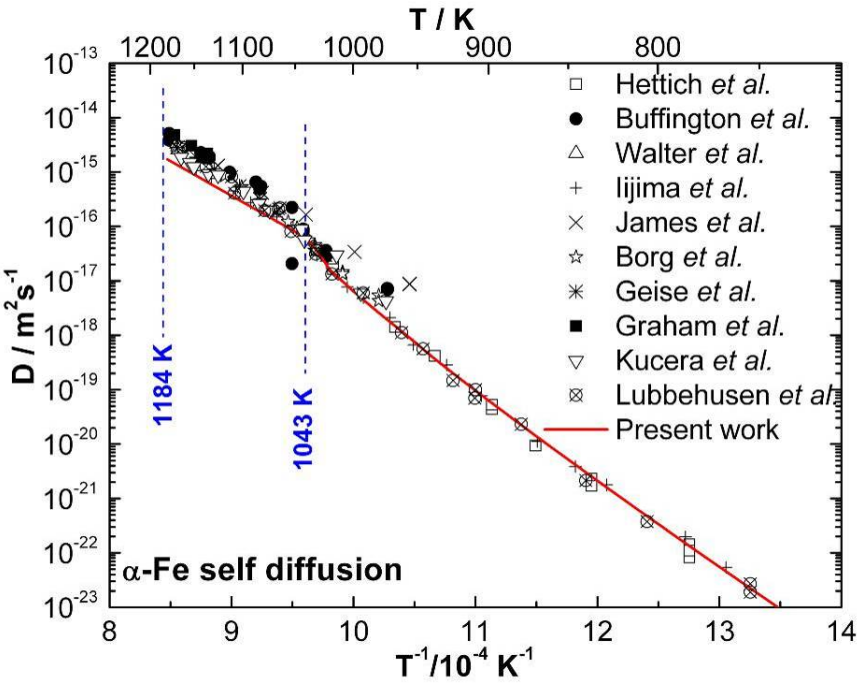

Figure 7. Predicted temperature dependence of the calculated α-Fe self-diffusion coefficient (red line) versus published experimental data [61,69,80,82-85,88-89,96].

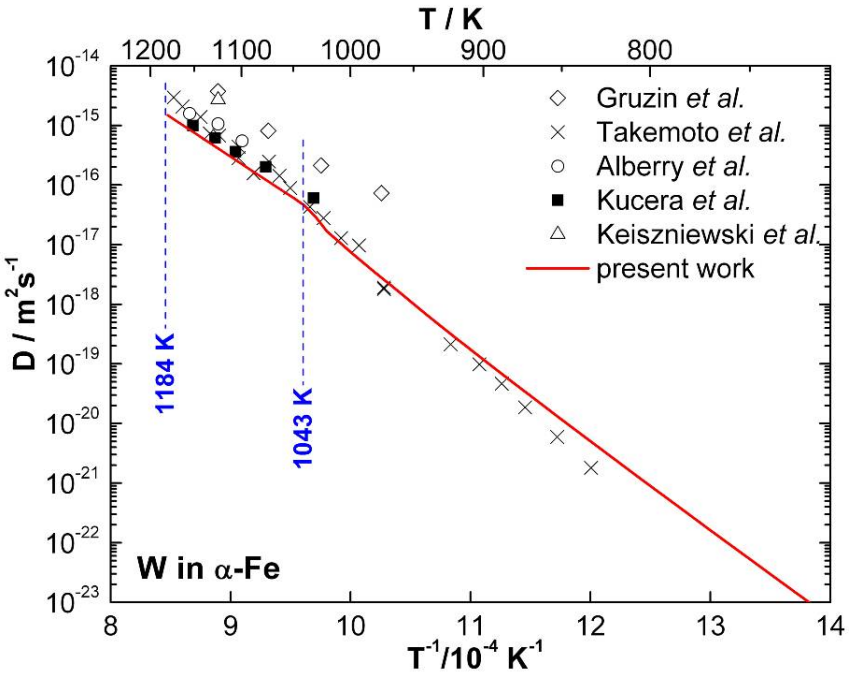

Figure 8. Predicted temperature dependence of the calculated impurity-diffusion coefficient for W in α-Fe (red line) versus published experimental data [62,78,86-87,94].

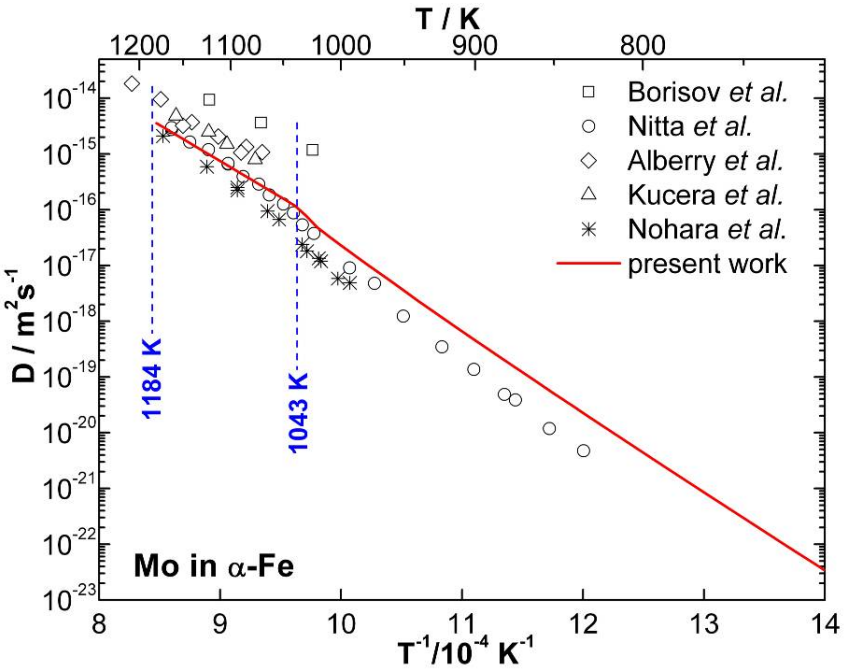

Figure 9. Predicted temperature dependence of the calculated impurity-diffusion coefficient for Mo in α-Fe (red line) versus published experimental data [78,81,87,90-91].

Fe and impurity diffusivities were measured by tracer analysis over the temperature range of 833 to 1173 K, employing magnetron sputter-microsectioning, radio-frequency sputter-microsectioning, and ion-beam sputter-microsectioning techniques. At 1053 K, the reported experimental value of the W impurity diffusivity is 8.94 x 10^{-17} m^2/s, which is in very good agreement with our calculated value of 6.23 x 10^{-17} m^2/s at the same temperature. The measured results in the paramagnetic phase due to Takemoto *et al.* [94], Kucera *et al.* [87], and Alberry and Haworth [78] agree fairly well, but those due to Gruzin [62] and Kieszniewski [86] are higher by a factor of up to 5; possible reasons for these discrepancies could include differences in the impurity and grain sizes of the starting materials, instrumental accuracy in the older measurements and/or surface stress effects. The calculated diffusion coefficients show good overall agreement with the measured values in the ferromagnetic phase obtained by Takemoto *et al.* [94], although the calculated values are seen to be larger than these measurements at the lowest temperatures. The calculations are similarly in good agreement with the measurements of Refs. [78,87,94] in the paramagnetic phase, leading to at most a factor of 2-5 underestimation of the measured data at the highest temperatures.

For Mo-impurity diffusion the measurements of Nitta *et al.* [90] made use of the same starting materials and similar experimental techniques as those listed above for the W measurements of Ref. [94]. At 1050 K, the measured values of the Mo impurity diffusivity is 1.26 x 10^{-16} m^2/s [90] which is in very good agreement with our calculated value of 1.44 x 10^{-16} m^2/s. Borisov *et al.* [81],

Kucera *et al.* [87], and Alberry and Haworth [78] reported measurements of the Mo impurity diffusivity in the paramagnetic phase over a small temperature range, and their values are higher (by as much as an order of magnitude) than those reported by Nitta *et al.* [90]. Possible reasons for this large discrepancy include the factors listed above. Nohara and Hirano [91] also determined the tracer diffusivity or Mo impurities in both the ferro- and paramagnetic phases, but their values are lower by a factor of 2-3 than those due to Nitta *et al.* [90]. There is a slight discrepancy between the presently computed and measured data of Nitta *et al.* [90] in the ferromagnetic phase and, as with W, this discrepancy increases at lower temperatures. Nevertheless, for Mo our predictions overestimate by no more than a factor of 2-5 the measured values in the ferromagnetic state, while the predicted values show even better agreement with the published experimental data in the paramagnetic phase.

It is noteworthy that while the diffusion coefficients are well predicted by the calculations for Fe at both low and high temperatures, the calculated solute impurity diffusivities show relatively better agreement with measurements at high T, and larger discrepancies at low T. Given that the DFT results should be most accurate for the low-temperature ordered ferromagnetic phase, for which all of the calculations were performed directly, further studies would be of interest to understand whether the larger discrepancy with experimental measurements at the lowest temperatures is due to systematic errors in the calculations, or inherent difficulties associated with the measurements at low T. Overall, considering that the calculations do not involve any adjustable parameters, the

agreement between the computed and measured results over the relevant temperature range is viewed to be highly encouraging, and suggests that the computational methodology presented in this paper provides sufficient accuracy to be useful in the context of designing coarsening-resistant microstructures.

3.4 Discussions

As mentioned in Section 3.1, the motivation for this work is the development of a computational framework to assist in identifying slow-diffusing elements in a bcc Fe matrix, for the design of coarsening-resistant nanoscale precipitate microstructures in Fe-Ni-Al-Cr based alloys. This goal is motivated through the analogy with two-phase Ni-based superalloys. In Ni, many 4d and 5d transition-metal solutes display impurity diffusion coefficients, which are orders of magnitude smaller than the self-diffusivity in pure Ni [49,52]. The addition of these TM elements correlates with substantial improvements in the coarsening resistance and high-temperature creep properties of modern commercial Ni-based superalloys. Thus, it is desirable from the standpoint of the design of analogous two-phase ferritic alloys to see whether such slow-diffusing solutes can be identified. We consider this question in light of the compiled data in Table 1 and the results of the current calculations.

Figure 10 shows that for the two 4d and 5d TM solutes considered in the present work, namely Mo and W, the calculated impurity-diffusion coefficients are equal to or larger than the diffusivity for Fe self-diffusion. The main effects underlying this result are shown in Tables 3-5 to be the slightly lower values of

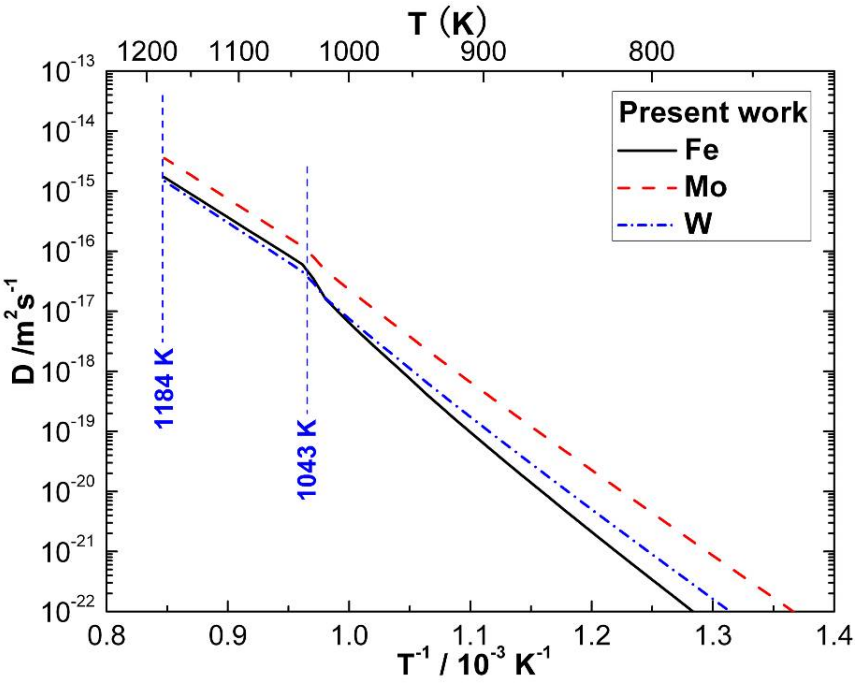

Figure 10. Predicted temperature dependence of the diffusion coefficient for W and Mo-impurity diffusion, compared with that for self-diffusion in α-Fe.

the activation energies of W- and Mo-impurity diffusion compared to Fe self diffusion – the diffusion prefactors are computed to have comparable magnitudes. The lower values of the activation energies for Mo and W impurity diffusion can be seen in Table 1 to be due to both the appreciable and negative values for the vacancy-solute binding energies, and a slightly reduced value of the migration energy in the case of Mo. If we assume that the diffusion prefactor is roughly constant, as the calculated results in Tables 3-5 seem to suggest, the first-principles data in Table 1 indicate that the comparable or higher values of the impurity-diffusion coefficients relative to self diffusion in bcc Fe may be more general for other 5d TM alloying elements, for which measured data in pure bcc Fe is lacking. Specifically, both Ta and Hf impurities are computed to have substantially lower values of the activation energies than that for Fe self diffusion in Table 1. The trend towards higher values of impurity-diffusion constants relative to self diffusion is also consistent with the measured data for 4d elements compiled in Figure 5.

The calculated and measured results compiled in this work stand in sharp contrast to Ni-based alloys, where activation energies vary by more than a factor of two for 4d and 5d solutes, with the associated diffusion constants at relevant temperatures varying by more than four orders of magnitude at 1173 K [51]. The current results and the measured data plotted in Figure 5 suggest an absence of comparable slow diffusers amongst the common solute additions to bcc Fe. An outstanding question that deserves further attention is whether the apparently smaller variations in impurity diffusion coefficients for TM solutes in bcc Fe,

relative to fcc Ni, is due to the differences in bonding (electronic structure) in these systems, or the geometrical differences of the more open bcc lattice relative to the close-packed fcc structure. To address this question it would be interesting to extend the computational framework described here more generally to other bcc elements, to further investigate the general trend of the variations of TM impurity diffusion coefficients in other bcc hosts.

An important observation that can be made from the results presented in this paper is the absence of the often-assumed correlation between the magnitude of the impurity diffusivity and the atomic size of the solute. While such a correlation is often assumed as a useful "rule of thumb," it clearly breaks down in the case of impurity diffusion in bcc Fe. This point is apparent when considering the measured impurity diffusion coefficients for the four oversized TM solutes Ti, Mo, W and Ta, in comparison to that for the undersized Co solute. The atomic volumes ($Å^3$) in the stable room-temperature structure [129] for these solutes and pure Fe are: Fe (11.78), Co (11.07), Ti (17.64), Mo (15.58), W (15.85), and Ta (18.01). In Figure 5 the lowest and highest impurity diffusivities occur for the smallest (Co) and largest (Ti) of these solutes, respectively. Further, while Mo, W and Ta have atomic volumes roughly 30-50 % larger than Co, their impurity diffusivities are comparable to or even slightly larger in magnitude. The lack of a correlation between atomic size and the magnitudes of impurity diffusion coefficients in Ni [51] and Al [55] has also been discussed previously. Collectively, these previous studies and the present work demonstrate that the search for slow-diffusing elements should be based on more detailed

considerations of the chemical (electronic-structure) factors underlying the magnitudes of the migration and solute-vacancy binding energies and entropies, rather than a simple size effect.

It should be emphasized that the present calculations and the compiled experimental data in Figure 5 are associated with impurity-diffusion coefficients for highly dilute solute concentrations in pure bcc Fe. From the standpoint of developing coarsening-resistant bcc-based microstructures, at the higher solute compositions employed in real alloys, it may be important to consider the concentration dependencies of the relevant diffusivities. For example, Nitta *et al.* [128] recently reported results of measurements for the concentration dependence of both Fe and Mo tracer diffusion coefficients in binary bcc Fe-Mo alloys. In this system the diffusion coefficient of Fe is measured to increase with increasing Mo content, whereas that for Mo decreases. For concentrations greater than 1.5 atomic percent (at. %) Mo concentration, the solute tracer-diffusion coefficient becomes slower than that for Fe at high temperatures. It is also interesting to consider the published results indicating that in dilute Fe(V) alloys, Hf impurities display a diffusion coefficient which is as much as 3 orders of magnitude lower than that for Fe [130]. The current calculated results for activation energies presented in Table 1 suggest that in pure bcc Fe, Hf impurities should display very high relative diffusion constants (assuming that the diffusion prefactor is not anomalously low). To reconcile the measurements and calculations in the case of Hf, it would be interesting to investigate the effects of V solutes on Hf impurity diffusion in bcc Fe. Overall, it would be of interest to

extend the formalism presented in this paper to the study of the concentration dependencies of relevant diffusion coefficients for non-dilute Fe alloy compositions. While such studies lie beyond the scope of the current work, they should be possible by generalizing the first-principles formalism presented in Ref. [56] to magnetic bcc Fe-based systems.

3.5 Summary

A framework involving the combination of first-principles DFT calculations and a semi-empirical correction for magnetic effects has been outlined to predict temperature-dependent self- and substitutional-impurity-diffusion coefficients in the ferromagnetic and paramagnetic phases of bcc Fe. The activation energies are determined from DFT calculated vacancy formation, migration, and nearest-neighbor solute-vacancy binding energies in the ordered ferromagnetic state. The diffusion prefactors are derived from DFT calculations of longer-ranged solute-vacancy binding and migration energies, and the relevant vibrational and electronic entropies, employing Vineyard's harmonic transition-state theory and the Le Claire nine-frequency formalism.

The computational approach has been applied to calculations of Fe self-diffusion, and impurity-diffusion coefficients for W and Mo solutes in bcc Fe. The computational results are compared with available experimental measurements in the temperature range of 800 to 1184 K. Calculated and measured self and impurity diffusion coefficients are found to agree within a factor of five over this temperature range, with the level of agreement between experiment and theory

being comparable to the scatter of experimental data in the high-temperature paramagnetic phase. The calculated impurity diffusion coefficient for Mo is larger than the self-diffusivity of bcc Fe over the entire temperature range below the α-γ phase transition. Calculated activation energies for Ta and Hf impurities suggest that these solutes should also display impurity diffusion coefficients larger than that for Fe self-diffusion. For W the calculated impurity-diffusion coefficient is comparable to and larger than the Fe self-diffusivity in the paramagnetic and ferromagnetic phases, respectively.

The current computational study is motivated in the context of the design of nanoscale-precipitate-strengthened ferritic alloys, where the identification of slow diffusing solutes in the bcc matrix is desirable for the optimization of coarsening and creep resistance. The accuracy of the results obtained in this study suggests that the proposed computational approach should provide a useful tool to aid in the development of kinetic databases for such alloy-design efforts.

CHAPTER IV
EFFECT OF AL ON MICROSTRUCTURE AND CREEP BEHAVIOR

4.1 Introduction

The creep behavior of the particle-strengthened alloys is largely dependent on the microstructural parameters of the precipitates viz. particle size, inter-particle spacing, and volume fraction, which are associated with various dislocation-particle interaction mechanisms (e.g., particle shearing, Orowan looping, dislocation climb, and dislocation detachment) [131]. Previous work studied the effect of the precipitate volume fraction on the creep properties of Fe-Ni-Al-Cr alloys by proportionally adjusting the content of Ni and Al [34]. To the best of our knowledge, no efforts have been made so far to study the influence of Al on the microstructural parameters as well as on the mechanical properties. Microstructural modification by addition of Al provides a considerable cost advantage over the addition of Ni.

In the present work, the microstructural attributes of NiAl-type *B*2 precipitates and corresponding creep properties of the alloys are investigated and analyzed in six model ferritic alloys with Al content varying from 4 to 10 mass%, which have been designed to achieve improved creep resistance. The objectives are to investigate the interrelationships among composition, microstructure, and mechanical properties, which facilitates to establish a baseline creep database for further optimization of properties. The primary precipitate attributes are quantified by ex-situ ultra-small-angle X-ray scattering

(USAXS) measurements, using a theoretical model which combines the polydispersity (a monomodal distribution of primary precipitate size) and interference effects of the precipitates (interference between waves scattered by different particles). Complementary transmission-electron-microscopy (TEM) characterizations are carried out to validate the microstructural attributes obtained from synchrotron USAXS experiments, and also to reveal the dislocation-particle interaction mechanisms in the crept alloys. The effect of Al content on the precipitate configurations in the aged specimen is briefly discussed based on the precipitation and coarsening kinetics. The correlation between precipitate parameters and creep behavior is discussed with respect to the magnitude of Orowan stress and diffusion coefficient in the matrix. These results are expected to establish the baseline information for the structure-property relationships and creep behaviors of the designed alloys.

Synchrotron USAXS is selected to quantify the precipitate characteristics (volume fraction, average size, inter-particle distance) due to its unique advantages over small-angle X-ray scattering (SAXS), small-angle neutron scattering (SANS), laboratory X-ray facilities, and transmission-electron microscopy (TEM). USAXS can resolve large-dimension microstructures, including the 130-nm precipitates in the studied alloys, which is below the lower limit of the scattering vector for other small-angle scattering facilities. It probes a large volume (up to a few mm^3 for low absorbing materials) with better statistics compared to the scale of the local structure (several μm) characterized by TEM. A relative high-energy X-ray beam (~ 17 keV) can be utilized to analyze highly

absorbing materials (such as Fe-based alloys), to ensure appropriate transmission (~ 40%) of the X-ray beam through the thin foil. Moreover, USAXS requires a short measuring time in comparison to SANS and TEM, and a smaller quantity of sample than SANS.

4.2 Experimental Methods

The nominal alloy compositions are listed in Table 6 in both mass percent (mass%) and atomic percent (at.%). Composition throughout this Chapter is in mass%, unless specified otherwise. The model alloys contain nominally 10% Ni and Cr, and 3.2% Mo to dilate the matrix (i.e., to reduce the lattice mismatch between β and β′ phases). A small amount of Zr and B was added to introduce ZrB_2 particles for grain boundary pinning. The alloy ingots were fabricated by vacuum arc-melting and then drop cast into a Cu mold. The purity of the starting materials was 99.97%. Rods cut from ingots were sealed under vacuum in quartz tubes and homogenized at 1473 K for 30 minutes, followed by aging at 973 K for 100 hours. The rods were air cooled after the heat treatments.

Creep specimens were cut from the rods into cylinders having a 4-mm diameter and 6-mm height using electrical discharge machining (EDM). Short-time compressive creep tests were conducted to prescreen the creep properties of the different compositions using a Material Testing Systems (MTS) servo-hydraulic testing machine, as shown in Figure 11. A constant compressive load with an engineering stress level of 140 MPa was applied at a constant temperature of 973 K for 100 hours in air. The temperature variation across the

Table 6. FBB alloy nominal compositions [in both mass% (bold) and at.% (in parenthesis)].

Alloys #	Fe	Al	Cr	Ni	Mo	Zr	B
FBB10	**66.3**	**10**	**10**	**10**	**3.4**	**0.25**	**0.005**
	(60.6)	(18.9)	(9.8)	(8.7)	(1.8)	(0.14)	(0.02)
FBB8	**68.3**	**8**	**10**	**10**	**3.4**	**0.25**	**0.005**
	(63.7)	(15.4)	(10)	(8.9)	(1.8)	(0.14)	(0.02)
FBB6.5	**69.8**	**6.5**	**10**	**10**	**3.4**	**0.25**	**0.005**
	(66.1)	(12.7)	(10.2)	(9.0)	(1.9)	(0.14)	(0.02)
FBB6	**70.3**	**6**	**10**	**10**	**3.4**	**0.25**	**0.005**
	(66.9)	(11.8)	(10.2)	(9.1)	(1.9)	(0.15)	(0.02)
FBB5	**71.3**	**5**	**10**	**10**	**3.4**	**0.25**	**0.005**
	(68.5)	(10.0)	(10.3)	(9.1)	(1.9)	(0.15)	(0.02)
FBB4	**72.3**	**4**	**10**	**10**	**3.4**	**0.25**	**0.005**
	(70.2)	(8.0)	(10.4)	(9.2)	(1.9)	(0.15)	(0.03)

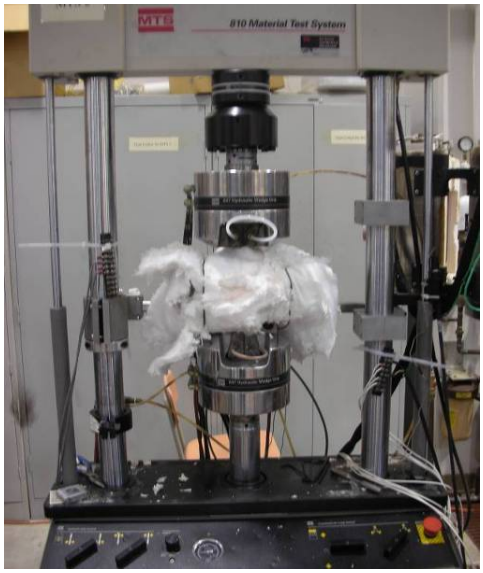

(a)

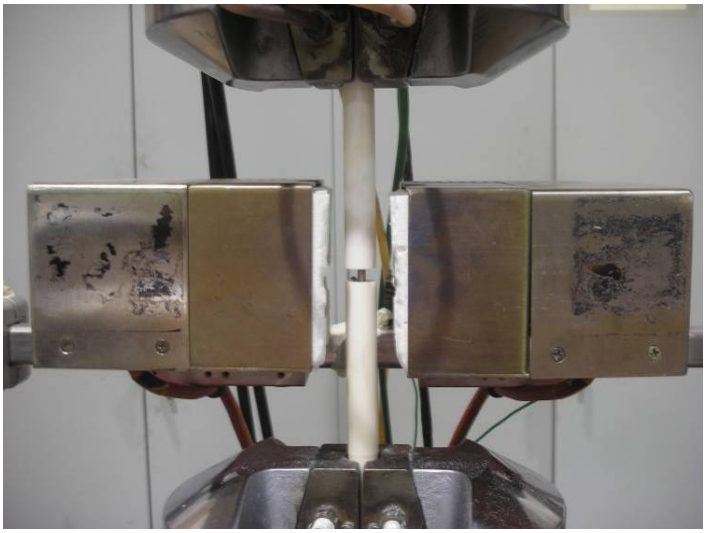

(b)

Figure 11. Experimental configurations of compressive creep experiment under constant load using Material Testing Systems (MTS) servo-hydraulic testing machine: (a) Furnace covered by thermal insulation materials, and (b) a closer look of the cylindrical samples, ceramics grips, and split furnace.

sample was within 2 K, as monitored by a thermocouple attached to the specimen. The size of the cylinder was too small to use a high-temperature extensometer. Instead, the displacement of the crossheads was recorded as a function of time and translated into the creep strain. After the creep test, the sample was cooled in air under an unstressed state. This might have caused a slight relaxation of dislocation substructures.

Foils sliced from rods were ground to a thickness of ~ 50 μm. Fine polishing with P4000 abrasive SiC paper was performed to reduce the contribution from surface scattering to SAXS. Small-angle scattering data were collected at the X-ray Operations and Research beamline, 32-ID-B (presently moved to 15-ID), an Ultra-Small-Angle X-ray Scattering Facility [132] at the Advanced Photon Source, Argonne National Laboratory. A schematic plot of the experimental configuration is exhibited in Figure 12. The beam size was adjusted to the dimension of 1.6 x 0.8 mm. The beam was illuminated at the center of the foils. The measured scattering vector ranged from 10^{-4} to 0.5 $Å^{-1}$. The data acquisition time for each sample was roughly 15 minutes for 200 data points. The data reduction and de-smearing corrections were performed to derive the spectra on the absolute intensity scale using Indra and Irena software packages [132-133].

TEM characterization was performed using a Hitachi 8100 microscope operated at 200 kV. Slices were ground to less than 100 μm in thickness, and thinned by a Fischione dual-jet polisher. An electrolyte containing a 20-volume

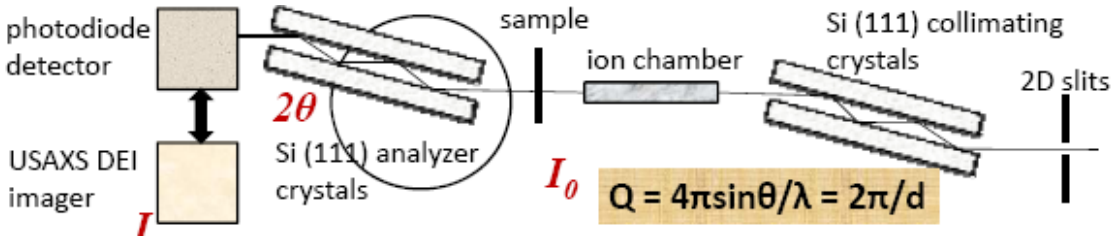

Figure 12. Schematic of the APS USAXS instrument in one-dimensional collimated or USAXS imaging configuration [132].

fraction (vol.%) of the perchloric acid in methanol was maintained at 233 to 238 K, and a voltage of 40 V and a current of 40 ~ 50 mA was applied. For crept materials, foils used for USAXS measurements were further prepared by electropolishing. The electrolyte contained 6% perchloric acid, 60% Methanol, 33.5% ethoxy-ethanol, and 0.5% glycerin in methanol, which was maintained at 243 to 253 K and a voltage of 16 V.

4.3 Results

4.3.1 Theoretical Model and USAXS Analysis

A typical absolute intensity profile from USAXS measurements for the aged FBB6.5 alloy is shown in Figure 13(a) as a function of the scattering vector, *Q*. The profile contains a power-law slope at $Q < 10^{-3}$ Å^{-1} and a broad distinctive peak at a Q range of 10^{-3} ~ 10^{-2} Å^{-1} with a small bump at ~ 7×10^{-3} Å^{-1}. The slope at low *Q* (< 10^{-3} Å^{-1}) represents the scattering from defects or precipitates at the grain boundaries of the polycrystalline Fe matrix. The large peak at 10^{-3} ~ 10^{-2} Å^{-1} is characteristic of the strong interference among the primary β' precipitates, and is indicative of the average inter-particle spacing. In this case, previously used Guinier approximation to obtain the radius of gyration as a measure of precipitate size is rendered inapplicable, since there is a non-dilute number density of precipitates within the grains [134]. Also, the smeared shoulder at ~ 7×10^{-3} Å^{-1} is not consistent with the previously determined inter-particle spacing (~ 10 nm) of hyperfine secondary precipitates as revealed in a previous APT study [27]. Actually, those secondary precipitates have no significant population to generate

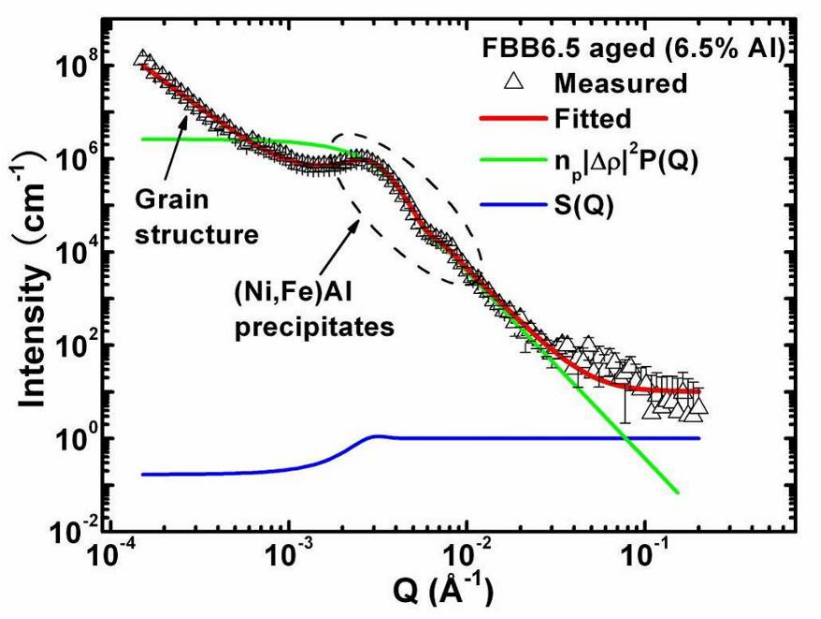

(a)

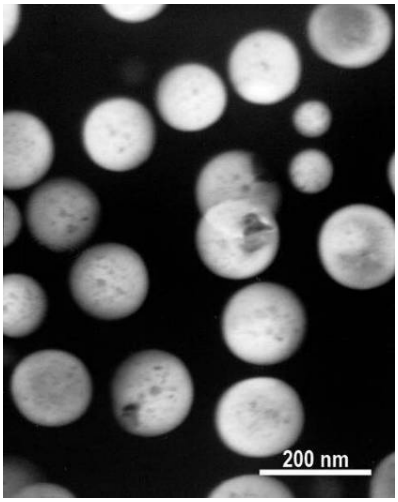

(b)

Figure 13. (a) Measured and fitted absolute intensity profiles for the aged FBB6.5 alloy, along with the scaled form factor and structure factor, and (b) the dark-field (DF) TEM image (using 100_{B2} reflection) showing β′ (bright) particles [27].

detectable scattering signal at Q ~ 0.06 $Å^{-1}$. Rather, the small shoulder on the right side of main scattering peak is indicative of the synergy between the polydispersity of the precipitate size and the variance of the inter-particle spacing. The intensity spectra for all the alloy compositions showed similar characteristic features, except for the position and shape of the correlation peak [see Figure 14].

The precipitate parameters in real space can be extracted from the measured absolute intensity in the reciprocal space using an appropriate theoretical-model fitting. Considering the case of non-dilute precipitates, we apply a model that includes both the polydispersity and interactions among particles. Previous TEM work showed that *B2* precipitates for all the compositions were spherical in shape [27] [see Figure 13(b)]. For spherical particles, the measured absolute intensity can be written as the product of the form factor and structure factor with other scaling parameters as [135]

$$I(Q) = n_p \mid \Delta\rho \mid^2 P(Q)S(Q) + AQ^{-b} + I_b \tag{16}$$

where n_p is the number density of precipitates in the illuminated volume and $\Delta\rho$ is the contrast of the average scattering-length density between the precipitate and the matrix. At small *Q*, the contribution from the scattering of grain boundaries is taken into account by incorporating a term of AQ^{-b} into the equation, where *b* is a parameter representing the fractal information of the grain-boundary surface, *A* is the scattering amplitude for the grain-boundary scattering, I_b is the scattering intensity background, and *P(Q)* is the average form factor depending on the

shape and size distribution of the particles. The normalized form factor for a spherical particle is given by

$$F(Q,x) = \left[\sin(Qx) - Qx\cos(Qx)\right]/(Qx)^3 \tag{17}$$

where x is the individual precipitate radius. Considering that the precipitates exhibit a polydisperse size distribution, as evident by the TEM characterization, a normal distribution (Gaussian law) is assumed with an average particle radius, R, and standard deviation of particle radius, δ, as

$$N(x,R,\delta) = \exp\left[-(x-R)^2/2\delta^2\right]/\sqrt{2\pi\delta^2} \tag{18}$$

Therefore, the form factor for the overall contribution to intensity is written as

$$P(Q) = \left(\frac{4\pi}{3}\right)^2 \int F^2(Q,x)\cdot N(x,R,\delta)\cdot x^6 dx \tag{19}$$

$S(Q)$, the structure factor representing the inter-particle correlations, is calculated by a stochastic phenomenological model [136]

$$S(Q,L,\sigma) = 2\left\{\frac{1-\exp\left[-\left(Q^2\sigma^2\right)/4\right]\cos(QL)}{1-2\exp\left[-\left(Q^2\sigma^2\right)/4\right]\cos(QL)+\exp\left[-\left(Q^2\sigma^2\right)/2\right]}\right\} - 1 \tag{20}$$

where L is the average inter-particle spacing and σ is the standard variation of L. Eq. (20) originates from the assumption that the particles are partially ordered with an average separation distance [136]. Such a structure factor has been previously applied to a Ni-based superalloy system strengthened by ellipsoid precipitates, which provided predictions on precipitate parameters and were subsequently validated by TEM [135]. From Eqs. (16) – (20), the measured absolute intensity can be fitted by this model with eight parameters: $n_p|\Delta\rho|^2$, R, δ, L, σ, I_{INC}, b, and A, employing a nonlinear least-square fitting method.

As exhibited in Figure 13(a), there is good agreement between the fitted data and desmeared spectra from the USAXS measurement. Figure 14 displays the USAXS-intensity profiles measured and fitted for the alloys with varying amounts of Al. The reduced χ^2, which represents the goodness of fit, is close to 1 for all the fitting. Note that the intensities are rescaled for clarity. The values for the power-law slopes at low *Q* and the background at high *Q* are similar for all the alloy compositions. With increasing Al concentrations, the peak shifts to the high *Q* region, indicating that the inter-particle spacing becomes smaller.

Table 7 summarizes the values for the average precipitate diameter, average inter-particle spacing calculated from the USAXS spectra, and their corresponding standard deviations. Average diameters obtained from TEM experiments are also listed for comparison. Even though TEM data are based on a finite number of precipitates (less than 100), those obtained from the USAXS data are in good agreement with the former. This trend provides further verification for the underlying model used to deconvolute the USAXS spectra for an accurate determination of precipitation attributes.

The intensity profile does not only include the phase contrast between the matrix and the precipitates, but also reflects the scattering from grain boundaries as implied by the slope at low Q. Therefore, it is not reliable to apply Porod's invariant [137] (with the knowledge of the matrix-precipitate scattering contrast, $\Delta\rho$) to derive the precipitate volume fraction. However, the volume fraction of the precipitates from the precipitate parameters can be obtained, using the following

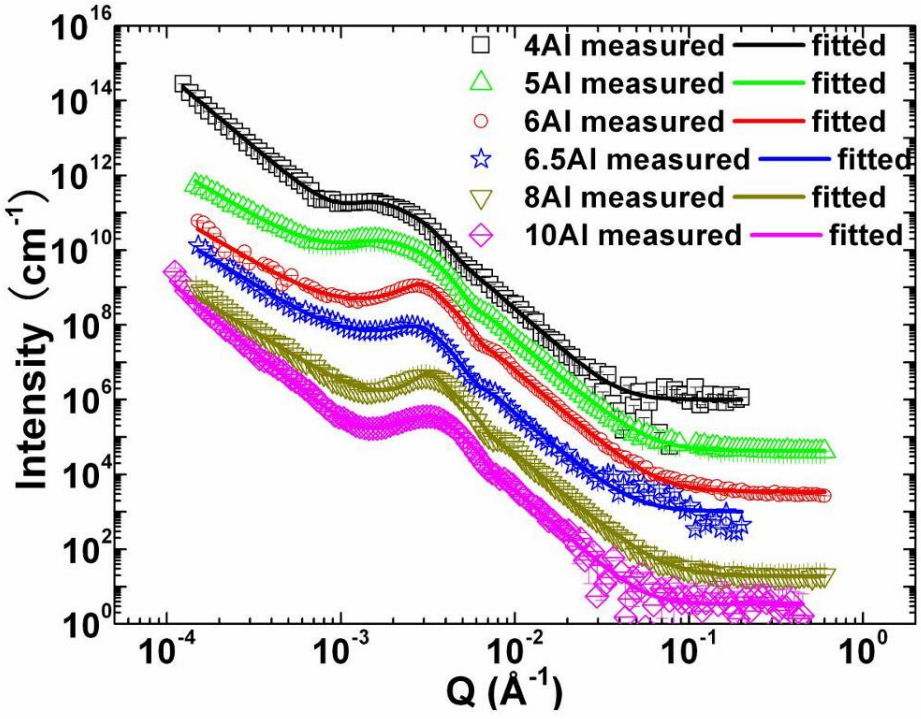

Figure 14. Measured and fitted absolute intensity profiles for aged ferritic alloys with different Al%. Note that the intensities are rescaled.

Table 7. Primary precipitate parameters (average diameter, *2R*, standard deviation of diameter, *2δ*, average inter-particle spacing, *L*, standard deviation of spacing, *σ*, and vol.%) of the aged FBB alloys determined by USAXS, TEM, and AEM [26]. The uncertainties of USAXS results are obtained from non-linear least-square fitting (units: nm).

Alloys	Parameters	2R	2δ	L	σ	Vol.%
4	USAXS	152.4 ± 6.2	38.4 ± 4.4	302.0 ± 11.5	174.0 ± 5.3	10.5± 0.8[+]
	TEM/AEM	148	43	-	-	13.5[#]
5	USAXS	127.4 ± 3.8	34.8 ± 2.8	229.5 ± 14.0	196.5 ± 10.6	10.4± 0.8[+]
6	USAXS	111.0 ± 3.0	32.0 ± 2.2	186.6 ± 3.2	89.2 ± 2.1	15.1± 0.7[+]
6.5	USAXS	129.8 ± 4.2	30.0 ± 3.4	175.0 ± 4.9	101.7 ± 3.6	17.8±1.0 [+]
	TEM/AEM	130	25	-	-	17.8[#]
8	USAXS	99.4 ± 1.5	24.4 ± 1.2	178.5 ± 1.5	74.2 ± 1.9	13.4± 0.4[+]
	TEM	105	25	-	-	-
10	USAXS	89.4 ± 2.4	26.2 ± 2.4	165.9 ± 1.8	82.9 ± 1.2	12.9± 0.6[+]
	TEM/AEM	93.3	22.1	-	-	17.9[#]

+ Based on USAXS data by Eq. (21).

Measured by AEM [26].

equation, while assuming that the normal distribution of the particle diameter and inter-particle spacing are independent of each other,

$$f = \int_0^\infty \int_0^\infty \frac{4\pi x^3}{y^3} \cdot \frac{\exp\left[-(x-R)^2 / 2\delta^2\right]}{\sqrt{2\pi\delta^2}} \cdot \frac{\exp\left[-(y-L)^2 / 2\sigma^2\right]}{\sqrt{2\pi\sigma^2}} dxdy \qquad (21)$$

The calculated volume fractions of precipitates for various alloys are listed in Table 7. The results of volume fractions from USAXS show a qualitative agreement with 13.5%, 17.8%, and 17.9% for alloys FBB4, 6.5, and 10, respectively, which were previously reported based on the quantitative analysis of the compositions of matrix and primary precipitates in an analytical electron microscope (AEM) [26].

The precipitate parameters and volume fractions obtained from USAXS are plotted as a function of Al% for the aged alloys in Figure 15. TEM results for the precipitate diameters of the aged alloys are also presented as a reference for comparison with USAXS results. As the Al content increases, there is a ~ 30% reduction in the average precipitate diameter from 150 nm for FBB4 to 100 nm for FBB10, while FBB6.5 appears to have a higher diameter than FBB6 and 8. The average inter-particle spacing shows a ~ 40% decrease from 300 nm to 180 nm with Al increasing to 6.5%, and a slight decrease within the range of 6.5 ~ 10% Al. The corresponding magnitude of the volume fraction determined by Eq. (21) are in the range of 10 ~ 18 %. The volume fraction of the precipitates tends to increase with Al addition up to 6.5%, and remains nearly constant with further addition of Al.

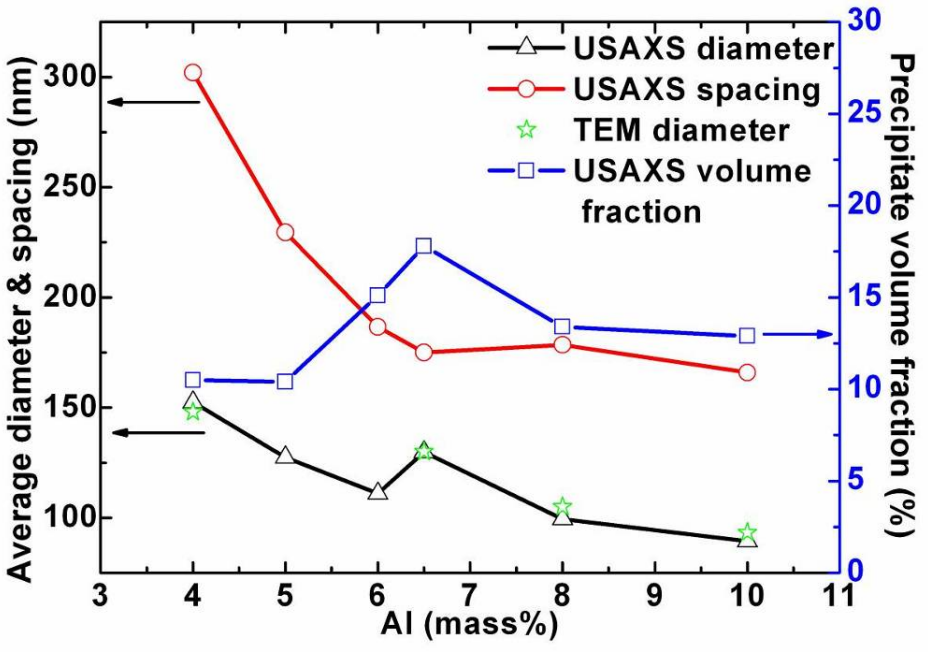

Figure 15. Precipitate parameters and volume fractions obtained by USAXS and measured by TEM as a function of Al%.

The variation of the precipitate parameters before and after creep deformation has been examined. Representative measured and fitted absolute intensity profiles are displayed in Figure 16 (a) ~ (e) for aged and crept alloys, with the peaks magnified at the lower left corner. After creep deformation, a common feature found for all the alloys is that the peak shifts slightly to smaller Q values. The inter-particle spacing increases after creep for alloys with differing Al contents. The average particle size remains constant or exhibits a slight increase, implying that the precipitates coarsened slightly during the 100-hour creep deformation.

4.3.2 Compressive Creep Behavior

Figure 17 shows the compressive creep curves of strain vs. time for the six alloys, at 973K under 140 MPa for 100 hours. All alloys except FBB4 show a brief primary creep, where the strain rate decreases as a function of time, prior to the secondary-creep stage where the strain rate is approximately constant. Either secondary creep or slowly accelerating tertiary creep was observed during the 100-hour tests. The period of secondary creep is shorter for alloys FBB10 and FBB8 in comparison to the other alloys. The accelerated onset and extended period of tertiary creep is usually explained by particle coarsening [138-139] and strain softening micromechanisms (e.g., accumulation of dislocations and cavitations) [140-142].

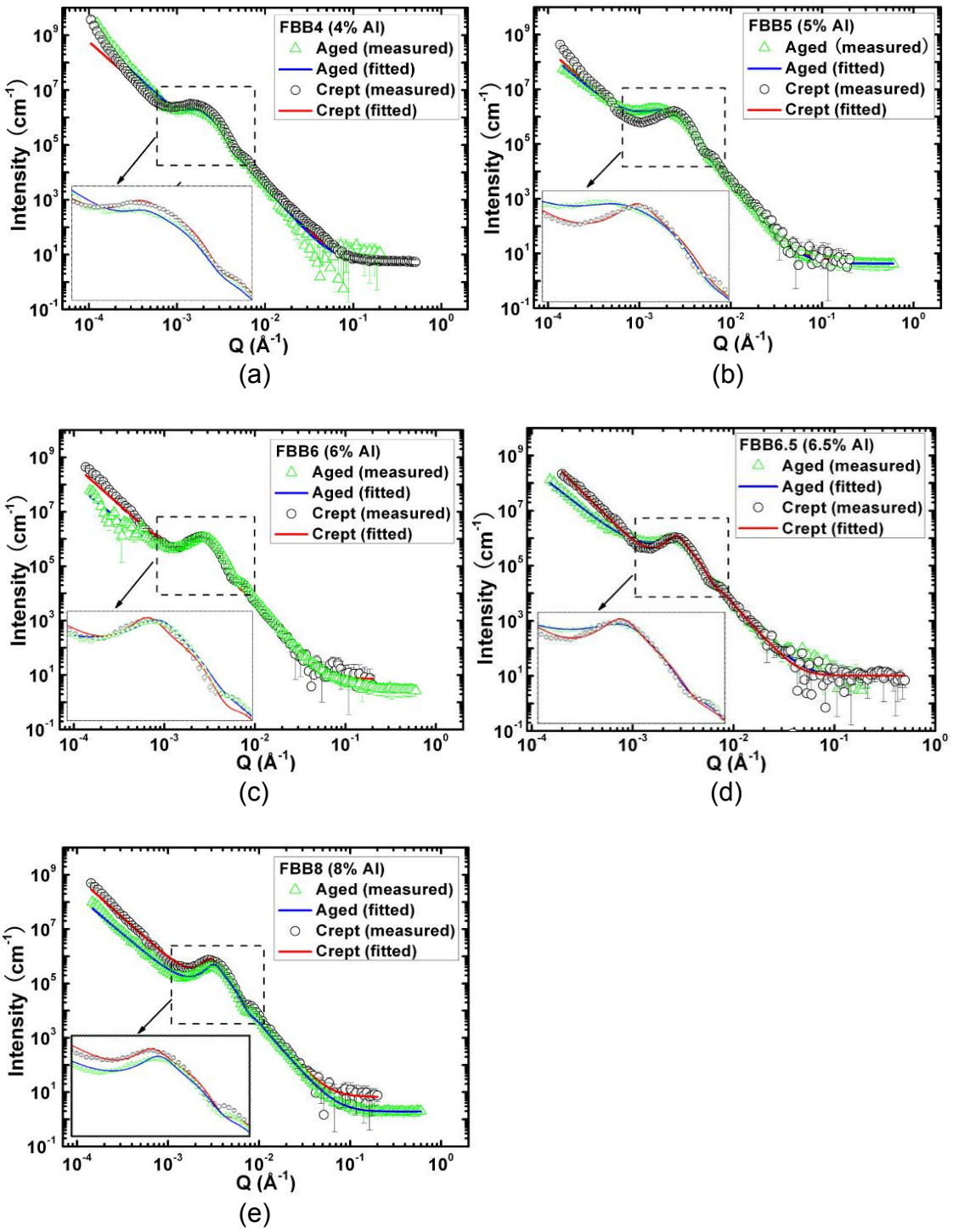

Figure 16. Measured and fitted absolute intensity profiles for aged and crept FBB alloys with 4 ~ 8 mass% Al [(a) ~ (e)].

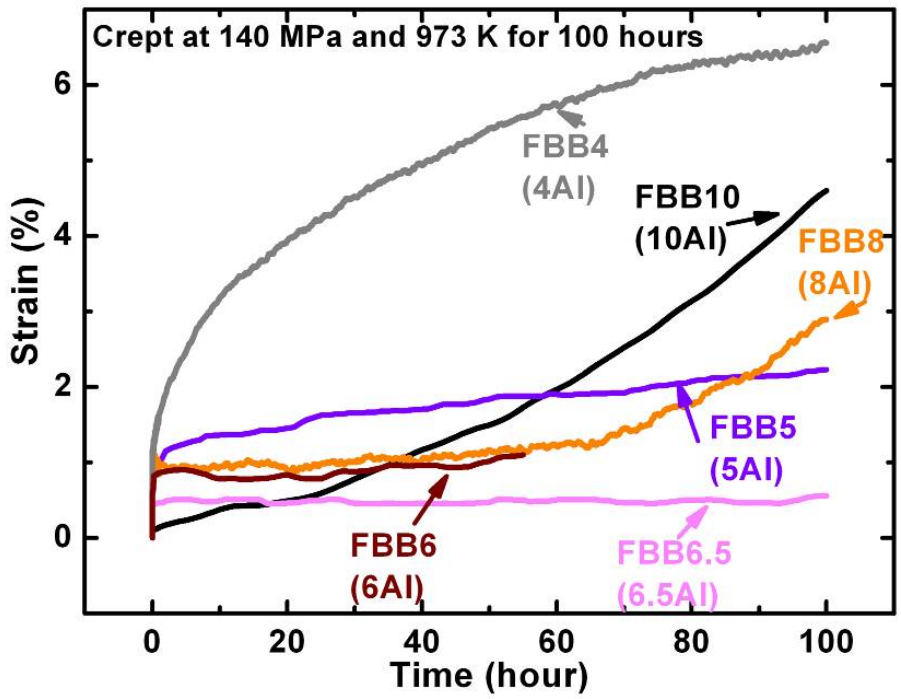

Figure 17. Compressive creep curves at 973 K under 140 MPa for 100 hours; strain as a function of time are plotted for various compositions.

The steady-state creep rate varies by nearly two orders of magnitude (10^{-9} ~ 10^{-7} /s) as a function of Al content. Optimal composition with the minimal secondary creep rate is exhibited by the alloys with ~ 6.5 mass% Al (FBB6.5). For Fe-Ni-Al-Cr alloys with 9 ~ 37 vol.% of precipitates, Stallybrass [34] measured the compressive steady-state creep rates to be in the range of 7.2 x 10^{-5} ~ 2.8 x 10^{-6} /s at 973 K and under 140 MPa. Compared to these results, the present FBB alloys show 1 ~ 3 orders of magnitude lower creep rates with less than 20 vol.% precipitates. Such a significant improvement in creep resistance is likely a result of, among others, the addition of Mo as a solid-solution strengthening element in the Fe matrix. In-situ TEM observations of dislocation motion in an Fe-Mo solid solution at high temperatures show that dislocation mobility is reduced due to viscous motion of dislocations dragging the solute atmosphere [143]. Creep rates in solid-solution Fe-Mo alloys have been reported to be approximately three orders of magnitude lower than that in α-Fe [144], which is in good agreement with our results.

4.3.3 Dislocation-Particle Interaction Modes

Figure 18 presents a typical feature of the dislocation-particle interaction modes in the secondary creep regime as determined by TEM, which reveals the existence of two types of precipitate strengthening mechanisms: dislocation loops bowing out between particles (indicated by red arrows) and dislocation climb around particles (indicated by blue arrows). However, it is not possible to conclusively determine which is the dominant mechanism between the two

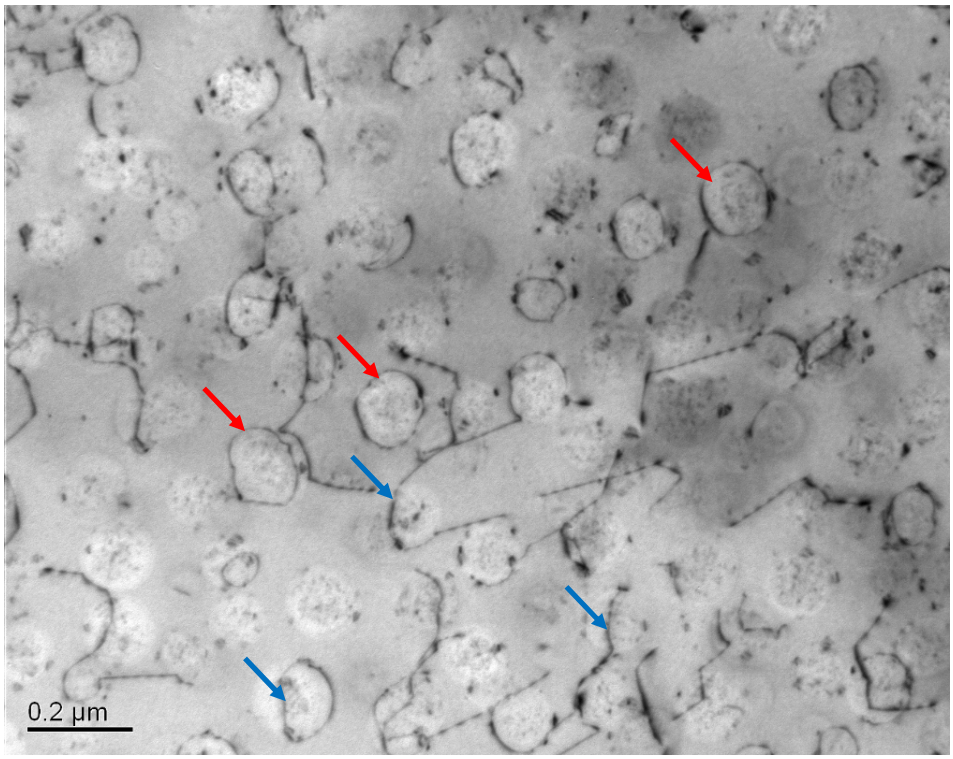

Figure 18. Bright-field (BF) TEM images taken with a 110 diffraction vector near the [001] zone showing dislocation-particle interactions identified as dislocation loops (red arrows) and dislocation climb around particles (blue arrows) in the compressively crept FBB8 alloy at 973 K and under 140 MPa.

interaction modes. It should be noted that particle shearing was not observed, which is probably due to the coarse size of the precipitates. The TEM results are consistent with Zhu's investigations, which suggested that the operative mechanism under low stresses (e.g., 60 MPa, 923 K, and 100 MPa, 873 K) is dislocation climb. The feature of Orowan looping at high stresses (e.g., 140 MPa, 873 K) was also reported [35].

4.4 Discussions

4.4.1 Effect of Al on Precipitate Volume Fraction and Size

The rise of the volume fraction of precipitates as Al increases from 4 to 6.5% is likely due to more Al atoms forming *B2* precipitates together with the Ni atoms in the matrix. With further addition of Al beyond 6.5%, the precipitate volume fraction saturates due to the lack of the further availability of Ni in the matrix; consequently, the excess Al atoms remain in the matrix. This trend is consistent with the published results that the matrix composition is indeed enriched with 18.6 atomic percent (at.%) Al in FBB10, compared to 8.2 and 4.7 at.% in FBB 6.5 and 4, respectively (see Table 2 in Ref. [26]).

The precipitate size in the aged specimen is closely related to the diffusional nucleation and growth of the precipitates. The effects of Al content are associated with three distinct aspects: (1) Al affects the composition and volume fraction of the precipitates by partitioning into the precipitate phase; (2) Al in the matrix modifies the composition and diffusion rates of elements in the matrix, and (3) the lattice misfit between the matrix and precipitates changes due

to the different phase compositions. The lattice misfit between the two phases is calculated from the lattice parameters measured by neutron diffraction as

$$\delta = 2\frac{a_p - a_m}{a_p + a_m} \tag{22}$$

where a_p and a_m are the lattice parameters of the matrix and precipitate, respectively. The lattice misfits δ at 973 K under zero stress are very similar for FBB4, 6.5, and 10 alloys (-0.0004, 0.0002, and 0.0002, respectively). Therefore, the diffusional nucleation and growth of precipitates can be mainly discussed with respect to the first and second aspects, as discussed above.

From both literature results and our preliminary work, the precipitation of ordered *B2* NiAl intermetallics was observed to occur during the quenching and precipitation kinetics during subsequent aging was fast [18]. The average particle size characterized by TEM in the as-quenched specimen from homogenization at 1473 K is listed in Table 8, together with the ratio of the mean volume of precipitates after 100-hour aging and in the as-quenched specimen, which is a qualitative measure of precipitate coarsening resistance. First, the as-quenched particle size in FBB10 is much lower than FBB6.5 and 8, and the volume fraction is larger (or nearly the same), which possibly indicates a higher nucleation rate in FBB10. According to Equation 5.11 in Ref. [145], the homogeneous nucleation rate in solids is described as

$$N_{\text{hom}} = wC_0 \exp\left(-\frac{\Delta G_m}{kT}\right)\exp\left(-\frac{\Delta G^*}{kT}\right) \tag{23}$$

$$\Delta G^* = \frac{16\pi\gamma^3}{3(\Delta G_v - \Delta G_s)^2} \quad (24)$$

where w is the vibration frequency of the atoms, C_0 is the number of atoms per unit volume in the phase, ΔG_m is the activation energy for atomic migration per atom, ΔG^* is the critical free energy change for homogeneous nucleation, γ is the matrix-precipitate interfacial energy, ΔG_v is the volume free energy reduction per unit volume caused by the formation of a volume of precipitates, ΔG_s is the misfit strain energy per unit volume of the precipitate. If the misfit strain energy is ignored, ΔG^* is inversely proportional to the power of the chemical driving force ΔG_v^2. With the increase of Al concentration, the chemical driving force for nucleation will increase, leading to a reduction of ΔG^* and, thus, an accelerated nucleation rate. Since the precipitate equilibrium volume fraction is comparable for FBB6.5 and FBB10, an increased addition of Al into FBB10 and the resulting high percentage of Al in the matrix [26] can lead to the smaller size of precipitates with a denser distribution, which is consistent with our TEM observations of the as-quenched alloys as shown in Table 8.

Secondly, the ratio of the mean volume of precipitates V_{973}/V_{AQ} for FBB10 is substantially higher than FBB6.5 and FBB8. Since the effect of lattice misfit is ignored due to the subtle difference in various compositions, the coarsening rate of β′ is mainly governed by the diffusion coefficient of the controlled species in the matrix. The rate-controlling diffusion coefficient at 973 K is the self-diffusion coefficient of Fe, which is slower than the solute-diffusion coefficients of Al, Ni,

Table 8. Precipitate size data (mean diameter ± standard deviation, in nm) based on TEM measurements. As a relative measure of coarsening resistance in these alloys, also listed are V_{973}/V_{AQ} [= $(D_{973}/D_{AQ})^3$] the ratio of the mean volumes of precipiates after aging (V_{973}) and in the as-quenched (V_{AQ}) conditions.

Alloy	As-quenched	Aged at 973K/100h	V_{973}/V_{AQ}
FBB6.5	100 ± 18	130 ± 25	2.2
FBB8	95 ± 22	105 ± 25	1.35
FBB10	20.5 ± 4.3	100.3 ± 26.5	117

Mo, and Cr in the Fe matrix (see Figure 5). It has been reported that the self-diffusion coefficient of Fe increases by more than one order of magnitude at 973 K, as Al increases from 6 to 18 at.% (see Figure 2 in Ref. [146]). The accelerated self diffusion of Fe could be associated with the reduction of the vacancy formation enthalpy as Al content increases in the disordered Fe-Al alloys [147]. Therefore, the accelerated coarsening rate is likely due to the enhanced self diffusion of Fe in the matrix, which is induced by the large amount of Al partitioned into the matrix.

4.4.2 Correlation between Precipitate Attributes and Creep Behavior

As discussed in Section 4.4.1, the precipitate volume fraction increases as the Al content increases to 6.5 mass% and saturates with further Al additions, which is primarily due to the lack of concomitant increase in the amount of Ni to form more β´ precipitates.

As described in Section 4.3.4, the dislocation-particle interaction modes during secondary creep regime have been determined through TEM characterization as the combination of Orowan dislocation loop and dislocation climb. These two mechanisms (Orowan looping and dislocation climb) introduce a threshold stress such that the effective creep deformation is initialized only if the applied stress is higher than the threshold stress. The steady-state creep rate for power-law creep considering a threshold stress can be described by

$$\dot{\varepsilon} = B\frac{GbD}{kT}\left(\frac{\sigma_a - \sigma_{th}}{G}\right)^n \tag{25}$$

where B is a dimensionless constant, n is the stress exponent, D is the effective diffusivity of a rate-controlling element in the matrix, T is the absolute temperature, G is the isotropic shear modulus of the matrix, b is the Burger's vector in the matrix, σ_a is the applied stress, and σ_{th} is the threshold stress. The experimentally determined values of n and σ_{th} from tensile creep experiments for FBB6.5 will be reported in Section 5.5.1.

In the following, we focus on the threshold stress described by a variety of models and the dependence of threshold stress on the precipitate volume fraction. Depending on the different types of dislocation-particle interactions (dislocation looping, dislocation local climb, and general climb), the magnitude of threshold stress can have a wide range of values. The dislocation detachment mechanism may be ruled out here as it only applies to incoherent particles. An upper bound of threshold stress is given by the Orowan stress when dislocations bypass particles by bowing out on the glide plane. A lower bound could be a relative small fraction of the Orowan stress for dislocation climb mechanisms (e.g., 0.4 ~ 0.7 for the local climb and 0.004 ~ 0.02 for the general climb mechanisms [131,148]). The Orowan stress is a function of shear modulus, precipitate volume fraction, and particle radius as described by [149]:

$$\sigma_{OR} = \frac{0.81Gb}{\pi\lambda_s(1-\nu)^{1/2}}\ln\left(\frac{1.63r}{b}\right) \tag{26}$$

$$\lambda_s = 0.82\times\left[\left(\frac{\pi}{f}\right)^{1/2} - 2\right]r \tag{27}$$

where λ_s is the square lattice spacing, r is the particle radius, f is the volume fraction, and v is the Poisson's Ratio. Note that r and f are two competing factors that govern the magnitude of Orowan stress. The value of Orowan stress increases with increasing f and decreasing r.

Due to multicomponent nature of our alloys and a creep testing temperature of 973 K, it is necessary to consider the composition and temperature dependence of G, rather than the temperature dependence of pure Fe, in order to estimate σ_{OR} in Eq. (7). In an earlier study, a model to calculate the composition and temperature dependence of G of bcc Fe-based alloys was proposed [150], and it is given by

$$G = \left[10.296 + \sum x_j \left(\frac{dG}{dx_j}\right)_{Total}\right]\left[1 - 0.48153\left(\frac{T}{T_c}\right)\right] \text{ for } T > T_c \quad (28)$$

where x_j is the atomic fraction of Al, Cr, Ni, and Mo in the ferritic matrix, and $\left(\frac{dG}{dx_j}\right)_{Total}$ is the rate of change in shear modulus with composition, and T_c is the Curie temperature. Relevant $\left(\frac{dG}{dx_j}\right)_{Total}$ values were reported previously [150], while T_c is calculated using the kMART database [46,47]. Curie temperautre is calculated to be 945, 897, and 698 K for the ferritic matrix in FBB4, 6.5, and 10 alloys, respectively. The corresponding values for G at 973 K are 28.2, 46.1, and 49.8 GPa for FBB4, 6.5, and 10 alloys, respectively.

Taking v = 0.33, b = 0.2514 nm, and r determined by USAXS, the calculated Orowan stress are 164.6, 195.9, and 144.2 MPa for FBB4, 6.5, and 10, respectively, as shown in Table 9.

For a small applied stress, a threshold stress arises due to an increased dislocation line length, hence an increased total elastic energy, when dislocations climb over particles. The magnitude of the threshold stress, which is relatively insensitive to the precipitate parameters, is determined by the geometric configuration of the dislocation during the climb bypass. For local climb, which assumes a sharp bend of dislocation at the particle-matrix interface, σ_{th} depends on the shape of the particle, and is ~ $0.45\sigma_{or}$ for spherical particles in the combined climb and Orowan bypass model proposed by Arzt and Ashby [48]. Rosler and Arzt [49] suggested that the magnitude of σ_{th}/σ_{or} for local climb is proportional to r/l, where l is the inter-particle spacing. The value r/l is 0.26, 0.34, and 0.25 for FBB4, 6.5, and 10 alloys, respectively, according to the USAXS results.

Assuming the same dominant creep mechanism to be either dislocation local climb, or mixed mode of local climb and dislocation looping, FBB6.5 always has the highest Orowan stress and thus the highest threshold stress due to a high magnitude of precipitate volume fraction and matrix shear modulus as well as an intermediate value of average precipitate size. The correlation between its high magnitude of Orowan stress and optimal creep resistance is clearly apparent, indicating its optimal precipitate configuration to effectively resist dislocation motion.

Table 9. Matrix compositions (in at.%) obtained by AEM (see Table 2 in Ref. [26]), calculated T_c, G, and σ_{OR} for FBB4, 6.5, and 10 alloys.

Alloys #	Fe	Al	Cr	Ni	Mo	T_c (K)	G (GPa)	σ_{OR} (MPa)
FBB4	78.4	4.7	11.5	3.3	2.1	945	49.8	164.6
FBB6.5	75.7	8.2	11.9	2.1	2.1	897	46.1	195.9
FBB10	65.3	18.6	11.6	2.0	2.6	698	28.2	144.2

4.5 Summary

USAXS was used to determine primary precipitate parameters in model ferritic superalloys. A theoretical model that incorporates a polydisperse form factor and a phenomenological structure factor is employed to calculate the precipitate size, spacing, corresponding variance, and volume fraction. The microstructural attributes obtained from USAXS compare favorably with the complementary TEM data. As the amount of Al increases from 4 to 10 wt.% in the alloys, ~ 40% decrease in the average inter-particle spacing and ~ 30% reduction of the particle diameter were observed. The effect of Al on the precipitate size is discussed with respect to precipitation nucleation and coarsening. The alloy with optimal creep resistance is the composition containing 6.5 wt.% Al. Orowan looping and dislocation climb are identified as the dislocation-particle interaction modes. The optimal alloy of FBB6.5 shows a maximum value of Orowan stress, implying that the precipitates configuration in this alloy provides a strong resistance to dislocation motion.

CHAPTER V
IN-SITU NEUTRON DIFFRACTION STUDIES ON CREEP AND TENSILE BEHAVIOR

5.1 Introduction

Further optimization of the creep properties of Fe-Ni-Al ferritic alloys requires a fundamental understanding of the deformation micromechanisms, particularly at the local β and β' levels. Although mechanical behavior of single-phase solid-solution ferritic alloys [151-152] and NiAl intermetallics [153] have been investigated extensively, few studies have explored the deformation of two-phase alloy systems with β and β' phases present in the constrained state [30,34-35]. While these earlier studies focus on the macroscopic deformation behaviors at room temperature and elevated temperatures, none has explored the micromechanisms of deformation and load transfer/partition at the level of polycrystalline grains and local phases inside grains.

Neutron diffraction (ND) provides the crucial information on structural deformation at mesoscopic scales (less than 1 μm), specifically the accurate determination of lattice strains in differently-oriented grains and/or multiple phases. Large beam size and large penetration of neutrons into matters enable the illumination of a substantial quantity of grains, from which structural mechanisms in the bulk can be determined with better statistics. In contrast to the residual stress/strain state measured with ex-situ characterization techniques, in-situ measurements under loading at high temperatures probe the dynamic lattice-strain evolution during deformation. Since diffraction allows the precise

determination of interplanar spacings, it can be used to measure the elastic lattice strains. On the contrary, diffraction is not directly sensitive to plastic deformation, since the shear strain parallel to crystallographic planes induced by slip deformation cannot be directly detected by diffraction. However, local plastic strain of the differently-oriented grains is generally incompatible and, thus, is compensated by elastic lattice strains, which create local residual stresses. Therefore, the effects of plastic deformation on the elastic lattice strain can also be revealed by diffraction measurements.

So far only a limited number of investigations on the creep and high temperature tension of multiphase materials have been carried out using in-situ ND. These studies have successfully captured the diffraction signatures for micromechanisms of plastic deformation from characteristic elastic lattice strains, e.g., variations of slip systems at elevated temperatures [154], interphase load transfer [154], yielding of secondary phase due to dislocation penetration, estimations of the critical resolved shear stress (CRSS) [155] and constrained thermal-expansion coefficients [156].

Strengthening due to precipitates has two underlying mechanisms: (1) the direct interaction between precipitates and dislocations, which can be revealed by analyzing macroscopic mechanical properties and microscopy characterizations, and (2) the load transfer from the soft matrix to hard particles, which can be inferred from ND lattice-strain measurements. In this work, we present the results of the lattice-strain evolution during tension at room and elevated temperatures and tensile creep at 973 K of the ferritic superalloy

containing 6.5 wt.% Al. As discussed in Chapter IV, the alloy with 6.5 wt.% Al has the optimal creep properties. Shift in peak positions during high-temperature deformation is related to the average phase strains, (hkl) plane-specific lattice strains, and intragranular local phase strains to gain insights into the creep and tension deformation micromechanisms. The three types of lattice strains will be elaborately described in Section 5.2. Interphase and intergranular load partition, which are significant to the strength of material at high temperatures, are semi-quantitatively inferred from the measured lattice strains. Meanwhile, a change in peak intensity is associated with texture development, and a change in peak width is correlated with precipitate/grain size and/or non-uniform strain. In order to gain further insights into high-temperature deformation micromechanisms, crystal-plasticity based finite element simulations are applied to calculate the different types of lattice strains as a function of stress and compared to in-situ neutron diffraction results.

5.2 Experimental Methods

The nominal composition of the alloy for in-situ creep and tension experiments is Fe-12.7Al-10.2Cr-9Ni-1.9Mo-0.14Zr-0.024B, in atomic percent (at.%), or Fe-6.5Al-10Cr-10Ni-3.4Mo-0.25Zr-0.005B, in wt.%. This is the composition with optimal creep resistance at 973 K as described in Section 4. The samples for in-situ creep experiments were sliced from the ingots fabricated by vacuum arc melting at Oak Ridge National Laboratory (ORNL). The samples for in-situ tension experiments were cut from the ingot fabricated by induction

melting at Sophisticated Alloys, Inc. Rods cut from the two sources of ingots were sealed in quartz tubes under vacuum for the purpose of subsequent heat treatment. The heat treatment procedures include homogenization at 1473 K for 30 minutes followed by air cooling, and aging at 973 K for 100 hours followed by air cooling. The microstructure of the alloys was revealed by optical microscopy and TEM. The average grain size is ~ 100 μm, and the polycrystalline material is slightly textured. Inside each grain, there is a homogeneous distribution of β′ precipitates with an average diameter of 130 nm.

For in-situ creep experiments, screw-threaded cylindrical samples with a gage length of 40 mm and a gage diameter of 6.35 mm were machined. The in-situ ND experiments for creep were conducted at the Spectrometer for Materials Research at Temperature and Stress (SMARTS) diffractometer, at the Los Alamos Neutron Science Center (LANSCE) facility of the Los Alamos National Laboratory. A schematic of the ND time-of-flight experimental setup is presented in Figure 19. In-situ creep experiments were performed in vacuum at 973 K under constant load levels. A constant loading rate of 1 MPa / s was applied for loading up to 107 MPa. After the secondary creep is stabilized at 107 MPa, the stress is increased from 107 to 150 MPa. During creep, the macroscopic strain was measured using a high-temperature extensometer over a gauge length of 10 mm within a measurable strain range of 10%. The cross-head displacement was used to measure macroscopic strains above 10%. The material becomes paramagnetic at 973 K and, thus, the magnetic contribution to the ND pattern can be ignored. The diffraction geometry of SMARTS provides the lattice-strain

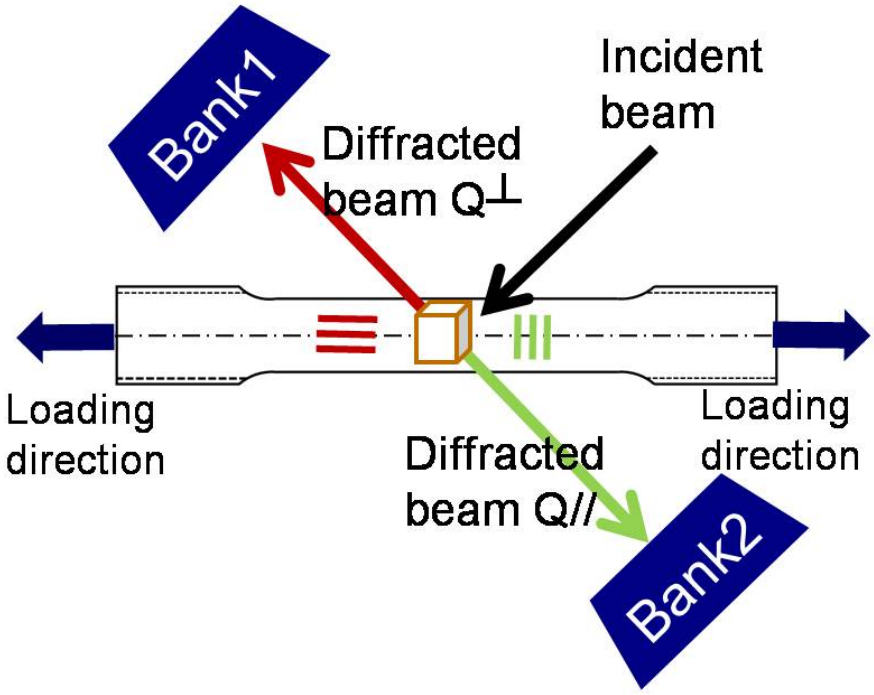

Figure 19. Schematic plot of the experimental setup of time-of-flight neutron diffraction. The scattering angle between the incident beam and the sample axial direction (or loading direction) is fixed at 45°. The incident beam is polychromatic with a range of wave length due to time-of-flight neutrons, which allows the determination of a diffraction pattern covering a wide range of d-spacings. The cube represents a detected volume illuminated by the neutron beam that is defined by the collimator and the beam slit. Detector Bank 1 (or 2) collects diffracted beam from polycrystalline grains with lattice planes parallel to the axial (or transverse) direction [marked by red (or green)]. Lattice plane normal of the diffracted grains is parallel to the diffraction vector, Q. In other words, measured intensity comes from grains whose plane normal is parallel (Bank 2) or perpendicular (Bank 1) to the loading direction.

information parallel and perpendicular to the loading directions (both axial and transverse directions with respect to the sample geometry). The neutron data were collected in batches of 5 minutes during the initial 100 minutes of measurements at 107 MPa, and in batches of 20 minutes afterwards. Diffraction was collected in batches of 5 minutes to capture accelerated lattice-strain changes at 150 MPa. In the 'unloaded' state, the sample was kept under a tensile stress of 18 MPa for proper alignment and maintaining vacuum.

For in-situ tension experiments, screw-threaded cylindrical samples with a gage length of 40 mm and a gage diameter of 6.75 mm were machined. The neutron-diffraction experiments were conducted at the VULCAN Engineering Diffractometer of the Spallation Neutron Source, ORNL, with the state-of-art thermomechanical-loading capabilities. Experimental configuration is similar to the schematic shown in Figure 19. Neutron data were detected in the high-intensity mode using a 20 Hz frequency of chopper, which selects the wavelength of the incident neutron beam. The incident beam size was controlled by a 5-mm collimator and a 6-mm horizontal slit, providing an illuminated volume of ~ 250 mm^3 in the material. A room-temperature extensometer was used to measure the macroscopic strain during room-temperature tension, while the cross-head displacement was used to obtain the macroscopic strain at elevated temperatures. Two water-cooled induction-heating coils, parallel to the axial direction, were placed symmetrically above and below the sample, respectively, as shown in Figure 20. The sample threads were screwed inside high-temperature water-cooled grips that were connected to the 100 kN load cell of a

Material Testing Systems (MTS) machine. Considering that heating was conducted in air, and thread ends of the sample were cooled inside the grips, we were initially concerned about the axial temperature gradient within the beam. Therefore, the temperature variation across the sample gauge length was measured by an infrared camera, which was verified to be within 10 K at various testing temperatures up to 1273 K. An example of the infrared camera image is exhibited in Figure 20. Two K-type thermocouples were spot welded at the center of the sample-gauge length and ~ 4 mm away from the center, respectively. The central thermocouple was used to control the heating of the induction furnace, while the off-central one was used to monitor the temperature difference with respect to the central one. In-situ tension experiments were performed under a constant load control mode with stepwise-loading steps at 300 (room temperature), 623, 773, 873, and 973 K. Neutron diffraction data were collected for 40 minutes at each stress level. Measurements during unloading were performed at three stress levels, if the sample was not fractured at the maximum load. The VULCAN data-analysis codes in an Interactive Data Language (IDL) were utilized to conduct the single-peak fitting with a Gaussian-type function to derive the position, the full width at half maximum (FWHM), and the integrated intensity of individual hkl peaks. The patterns collected by the two detectors were normalized with respect to the proton charge and the Vanadium calibration pattern, in order to eliminate the influence of the variation of the neutron flux and the detector efficiency, respectively. Thus, the normalized intensity was in an arbitrary unit, and the relative evolution of the peak intensity could be obtained.

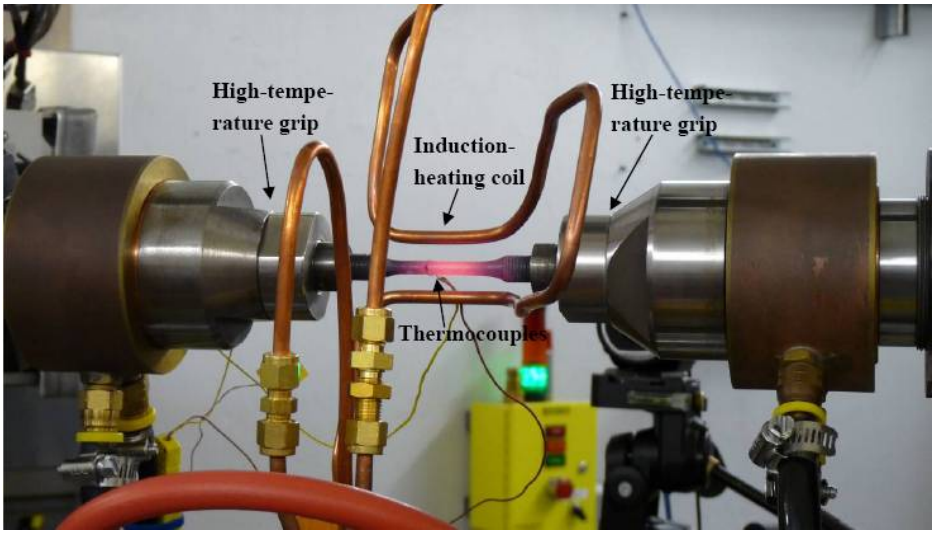

(a)

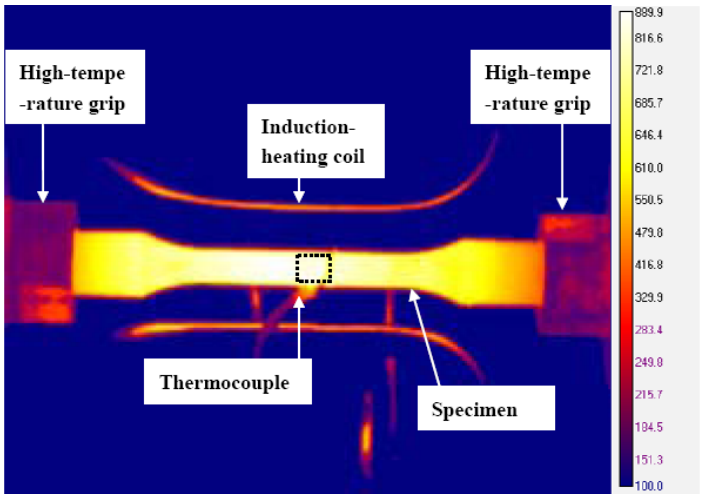

(b)

Figure 20. (a) Experimental setup showing a sample loaded on the grips and heating coils placed along the axial direction above and below the sample; and (b) Infrared-camera image of the loaded sample with a heating temperature of 1163 K. The temperature gradient along the sample-gauge length is clearly shown by the color scale (unit: °C). The temperature variation inside the neutron beam marked by dashed lines (~ 7 mm along the axial direction) is within 10 K.

The typical ND pattern measured at SMARTS is exhibited in Figure 21(a), together with GSAS Rietveld refinement. Due to the coherency between the precipitates and the matrix, overlapping β and β′ peaks (e.g., 110, 200, 211, 220, and 310 peaks) were observed as fundamental reflections, while low-intensity β′ peaks (e.g., 100, 111, and 210 peaks) were detected as superlattice reflections. Typical ND pattern detected at VULCAN is displayed in Figure 21(b), with normalized intensity on a logarithm scale.

Three types of elastic lattice strains [the average phase strain, the (hkl) plane-specific lattice strain, and intragranular local phase strain] are calculated from ND measurements of the polycrystalline multiphase material, as illustrated in Figure 22. The average phase strain is referred to as the lattice strain of an individual phase, volume averaged over all its diffracted aggregates, which represents the bulk behavior of the phase in the constrained state. The average phase strain is determined from the average lattice parameters under deformation, as obtained using whole-pattern Rietveld refinement in the General Structural Analysis System (GSAS) [157]. The average phase strain is given by the following formula

$$\varepsilon = (a - a_0) / a_0 \tag{29}$$

where a_0 is the reference lattice parameter prior to deformation, and a is the lattice parameter as a function of creep time, for the respective phases. The reference lattice parameter a_0 is defined as the lattice parameter measured under a nominal stress (18 MPa for creep and 0 MPa for tension experiments)

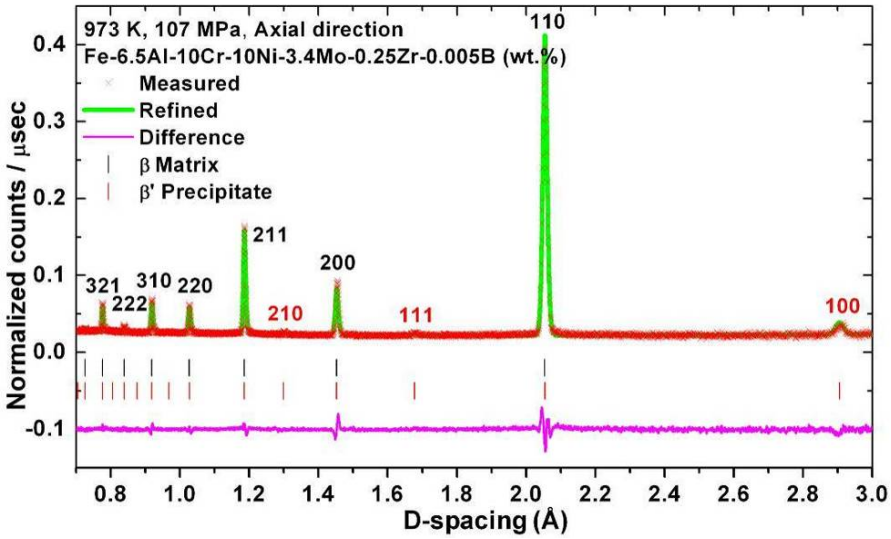

(a)

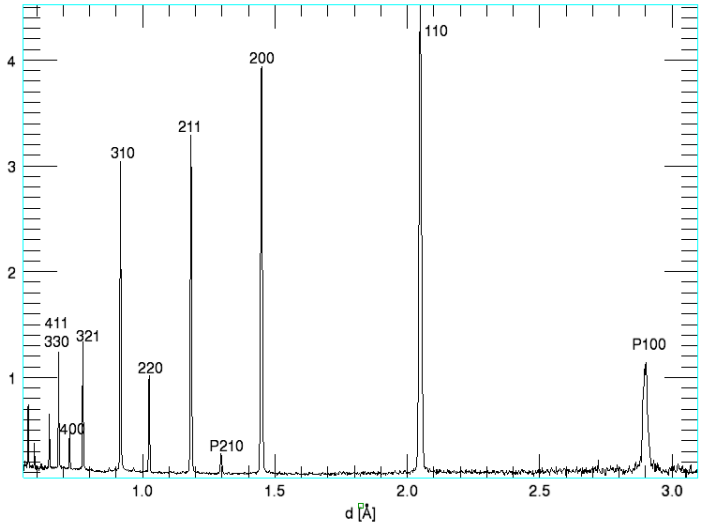

(b)

Figure 21. Typical diffraction pattern measured at (a) SMARTS at 973 K with intensity on a linear scale, and (b) VULCAN at 623 K with normalized intensity on a logarithm scale. Precipitate superlattice 100 and 210 peaks are clearly detected. The fundamental reflections, including 100, 200, 211, 220, 310, 321, and 420 of the matrix are superimposed by the overlapping precipitate peaks.

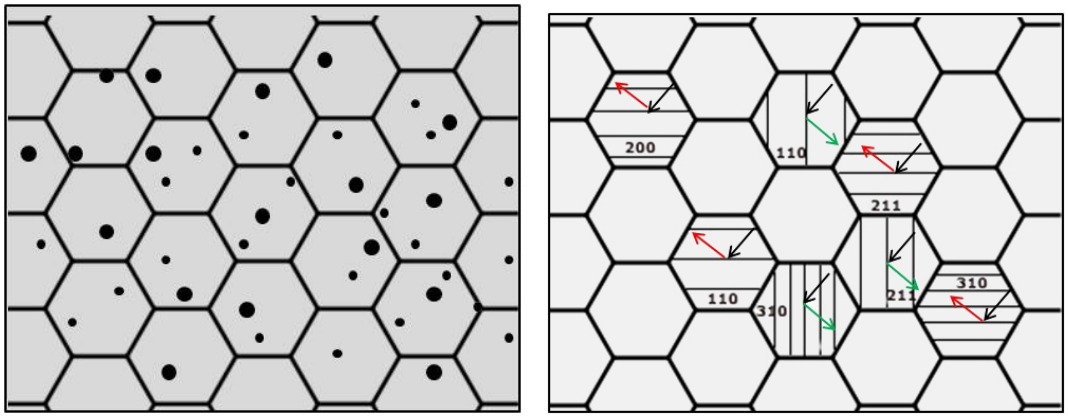

(a) (b)

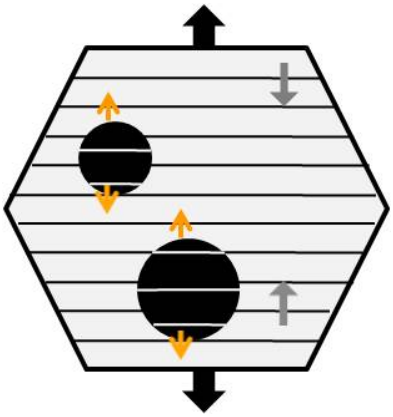

(c)

Figure 22. Three types of elastic lattice strains measured by neutron diffraction are schematically illustrated: (a) the average phase strain, (b) the (hkl) plane-specific lattice strain which reveals the intergranular load partition, and (c) the intragranular local phase strain which reveals the interphase load partition inside a specific (hkl)-oriented grain family. Black circles represent the precipitates, and the hexagons represent grains with different crystallographic orientations.

and at a reference temperature defined for different experiments. The peak-profile function used for Rietveld refinement is a convolution of two back-to-back exponentials with a Gaussian function [157], as described in Appendix A.1. Different variables incorporated in the refinement are the phase weight fraction, spherical harmonics for the texture, and peak-profile parameters. Rietveld analyses provide reasonable values of average β′ phase strains with acceptable uncertainties.

The second type of lattice strain reported here is the (hkl) plane-specific lattice strain. It is grain-orientation dependent and is described as the average lattice strain accumulated in the diffracted grains whose (hkl) plane normals are parallel to the diffraction vector, Q [also denoted as (hkl)-oriented grains]. During deformation of a polycrystalline sample, individual grains with different crystallographic orientations sustain different degrees of strains, depending on the relative orientations between the stress axis and the <hkl> crystallographic poles, elastic anisotropy, and plastic anisotropy [158]. Also, since a grain shares its grain boundaries with neighboring grains, additional strains are generated due to intergranular constraints. Under plastic straining, certain plane-specific lattice strains exhibit nonlinear relations with respect to the applied stress. The deviation from the elastic linearity is attributed to the intergranular strain, which is calculated as the difference between the measured (hkl) lattice strain and the elastic response of lattice strains at the grain level. The (hkl) plane-specific lattice strains represent the average response of β and β′ phases in similarly oriented

grains, and therefore are determined from the overlapping composite peaks through GSAS single-peak fitting as

$$\varepsilon_{hkl} = (d_{hkl} - d^0_{hkl}) / d^0_{hkl} \tag{30}$$

where ε_{hkl} is the lattice strain in the (hkl)-oriented grains, d^0_{hkl} is the reference (hkl) lattice spacing under the unloaded state (under 18 MPa for creep and under 0 Mpa for tension experiments), and d_{hkl} is the (hkl) lattice spacing as a function of creep time or applied tensile stress.

Both (hkl) plane-specific strains and average phase strains are measured along the axial and transverse directions with respect to the sample-loading geometry. Note that the reported lattice strains are not absolute, because any residual strains induced by fabrication and heat treatment at the unloaded state are ignored.

The intragranular local phase strains represent the average lattice strain for β and β′ phases inside specific (hkl)-oriented grain families as

$$\varepsilon_{local\_\beta} = (d^{\beta}_{hkl} - d^{\beta,0}_{hkl}) / d^{\beta,0}_{hkl} \text{ and } \varepsilon_{local\_\beta'} = (d^{\beta'}_{hkl} - d^{\beta',0}_{hkl}) / d^{\beta',0}_{hkl} \tag{31}$$

Determination of this type of lattice strain highly relies on the accurate separation of the overlapping peaks at fundamental reflections. As shown in Figure 23, attempts were made to separate the 200 peak using the summation of two Gaussian profiles calculated with similar methods as described in Ref. [159]. The 200 β′ peak position is obtained from the corresponding 100 β′ superlattice peak position. The ratio of integrated intensity ratio for 200 β and β′ peaks, $I^{\beta'}_{200} / I^{\beta}_{200}$,

are fixed as a constraint in the least-square fitting. The ratio $I_{200}^{\beta'}/I_{200}^{\beta}$ is calculated with known precipitate volume fraction obtained from AEM analysis as

$$\frac{I_{200}^{\beta'}}{I_{200}^{\beta}}=\frac{F_{200}^{\beta'}}{F_{200}^{\beta}}\frac{V_f}{1-V_f} \tag{32}$$

where $I_{200}^{\beta'}$ and I_{200}^{β} are the integrated intensities of 200 β and β′ peaks, respectively; V_f is the precipitate volume fraction; F_{200}^{β} and $F_{200}^{\beta'}$ are the diffraction structure factors for (200) reflections in solid solution bcc Fe and NiAl *B2* precipitates, respectively, which are functions of composition and atomic site occupancy. The compositions of the matrix and the precipitate were obtained from AEM and APT characterizations [26]. Atomic site occupancy in disordered bcc Fe is not a concern. For precipitates, we assume that the solid solution Fe atoms occupy both the Ni and Al sites. Therefore, the structure factors for β and β′ phases can be calculated as

$$F_{200}^{\beta}=2\left(x_{Fe}b_{Fe}+x_{Al}b_{Al}+x_{Ni}b_{Ni}+x_{Mo}b_{Mo}+x_{Cr}b_{Cr}\right) \tag{33}$$

$$F_{200}^{\beta'}=x_{Al}b_{Al}+x_{Fe}^{Al}b_{Fe}^{Al}+x_{Ni}b_{Ni}+x_{Fe}^{Ni}b_{Fe}^{Ni} \tag{34}$$

where *x* is the atomic percentage of a specific element in the matrix or on the cornor/center atomic sites in the precipitate, and *b* is the neutron scattering length for a specific element. Using non-linear least square fitting, the peak position of 200 β phase can be derived.

Analoguous to the γ/γ′ Ni-based superalloys, the constrained lattice misfit between β and β′ phases influences the shape and size of β′ precipitates, their interaction with dislocations, mechanical properties, and creep resistance at high

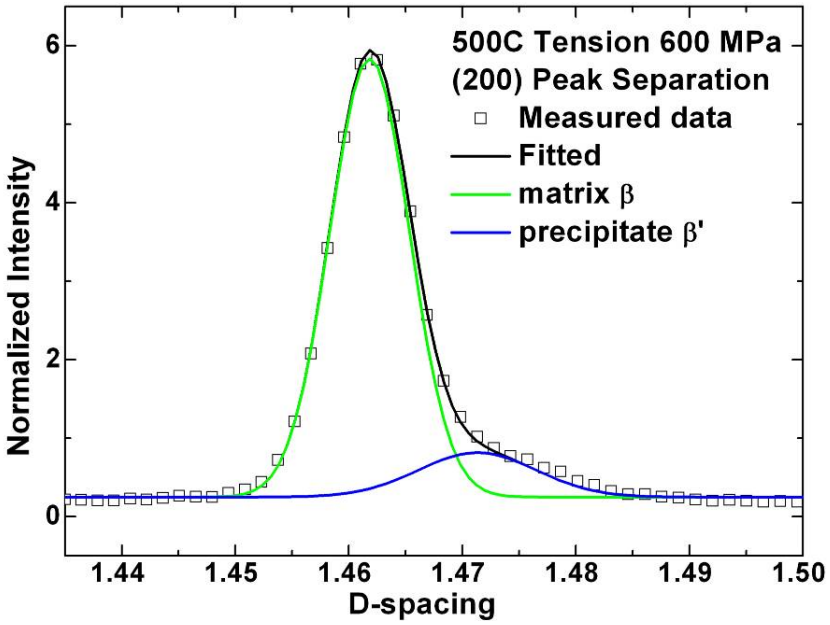

Figure 23. An example showing the separated 200 peaks belonging to the matrix and the precipitate phases, measured at 773 K under applied tensile stress of 600 MPa. Each pattern is batched for 40 minutes of collection time at VULCAN.

temperatures. Low misfit is beneficial with respect to the coarsening resistance and microstructure stability of precipitates. The lattice-misfit evolution during creep deformation is monitored within in-situ ND measurements. Average lattice misfit is obtained by the relative lattice-parameter difference in the two phases as

$$\delta = 2\left(a_{\beta'} - a_{\beta}\right)/\left(a_{\beta'} + a_{\beta}\right) \tag{35}$$

where δ is the lattice misfit; α_{β} and $\alpha_{\beta'}$ are the lattice parameters of β and β′ phases refined by the Rietveld fitting, respectively. Note that the lattice misfit herein calculated describes the relative difference between the volume-averaged lattice parameters of all the diffracted β grains and β′ precipitates. Average lattice misfit is, thus, a measure of the difference in the average phase strains of the two phases, and therefore related to the residual strain fields in the two phases.

In comparison, the local lattice mismatch between β and β′ phases inside specific (hkl)-oriented grain families is calculated as

$$\delta_{hkl} = 2\left(d_{hkl}^{\beta'} - d_{hkl}^{\beta}\right)/\left(d_{hkl}^{\beta'} + d_{hkl}^{\beta}\right) \tag{36}$$

Local lattice misfit is, thus, a measure of the difference in the intragranular local phase strains, and reflects the interphase load transfer inside specific grain orientations.

5.3 Description of Crystal-Plasticity Finite-Element Simulation

Finite element simulation based on crystal plasticity (CPFEM) is utilized to simulate the elastic-plastic response of (hkl) lattice strains as a function of stress and to compare with experimental results. The crystal plasticity model considers the slip deformation inside each grain and the yielding sequence of different

grains as governed by the grain orientation and the Schmid factor of specific slip systems. Development of intergranular strain caused by short-range grain-grain interactions due to the geometric constraints (incompability) of grain boundaries can be captured by this model. The framework of CPFEM methodology and the constitutive equations governing deformation within grains were elaborately described in the papers published by Pierce et al., Bower and Wininger, and Zheng et al [160-162]. A summary of the methodology is presented in the Appendix A.2. According to the constitutive law as reported by them, the elastic deformation gradient is determined by a relationship between the stress tensor obtained from Hooke's Law and the Cauchy stress. The plastic deformation gradient is determined by a summation of strain over the total number of slip systems, with regard to their respect products of slip direction, slip plane normal, and slip strain rate. The slip strain rate considers the power-law flow rule and the Pierce-Asaro-Needleman hardening law containing latent and self hardening.

We follow their work and further modified the ABAQUS user-defined material (UMAT) subroutine to take into account the two phases with different material attributes. The system is a polycrystalline aggregate containing 1000 cubic grains with random texture, as illustrated in Figure 24. There are 3 x 3 x 3 grids, or equivalently 27 elements, in each grain. 5 elements are randomly assigned with the material parameters of the precipitate phase according to the volume fraction of ~ 18%, and the remaining elements are assigned with the matrix material parameters. Elements inside each grain have the same crystallographic orientation, which mimics the cube-on-cube orientation of the

matrix and the precipitates in the real alloy system. The calculated (hkl) lattice strain is a volume average of the projected elastic strains in a subset of grains whose (hkl) plane normal is parallel to the diffraction vector Q. To ensure that 1% ~2% of the total grains can be selected for each <hkl> direction, we assign grain orientations within a difference of 5° relative to each <hkl> direction. Similarly, different subsets of elements represent the matrix and precipitate phases with specific <hkl> orientations are volume averaged to calculate the intragranular local phase strain. Input material parameters for CPFEM include stiffness C_{11}, C_{12}, and C_{44}, as the single crystal elastic constants for cubic materials, the stress exponent N, the initial hardening modulus h_0, the initial slip strength τ_0, the saturation slip strength τ_s, and the latent hardening parameter q, for both the matrix and the precipitate phases.

Since there are no available experimental data of the single crystal elastic constants for solid solution Fe matrix dissolved with Ni, Al, Mo, Cr, and NiAl precipitates containing Fe, we estimate their stiffness coefficients from the polycrystalline diffraction data, as the required input for CPFEM simulation. This type of calculation is of practical importance because single crystal elastic constants are usually not available for many multicomponent polycrystalline materials, in particular newly designed alloys. The reason is more or less associated with the difficulties in fabricating single crystals with exactly the same composition, necessary size, purity, and shape, for elastic constant measurements by acoustic methods. The available single crystal elastic constants at high temperatures are even rare. Voigt, Reuss, and Kroner models

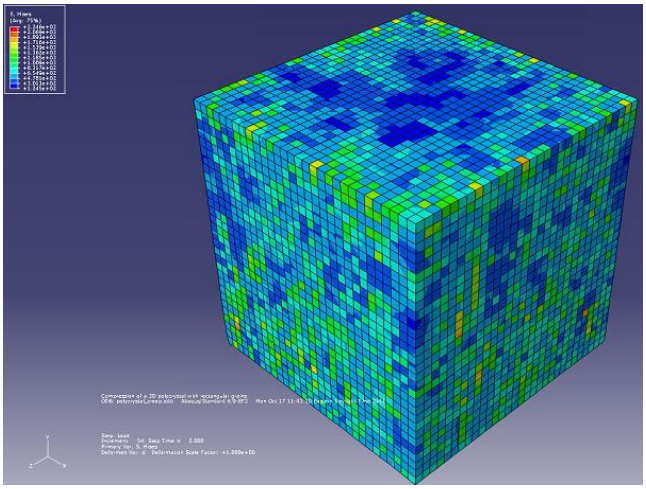

(a)

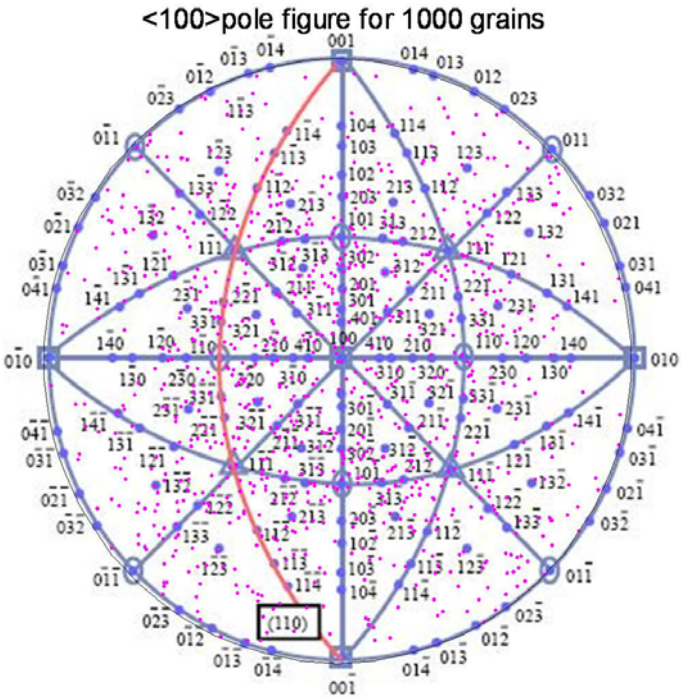

(b)

Figure 24. (a) Contour of σ_{22} for the 1000 cubic-grain model with 3 x 3 x 3 grids inside each grain, under an applied uniaxial stress of 700 MPa, and (b) <100> pole figure of random textured 1000 grains, superimposed on the <100> stereographic projection for cubic materials.

are widely used to calculate the isotropic elastic properties of a polycrystalline bulk material from the single-crystal elastic constants of its individual single crystal grains. To obtain the single-crystal elastic constants from polycrystalline diffraction data is an inverse problem. We follow the method of Ref. [163] within the modified Kronor micromechanical model to determine the single crystal stiffness by least square fitting to the measured orientation-dependent diffraction elastic constants from different (hkl) plane-specific elastic strains measured using in-situ neutron diffraction. The diffraction elastic constants $S_1(hkl)$ and $S_2(hkl)$ are expressed as a function of orientation-dependent Young's modulus E_{hkl} and Poisson's ratio v_{hkl} as

$$S_1(hkl) = -v_{hkl} / E_{hkl} \tag{37}$$

$$\frac{1}{2} S_2(hkl) = \left[\left(1 + v_{hkl}\right) / E_{hkl} \right] \tag{38}$$

The calculation assumes that the polycrystal is texture free and therefore rules out the effect of texture on the diffraction elastic constants. The least square fitting covers the different measured hkl directions, ranging from the most compliant lattice plane (200) in the cubic structure to the most stiff lattice plane (222). Therefore, the results provide an accurate estimation of single crystal elastic constants in both phases. Further refinement of single crystal elastic constants is performed by tuning the values of input stiffness in CPFEM.

5.4 Results: In-Situ Tension

5.4.1 Macroscopic Stress-Strain Behavior

The macroscopic stress-strain behavior during in-situ tension at elevated temperatures conducted at VULCAN was measured from the crosshead displacement of the loading frame. The use of crosshead displacement to measure macroscopic strain is not ideal since the sample experiences a temperature gradient and thus an inhomogeneous deformation along the gauge length. However, in absence of availability of a high-temperature extensometer, a compromise was made. The macroscopic stress-strain curves are displayed in Figures 25 ~ 29 for tension experiments at different temperatures. Here, strain at elevated temperatures was estimated by dividing the crosshead displacement with respect to the sample gauge length, while strain at room temperature was obtained from room-temperature extensometer.

Although use of crosshead displacement limits our ability to accurately determine the magnitude of macroscopic strain, we still can determine the macroscopic yield stress as the deviation from elastic linear response in the stress vs. displacement curves. The macroscopic yield stress from quasi-static tension experiments at VULCAN is shown in Figure 30 as a function of temperature. For comparison, the 0.2% compressive yield stress under a constant strain rate of 1×10^{-4}/s of a Fe-21.5Ni-12.5Al-10Cr alloy (wt.%) as reported by Stallybrass et al. [34] is also shown. Note that yielding is not observed for the currently studied FBB6.5 alloy at room-temperature tension,

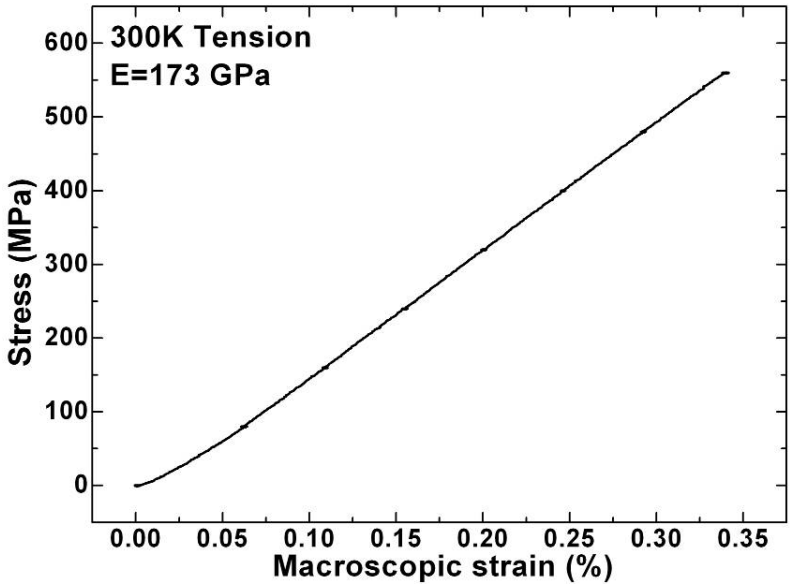

Figure 25. Macroscopic stress-strain curve for quasi-static tension at 300 K.

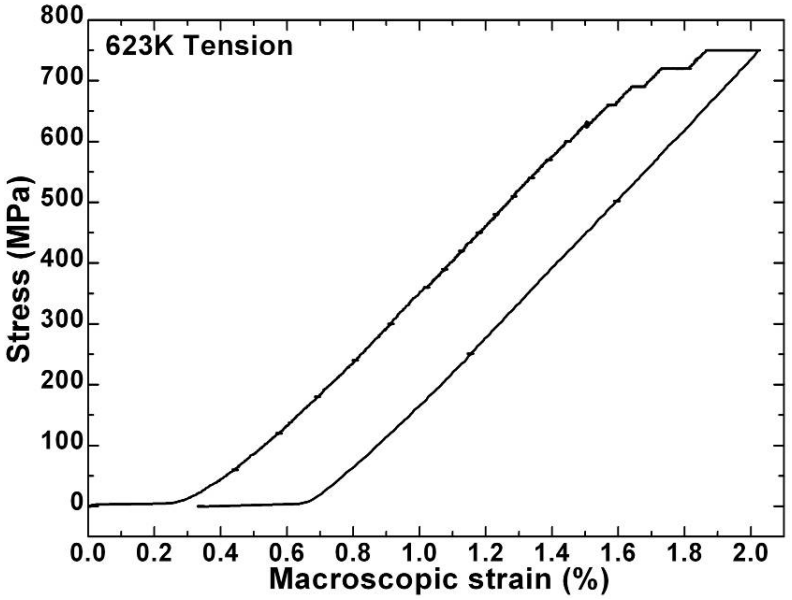

Figure 26. Macroscopic stress-strain curve for quasi-static tension at 623 K. Sample was loaded up to 750 MPa and then unloaded to 0 MPa.

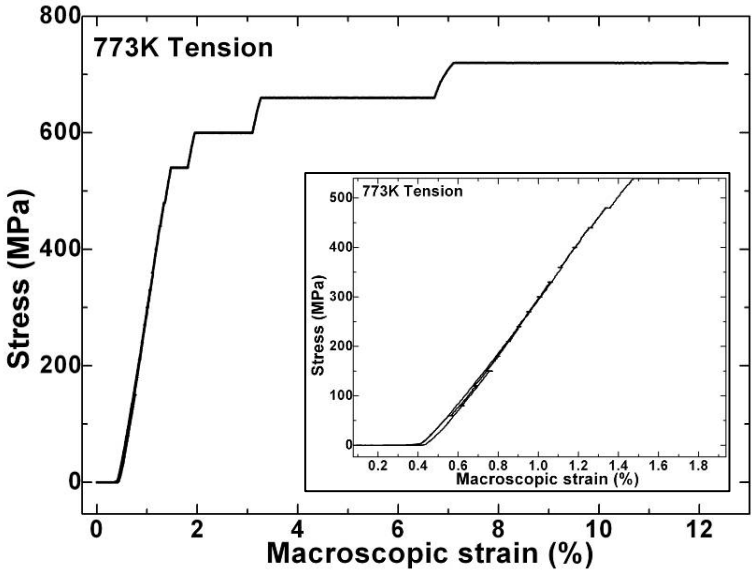

Figure 27. Macroscopic stress-strain curve for quasi-static tension at 773 K. Sample was loaded up to 330 MPa and then unloaded to 0 MPa, followed by subsequent loading to 360 ~ 720 MPa until final rupture. The inset shows a magnified curve at stresses below 540 MPa.

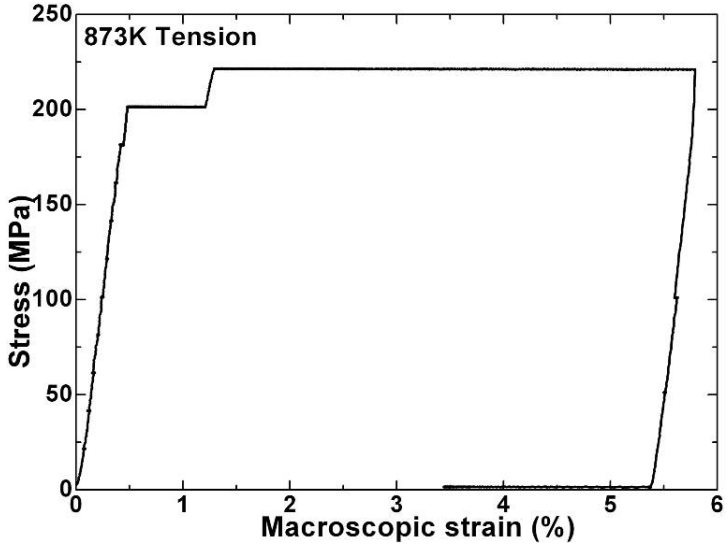

Figure 28. Macroscopic stress-strain curve for quasi-static tension at 873 K. Sample was loaded up to 220 MPa and then unloaded to 0 MPa.

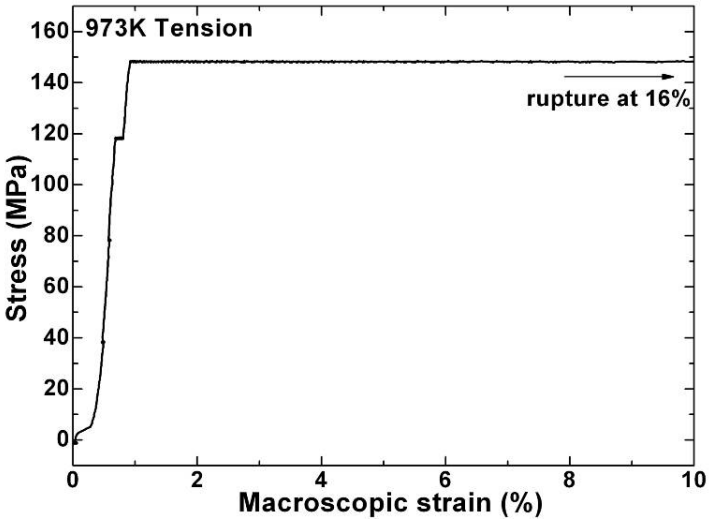

Figure 29. Macroscopic stress-strain curve for quasi-static tension at 973 K. Sample was loaded up to 150 MPa until final rupture at an elongation of 16%.

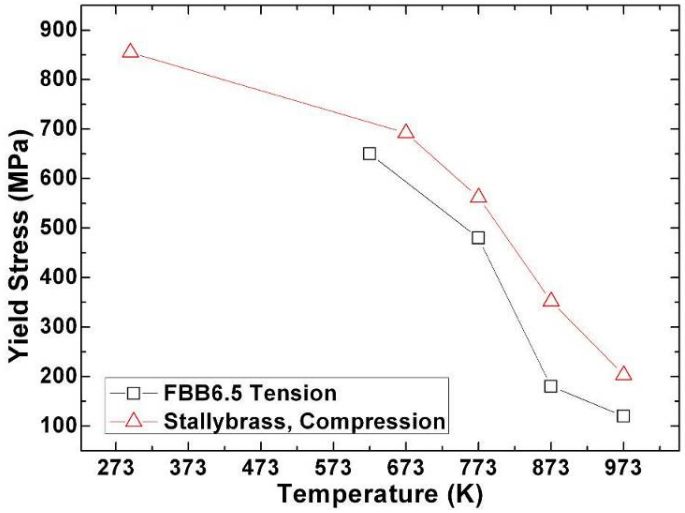

Figure 30. Macroscopic yield stress as a function of temperature for the quasi-static tension experiments at VULCAN (indicated by black square). The 0.2% yield stresses of a Fe-21.5Ni-12.5Al-10Cr alloy (wt.%) under compression and constant strain rate of 1 x 10^{-4}/s reported by Stallybrass et al. [30] are also plotted for comparison.

which implies that the fracture stress of this material is lower than the yield stress at 300 K. Another duplicate tensile experiment at UTK's lab shows that the sample behaves elastically until fracture at 800 MPa. Although the magnitudes of yield stress under different strain rates cannot be directly compared, the variation of quasi-static tensile yield stress with temperature seems to exhibit the same trend as previously reported for compression experiments. As temperature increases above 873 K, there is a strong decrease in yield strength by 70% ~ 80% relative to the value at 623 K.

5.4.2 (hkl) Plane-specific Lattice Strain

The evolution (hkl) plane-specific lattice strains as a function of stress and temperature are displayed in Figures 31 ~ 35. In the elastic region of tensile deformation, linear response of (hkl) plane-specific lattice strain is observed. The gradient of the stress vs. strain curve is governed by elastic anisotropy. In single crystals, the Young's modulus depends on the specific crystallographic <hkl> orientation according to the following equations,

$$\frac{1}{E_{hkl}} = S_{11} - 2\left(S_{11} - S_{12} - \frac{1}{2} S_{44} \right) A_{hkl} \tag{39}$$

$$A_{hkl} = \frac{h^2k^2 + l^2k^2 + h^2l^2}{\left(h^2 + l^2 + k^2\right)^2} \tag{40}$$

where S_{11}, S_{12}, and S_{44} are the single crystal compliance, and A_{hkl} is the elastic anisotropy factor. In cubic material, (111) plane has A_{hkl} value of 0.333 and the highest Young's modulus, while (100) plane has A_{hkl} value of 0 and the lowest Young's modulus. The elastic anisotropy of <hkl> directions in polycrystalline

materials may differ from the single crystal case, due to the effect of preferred grain orientations or texture.

The values of E_{hkl} for the matrix and precipitate phases are calculated from the measured (hkl) plane-specific lattice strains and the (hkl) lattice strains from superlattice peaks, respectively. The results are summarized in Table 10 as a function of temperature and an ascending sequence of elastic anisotropy factor. The observed (hkl) elastic lattice strains follow the rule of elastic anisotropy, exhibiting a rise in the Young's modulus with increase in A_{hkl}. As temperature increases from room temperature to 973 K, the magnitude of E_{hkl} decreases accordingly due to the thermal vibration of atoms. However there is a substantial softening in the material above the temperature of 873 K. Specifically, the Young's modulus at 973 K drops by almost 50% in the matrix and ~ 58% in the precipitate, relative to room temperature measurements. The percentage of reduction in Young's modulus relative to its room-temperature value is comparable to the reported magnitude of 25% in Cr ferritic steels at 873 K [164]. The elastic behavior of the matrix and the precipitates can be compared by monitoring the peak positions of the principal 200/420 peaks and the 100/210 superlattice peaks. It is observed that the precipitates are slightly softer than the matrix by at most 15% below 873 K, and by at most 28% above 873 K.

The onset of plastic deformation is marked by deviation from a linear gradient of stress vs. strain curve. Plastic deformation occurs on certain preferential slip systems, and the sequence of grain yielding relies on the

Table 10. Orientation-dependent Young's modulus as a function of temperature. Values along the normal direction to (200), (310), (420), (211), (220), and (222) planes are calculated from the overlapping fundamental reflections of bcc lattice. 222 peak shows very low intensity for samples tested at 773, 873, and 973 K, thus are not shown in this table. Values for P(100), and P(210) planes are calculated from the superlattice reflections of *B2* precipitates.

	200	310	420	211	220	222	P100	P210
A_{hkl}	0	0.09	0.16	0.25	0.25	0.33	0	0.16
E_{hkl} (300 K)	140.06	160.77	178.62	206.61	220.26	245.10	118.48	172.41
E_{hkl} (623 K)	112.74	128.21	147.12	171.53	188.68	179.86	113.50	145.99
E_{hkl} (773 K)	105.04	127.71	147.14	167.50	175.44	-	105.15	127.88
E_{hkl} (873 K)	89.29	102.88	121.43	137.17	153.85	-	65.79	119.47
E_{hkl} (973 K)	68.03	86.96	93.10	146.63	127.71	-	48.08	70.92

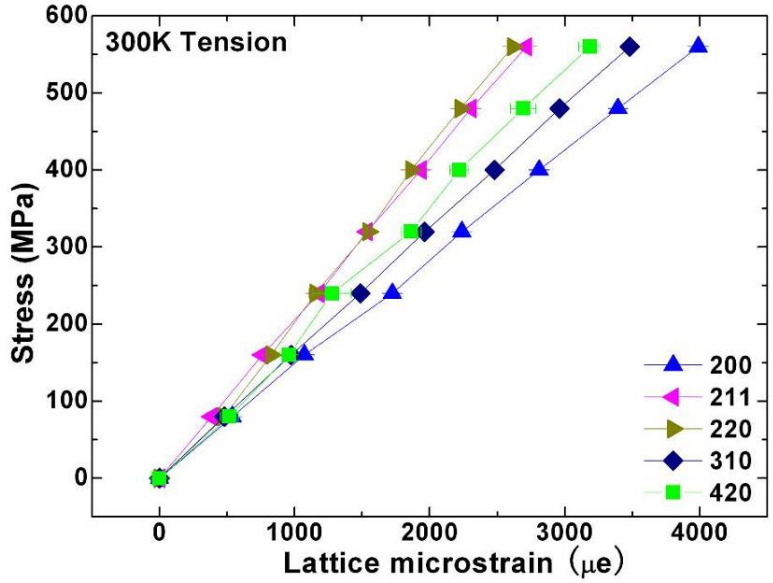

(a)

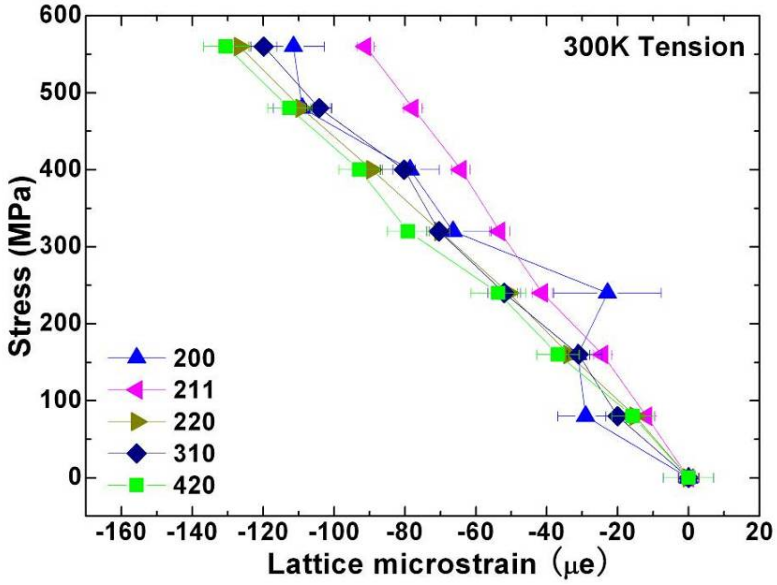

(b)

Figure 31. The response of (hkl) plane-specific lattice strains along axial direction (a), and transverse direction (b), as a function of applied stress during tensile deformation at 300 K (room temperature).

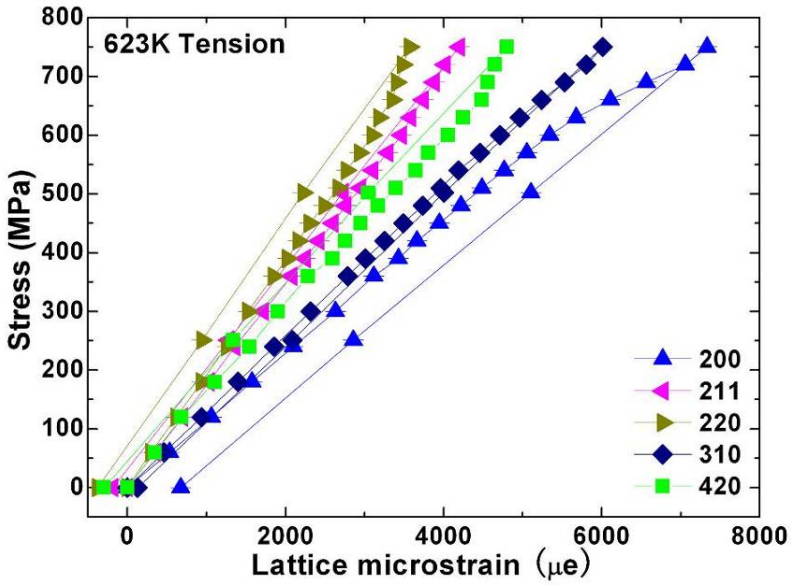

(a)

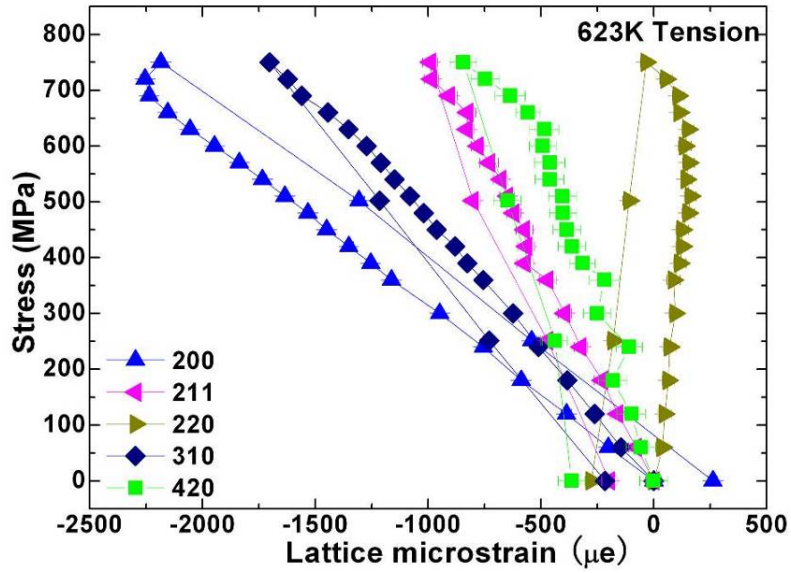

(b)

Figure 32. The response of (hkl) plane-specific lattice strains along axial direction (a), and transverse direction (b), as a function of applied stress during tensile deformation at 623 K.

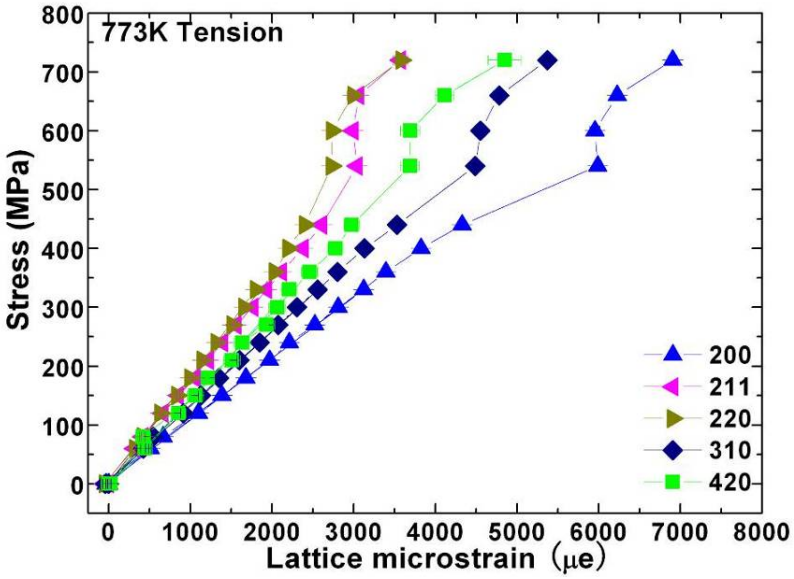

(a)

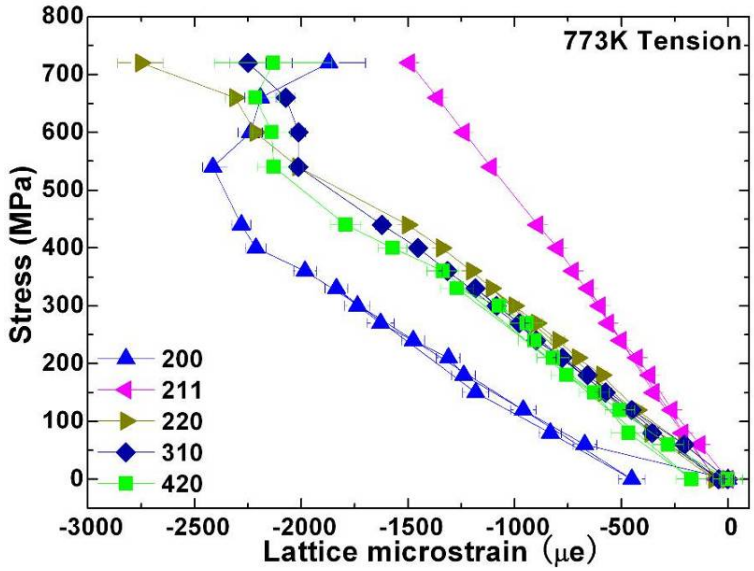

(b)

Figure 33. The response of (hkl) plane-specific lattice strains along axial direction (a), and transverse direction (b), as a function of applied stress during tensile deformation at 773 K.

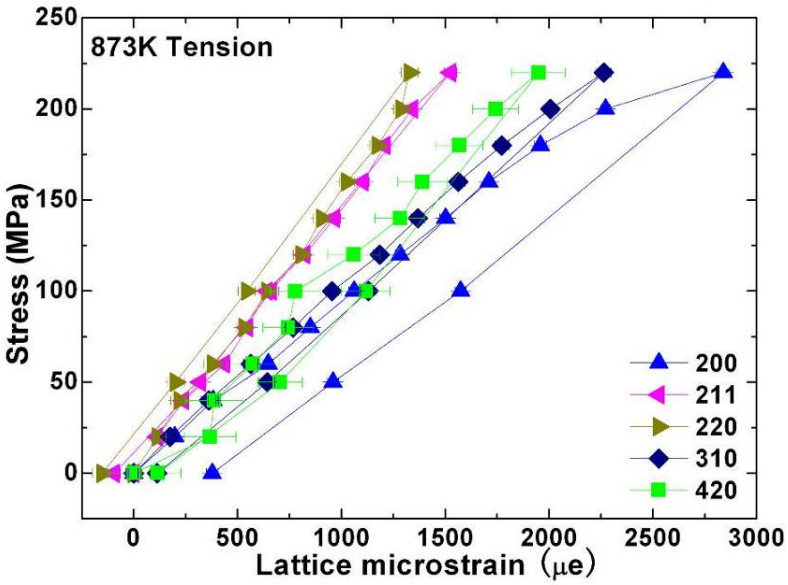

(a)

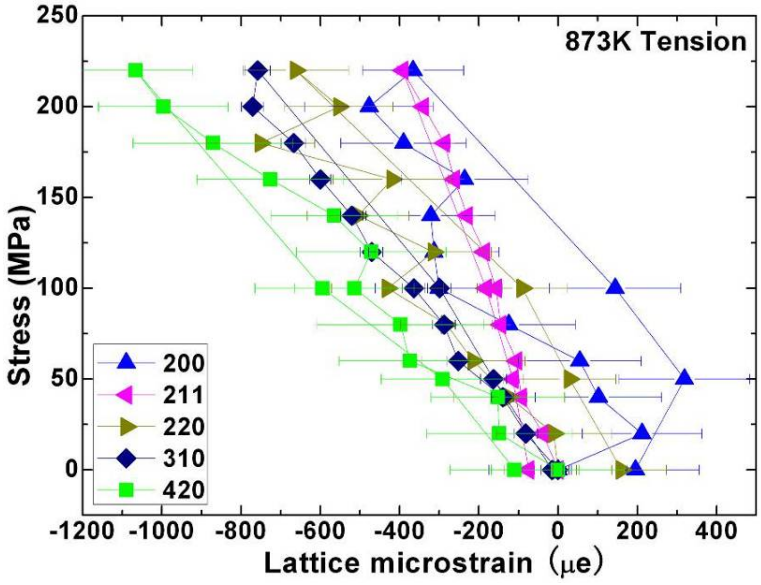

(b)

Figure 34. The response of (hkl) plane-specific lattice strains along axial direction (a), and transverse direction (b), as a function of applied stress during tensile deformation at 873 K.

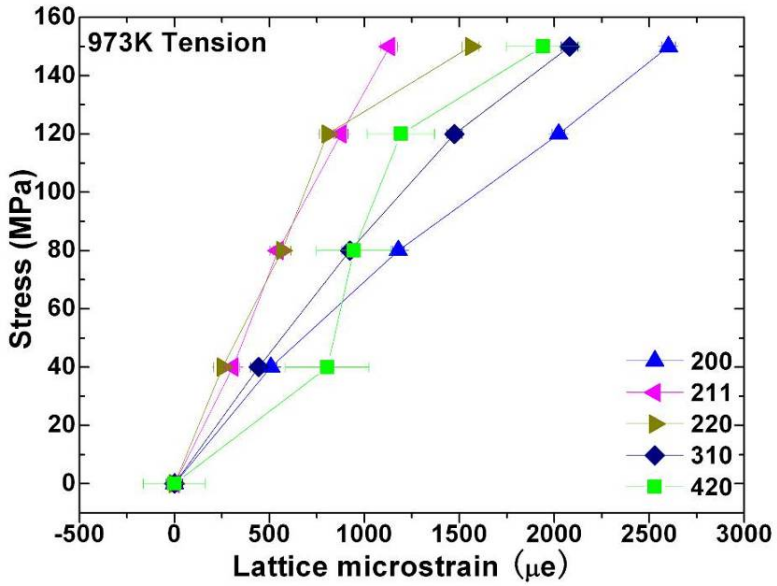

(a)

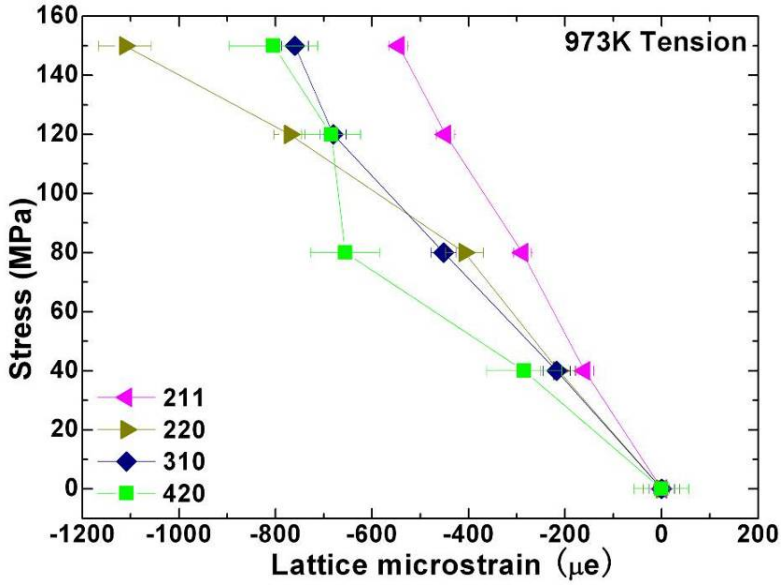

(b)

Figure 35. The response of (hkl) plane-specific lattice strains along axial direction (a), and transverse direction (b), as a function of applied stress during tensile deformation at 973 K.

magnitude of the strength-to-stiffness ratio, σ_{hkl}/E_{hkl} as the ratio of yield stress over Young's modulus for a specific <hkl> orientation [165]. An increased gradient relative to elastic modulus represents plastic yielding of certain (hkl)-oriented grains, while a decreased gradient indicates an intergranular load transfer from the neighboring yielding grains to the measured grains which are still in the elastic regime.

At room temperature below an applied tensile stress of 540 MPa [Figure 31], the lattice strains all display linear response in both axial and transverse directions, thereby verifying elastic deformation within this stress range. The lattice strain evolution at higher stresses could not be confirmed due to loss of data owing to an unfortunate software error at VULCAN.

For deformation at 623 K in axial direction [Figure 32(a)], it is observed that along the axial direction (220) and (211) oriented grain families yield first at around 630 MPa (slightly below the macroscopic yield stress of 650 MPa), with subsequent load transfer to (200) oriented grains. Under a higher stress of 660 MPa, (420) oriented grains start yielding with load transfer to (310) oriented grains. As a result, compressive intergranular stresses along axial direction are accumulated inside the (220), (211), and (420) oriented grains, while tensile stress is accumulated inside the (200) and (310) oriented grains. This trend is further demonstrated by the sign of residual intergranular strain after the specimen was unloaded to 0 MPa. Along the transverse direction [Figure 32(b)], the observed intergranular strain evolution is different from that in the axial direction. It is observed that (310), (220), (211), and (420) oriented grains

accumulate compressive intergranular strain and carry load from neighboring yielding grains at applied stresses of 480, 600, 660, and 690 MPa, respectively. (200) oriented grains exhibit yielding at 700 MPa. Accordingly, tensile residual stress along transverse direction is found in (200) oriented grains while compressive residual stress is found in (310), (220), (211), and (420) oriented grains. It is interesting to note that the gradient representing the ratio of Young's modulus to Poisson's ratio ($-E_{hkl}/\nu_{hkl}$) for a specific <hkl> orientation is positive within the elastic region for (220) oriented grains. Note that the grains which satisfy the axial diffraction condition for a particular (hkl) reflection could have any rotation angle along their plane normal. They can give rise to multiple (hkl) reflections in transverse direction. Only few of these reflections are probed by the detector collecting neutrons diffracted from lattice planes whose plane normals are parallel to the transverse direction. Therefore, it should be emphasized that the grains probed through a certain (hkl) reflection in the transverse direction are different than the grains probed by the same hkl peak along the axial direction.

At 773 K [Figure 33(a)], load transfer from (220) and (420) oriented grains to (310) and (200) oriented grains is also observed along the axial direction within the elastic-plastic regime for applied stresses above 400 MPa (slightly below the macroscopic yield stress of 480 MPa). With further plastic deformation above 540 MPa, most grain families yield and the (hkl) plane-specific lattice strains appear to be saturated. The specimen is eventually fractured at the maximum applied stress, so the unloading steps were not conducted. Along the transverse direction [Figure 33(b)], the lattice strain behavior is different from the

axial direction. (211) oriented grains show a linear response up to the maximal stress. (200) oriented grains yield at 400 MPa and load is transferred to (220) and (420) oriented grains. For applied stresses above 540 MPa, lattice strains are saturated in the (420) and (310) oriented grains, while (220) lattice strain increases and (200) lattice strain decreases dramatically with further increase in tensile load.

At 873 K [Figure 34(a)], the (220) oriented grain starts to yield at 180 MPa along the axial direction. At the same time, the reduced gradients of (310) and (200) lattice strains indicate that load is transferred from the plastically deformed grains to the (310) and (200) oriented grains that are still in the elastic regime. The residual lattice strain upon unloading also verifies this trend of intergranular load transfer. The (211) and (420) lattice strains show a linear response throughout the loading process. However, in transverse direction [Figure 34(b)], any conclusive trends could not be drawn due to scatter in the lattice strain data.

At 973 K [Figure 35(a)], (220) and (310) oriented grains yield around 120 MPa along the axial direction. In transverse direction [Figure 35(b)], load transfer from yielded (420) oriented grains to the elastically deformed (220) oriented grains occur at around 80 MPa.

5.4.3 Intragranular Local Phase Strain

The evolution of intragranular local phase strains along the axial direction as calculated from Eq.(31) is exhibited in Figures 36 ~ 39. It needs to be emphasized that (hkl) plane-specific lattice strains are superimposed on the

intragranular local phase strain. We select (420) and (200) oriented grains to study the intragranular local phase strains due to the relative high intensities of their corresponding (210) and (100) superlattice peaks. Moreover, tensile and compressive intergranular strains are accumulated in (200) and (420) oriented grains, respectively, as described in Section 5.4.2. The behavior of these grains can therefore be taken as the representative of the different effects superimposed on the intragranular local phase strains.

When the (420) oriented grains yield at 623 K under 660 MPa [Figure 32(a)], the matrix inside (420) oriented grains actually yield first and load is subsequently transferred to the precipitates inside the (420) oriented grains, which is evident by the splitting of the (420) local phase strains in Figure 36. Such interphase load transfer is mainly caused by the difference in plastic anisotropies of the matrix and the precipitate phases. The yield stress of the precipitate phase is expected to be much higher than that of the matrix. Due to the high magnitude of antiphase boundary energy (an experimentally-determined lower limit of 500 mJ/m^2 on {110} planes of the NiAl intermetallics [153]), the precipitates do not necessarily yield even though the matrix undergoes plastic deformation. Similar to (420) oriented grains, β and β´ phases inside (200) oriented grains show a consistent reduction in elastic gradient [Figure 36], when intergranular load transfer to the (200) oriented grains occurs above 600 MPa. Afterwards, yielding in the β phase occurs at 700 MPa. The interphase load transfer to the matrix is well captured by the splitting of β and β´ local phase strains and the substantial increase of matrix phase strain is revealed by the 200

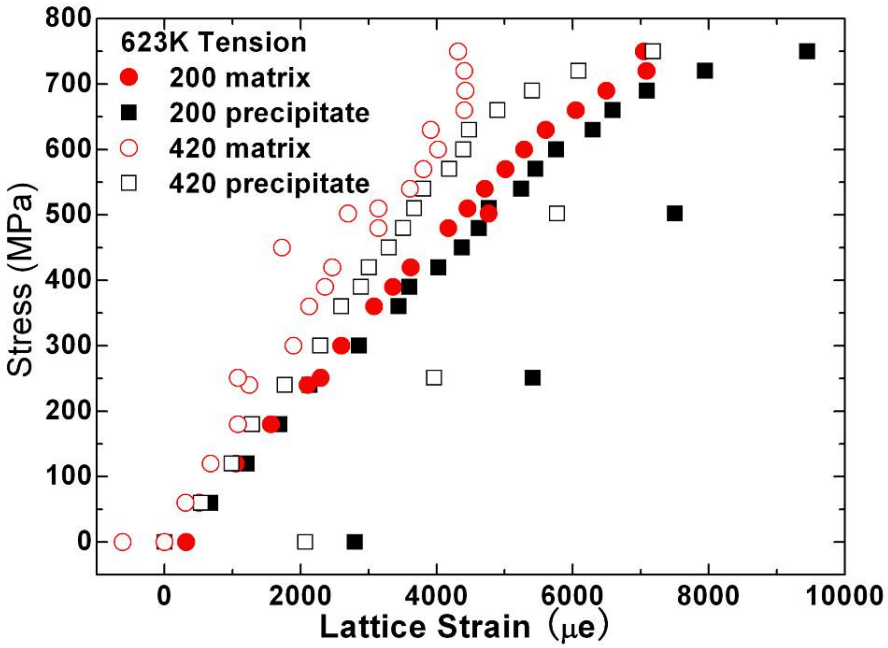

Figure 36. The evolution of (200) and (420) intragranular local phase strains along axial direction during tensile deformation at 623 K.

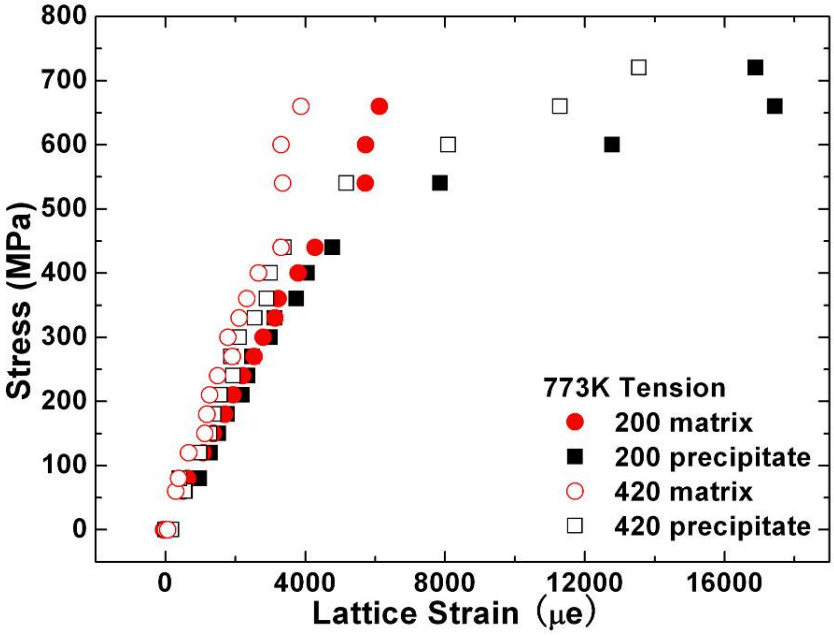

Figure 37. The evolution of (200) and (420) intragranular local phase strains along axial direction during tensile deformation at 773 K.

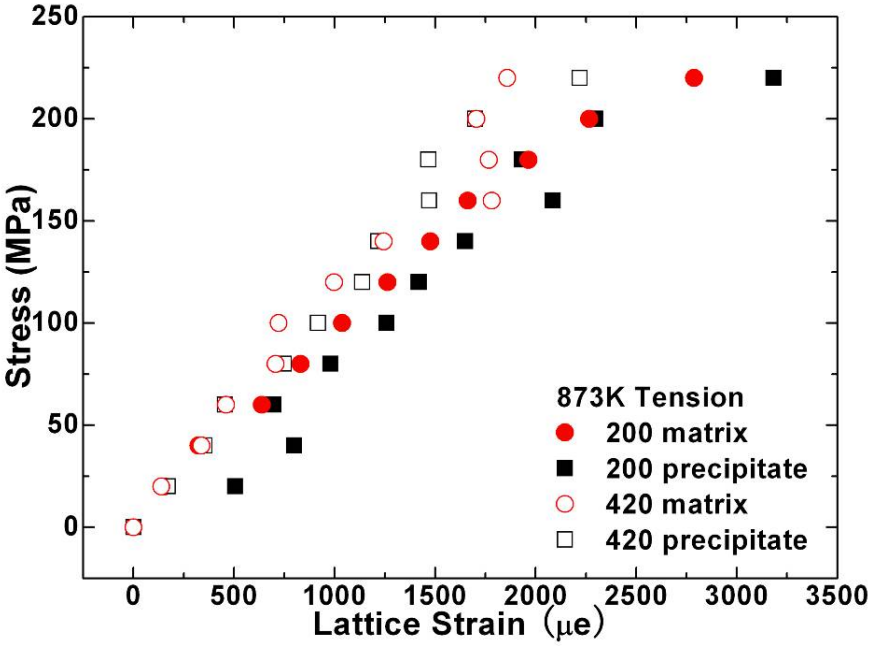

Figure 38. The evolution of (200) and (420) intragranular local phase strains along axial direction during tensile deformation at 873 K.

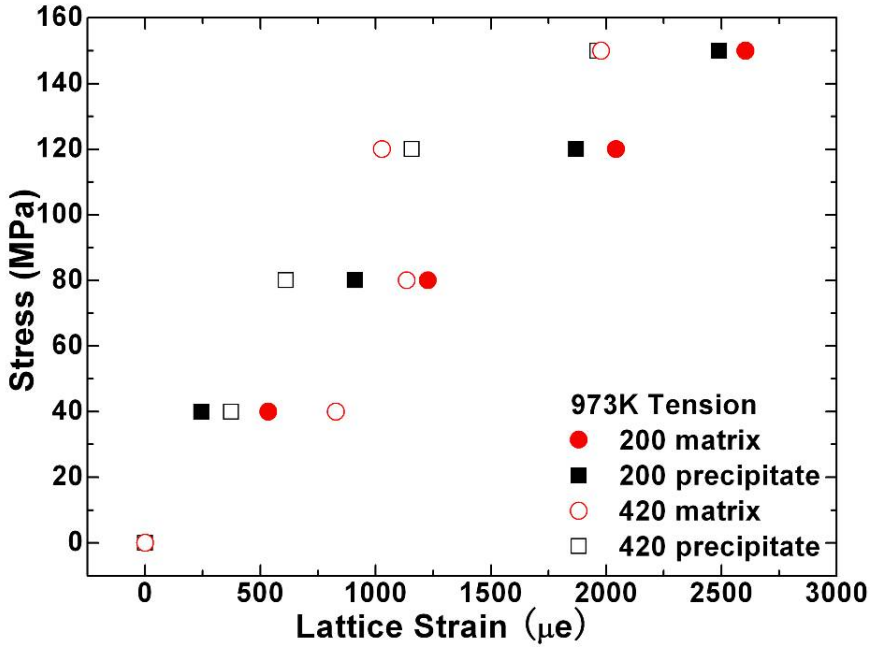

Figure 39. The evolution of (200) and (420) intragranular local phase strains along axial direction during tensile deformation at 973 K.

diffraction peaks. The interphase strain evolution is further demonstrated by the compressive residual lattice strains in the β phase of the (420) oriented grains and the tensile residual strains in the β′ phases of the (200) and (420) oriented grains.

The local phase strain evolutions at 773 K (Figure 37) and 873 K (Figure 38) show similarity to the trend at 623 K. After most grains yield at 540 MPa and 773 K with saturation of lattice strains in the β phase of (200) and (420) oriented grains, there is a dramatic load transfer from the matrix to the precipitate phase. Interphase load transfer inside the (420) oriented grains at 873 K is also evident by the changes in the elastic gradient of the β and β′ phases above 160 MPa. However, interphase lattice strain evolution is not obvious during tension at 973 K.

5.4.4 Lattice Misfit Evolution

The lattice misfit between β and β′ phases inside (200) and (420) oriented grains under zero stress is plotted in Figure 40 as a function of temperature. The lattice misfit at room temperature is ~ -0.085%, which is within the range of the reported values of 0.14% for Fe-Cr-Ni-Al alloy [18], 0.2% for Fe-Ni-Al alloy [24], and -0.7% ~ 0.8% for Fe-Ni-Al-Mo alloy with varying amount of Mo [21]. It is observed that lattice misfits in both (200) and (420) oriented grains increase by less than 0.1% when temperature is raised to 973 K. This trend indicates a slight reduction in the relative difference between the lattice parameters or lattice spacings of the two phases. It is consistent with the slightly higher value of the

thermal-expansion coefficient in β′ phase (15.1 x 10^{-6} K^{-1} for NiAl [153]) as compared to β phase (14.6 x 10^{-6} K^{-1} for pure Fe [166]).

The interphase load transfer within the plastic regime as described in Section 5.4.3 leads to a change in the lattice misfit between β and β′ phases. The evolution of coherency strain (representative of lattice misfit) with respect to the macroscopic strain (determined from crosshead displacement) are displayed in Figures 41 and 42 for tension at 623 and 773 K. There is a substantial increase in the coherency strain of both (200) and (420) oriented grains beyond macroscopic strain of approximately 1.5%. The sign of coherency strain changes from negative at unloaded state to positive at large plastic deformation, indicating an incremented lattice misfit with undergoing plastic strain. However, no clear trend of coherency strain or lattice misfit evolution is observed at 873 and 973 K.

5.4.5 Precipitate Peak Width Evolution

Peak broadening provides qualitative evaluation of microstructural features including the size of the diffracting crystallites and microstrains caused by dislocations. The peak width is characterized by the full width at half maximum (FWHM) of the fitted Gaussian profile. FWHM of the superlattice 100 and 210 peaks are presented in Figures 43 ~ 47 as a function of applied stress at various temperatures. FWHM of the matrix and the precipitate peaks other than 100 and 210 peaks are not reported due to the following reasons: (a) FWHM of the overlapping fundamental reflections, such as a 200 peak, include the peak width

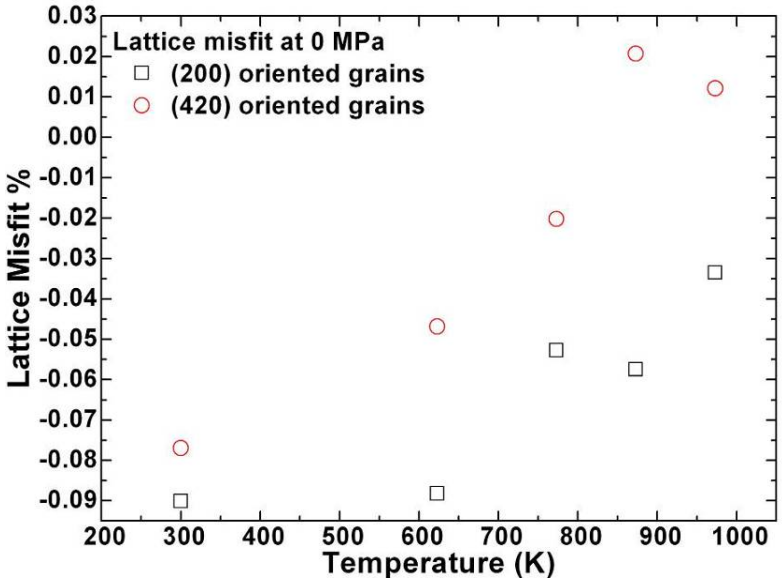

Figure 40. The measured lattice misfit between β and β´ phases in (200) and (420) oriented grains under zero stress as a function of temperature.

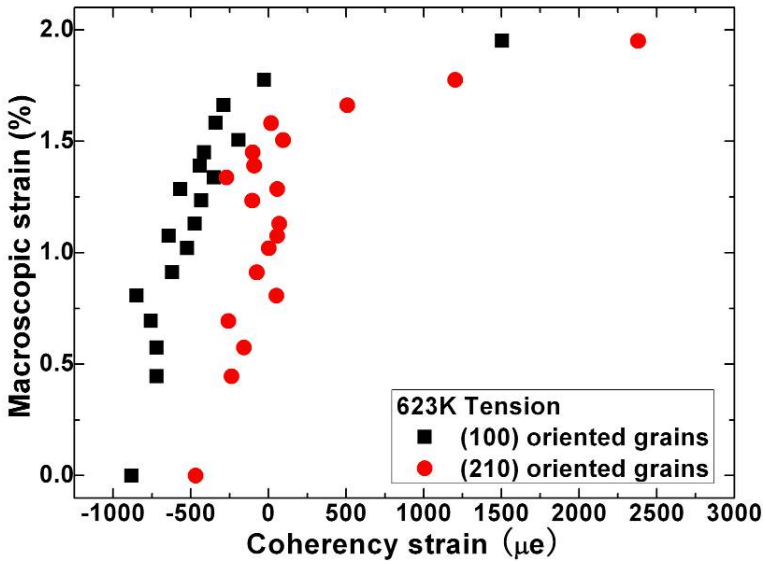

Figure 41. Axial coherency strain in (200) and (420) oriented grains against the macroscopic strain for tension at 623 K.

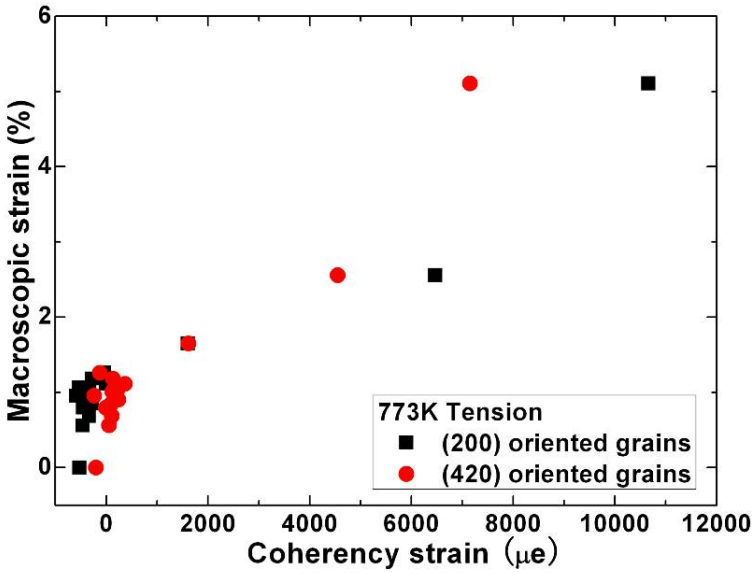

Figure 42. Axial coherency strain in (200) and (420) oriented grains against the macroscopic strain for tension at 773 K.

information of both phases; (b) The average diameter of the precipitates in the aged state is ~ 130 nm, which causes additional peak broadening due to the small size of the precipitates. A good solution to separate the overlapping hkl peaks for accurate determination of both peak positions and widths for the β and β´ phases is yet to be established.

Nevertheless, the characteristic trend for peak width evolution can be revealed despite somewhat scattered data of the fitted FWHM. The FWHM of the precipitate 100 and 210 peaks starts to increase, once load transfer from the matrix to precipitates starts to occur at 623, 773, and 873 K [Figures 44 ~ 46]. It can be further observed that the stress under which peak width starts to increase varies from ~700 MPa at 623 K to ~ 200 MPa at 873 K. Upon unloading, the magnitude of peak width keeps constant [Figure 44]. Since the precipitate phase remains elastic and takes load from the plastic deformed matrix, it is not appropriate to attribute the peak broadening to decrease in particle size or increased dislocation density inside the precipitate phase. Rather, the peak width evolution is possibly associated with dislocations climbing over the β´ particles, which causes the local misorientation in the precipitates. Such misorientation due to the inhomogeneous dislocation-strain field will cause peak broadening in the precipitate phase. Therefore, we conclude that the FWHM is an additional important parameter which reflect the extent of plastic deformation in the matrix and is consistent with the accumulation of interphase lattice strains at temperatures below 873 K.

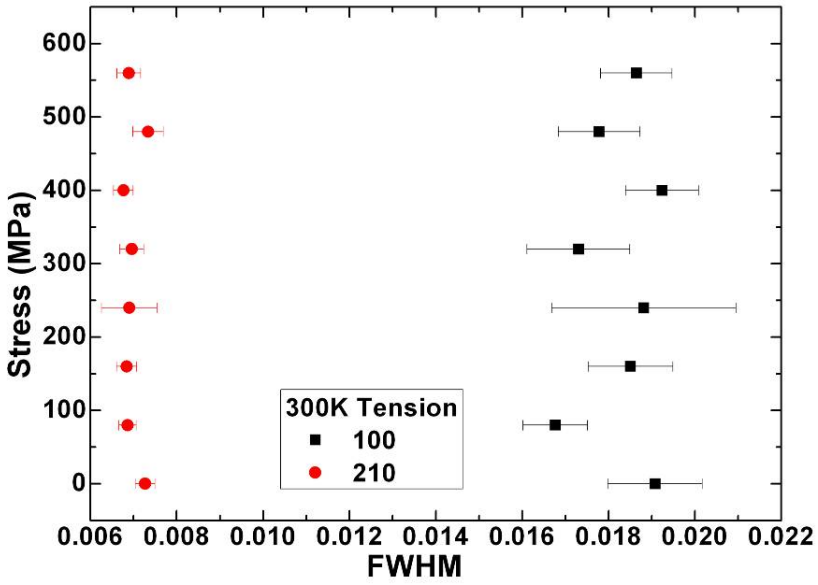

Figure 43. Peak width evolution for 100 and 200 superlattice peaks along axial direction during tensile deformation at 300 K.

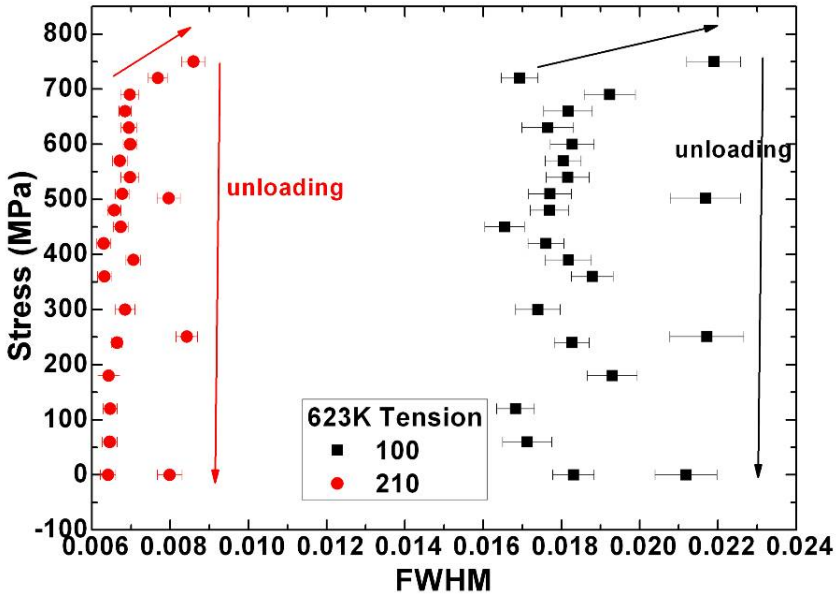

Figure 44. Peak width evolution for 100 and 200 superlattice peaks along axial direction during tensile deformation at 623 K. The last four data points represent peak width during unloading.

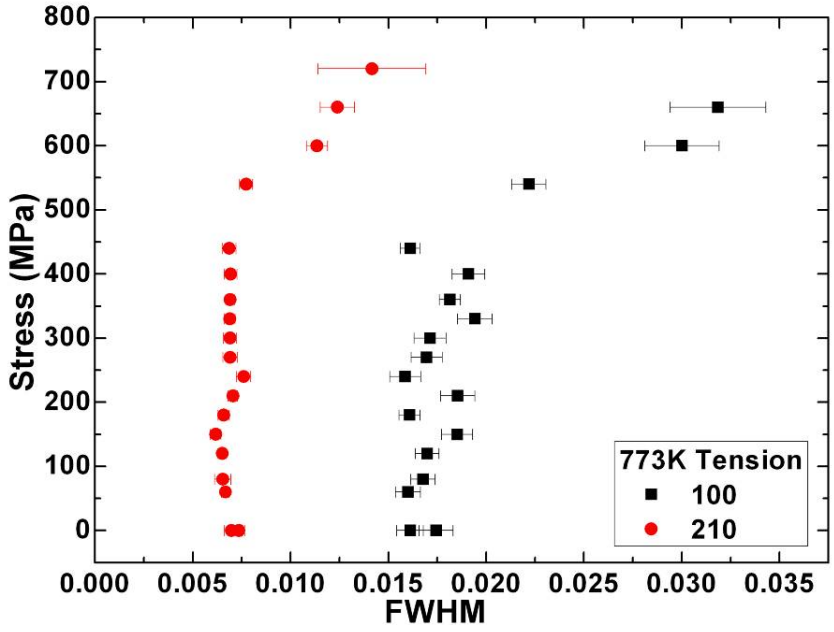

Figure 45. Peak width evolution for 100 and 200 superlattice peaks along axial direction during tensile deformation at 773 K.

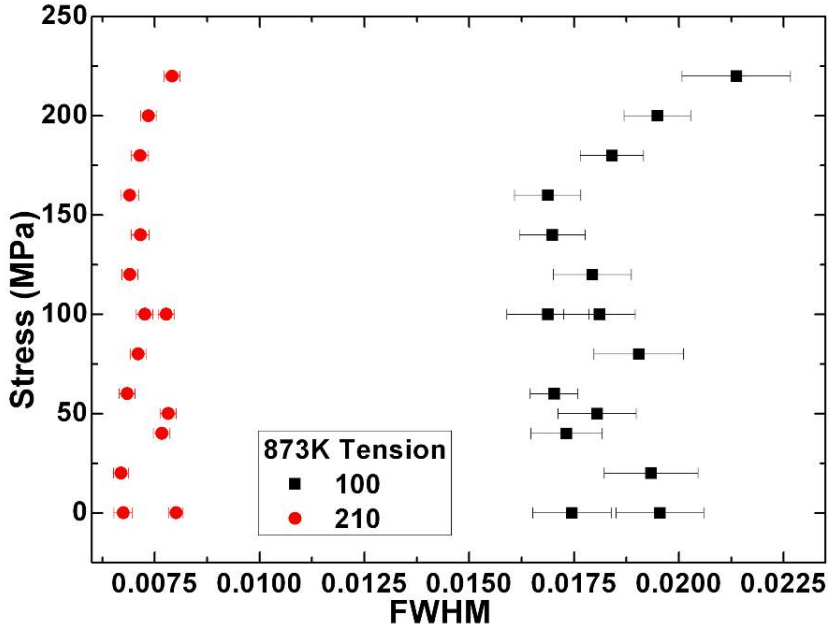

Figure 46. Peak width evolution for 100 and 200 superlattice peaks along axial direction during tensile deformation at 873 K.

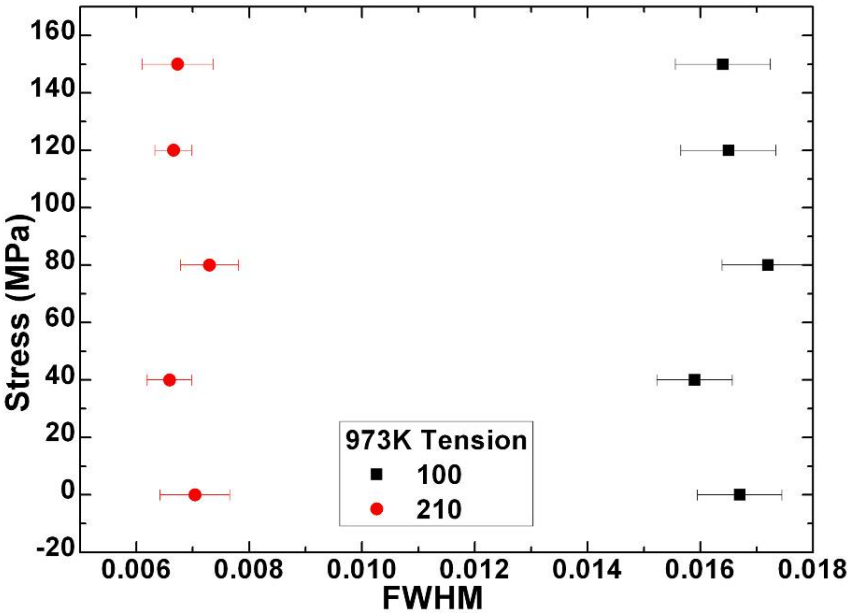

Figure 47. Peak width evolution for 100 and 200 superlattice peaks along axial direction during tensile deformation at 973 K.

It is also interesting that the increase in peak width of the precipitate 100 and 210 peaks is a function of temperature. The increase in peak width is maximum at 623 K, whereas the increase in peak width of the precipitate phase at 973 K is almost negligible as shown in Figure 47.

5.5 Results: In-Situ Creep

5.5.1 Macroscopic Creep Behavior

Macroscopic tensile-creep curves at 973 K under 107 and 150 MPa are shown in Figure 48. It is evident from the strain rate vs. time plot [Figure 48(c)] that at 107 MPa, primary creep is transient (~ 70 minutes), followed by a short period of secondary creep for the next ~ 130 minutes and an extended period of tertiary creep afterwards. At 150 MPa, the strain rate increases progressively starting from a minimum value of 2.2 x 10^{-5}/s until rupture. Earlier studies on similar alloy systems [35,167] have reported that a well-defined steady-state creep regime is barely observed, and an extended tertiary creep follows during tensile creep. Therefore, creep data are interpreted in terms of the minimal creep rate in the present work. Minimal creep rates measured during the in-situ experiment are 1.8 x 10^{-7}/s and 2.2 x 10^{-5}/s at 107 and 150 MPa, respectively. These values are roughly one order of magnitude lower than the reported compressive creep rates in a similar composition with a 24-volume percent (vol.%) of precipitates [34].

Figure 49(a) shows the stress dependence of the minimal creep rate for the data measured at SMARTS, together with the tensile-creep rate measured by

dead-load creep frames at The University of Tennessee's laboratory. The fitted slope of the minimal creep rate vs. true stress on the logarithm scale characterizes the stress dependence of the minimal creep rates, and is referred to as the apparent stress exponent. The value of 7.58 for the apparent stress exponent is slightly lower than reported values of around 10 by other investigators [34,167]. The data point at 107 MPa lies slightly lower than the linear fit, and the difference is within a factor of 2. The minimal creep rate at 150 MPa is appreciably higher than the predicted value by the linear fit. A high magnitude of the apparent stress exponent at low stresses is commonly observed in alloys with second-phase particles, accompanied by a reduced stress exponent at high stresses. In such a case, the creep rate can be analyzed using the concept of a threshold stress (or a back stress), whereby a uniform stress exponent and activation energy could be used to elucidate the underlying creep mechanisms throughout the whole stress region. The threshold stress, or the minimal applied stress below which no measurable creep is observed, is indicative of the different particle-dislocation interaction modes. The power-law creep, considering the threshold-stress compensation, can be described by Equation (25). The threshold stress can be determined by the intercept of $\dot{\varepsilon}^{1/n}$ vs. true stress at zero stress, as presented in Figure 49(b). A stress exponent of 3 ~ 5 is generally selected to obtain the threshold stress. Here, a good fit is achieved with n = 4, and the magnitude of the threshold stress is 46.1 MPa. Previous studies [34-35] also suggest a fourth-power stress dependence of the steady-state creep rate for compressive and tensile creep in the stress range of 50 ~ 170

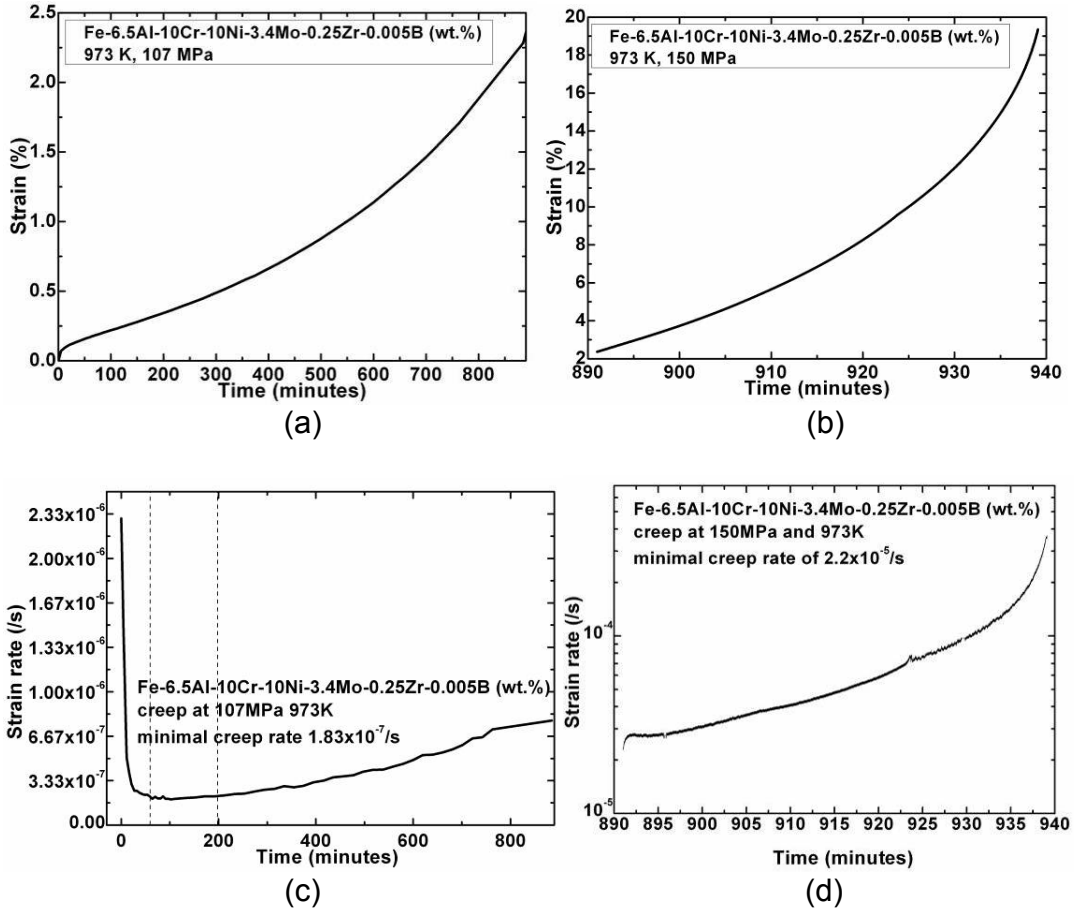

Figure 48. Macroscopic-creep curves of strain vs. time at (a) 107 MPa and (b) 150 MPa measured at SMARTS. Strain rate vs. time are plotted in (c) and (d), respectively. Two dashed lines characterize primary, secondary, and tertiary creep regimes.

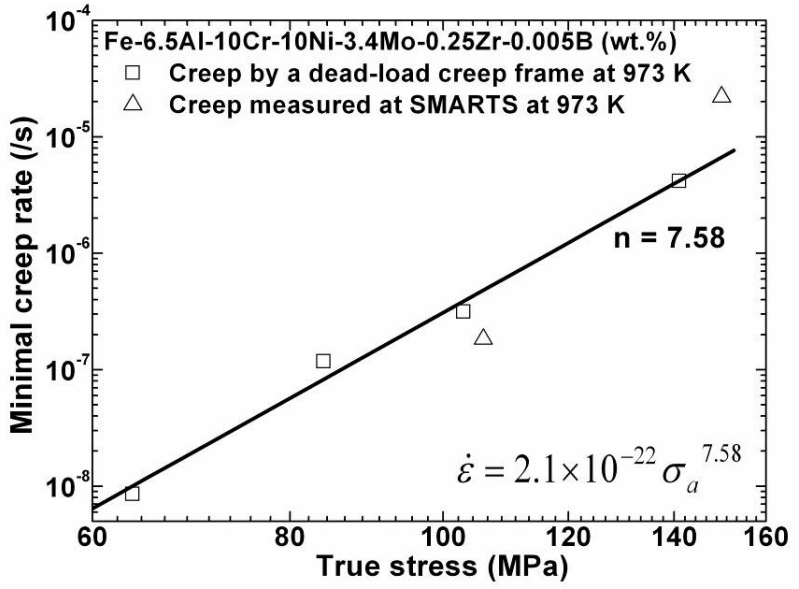

(a)

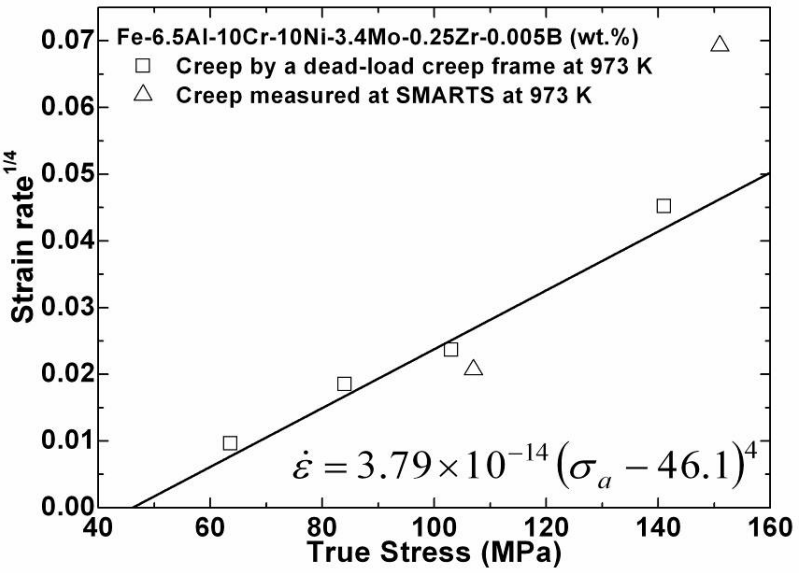

(b)

Figure 49. (a) Minimal creep rate vs. true stress at 973 K on a logarithm scale, and (b) minimal creep rate$^{1/4}$ vs. true stress at 973 K on a linear scale.

MPa and temperature range of 923 ~ 1023 K for alloys with β' volume fractions up to 37%. The observed threshold stress (46.1 MPa) is slightly lower than the reported values of 49 ~ 57 MPa at the same temperature by compressive creep [34]. It is worthwhile to note that although all the data points for creep rates lie close to the fitted line in Figure 49(b) for n = 4, the creep rate at 150 MPa is substantially higher. This trend indicates that the creep process is possibly governed due to a different mechanism at higher stress levels, which will be discussed in Section 5.6.2.

5.5.2 Temporal Evolution of Average Phase Strains

At 973 K and under a tensile stress of 18 MPa (the reference state), the lattice parameters of β and β´ phases are 2.9034 Å and 2.9040 Å, respectively. The lattice misfit is 0.0002, as calculated by Eq. (35). The precipitate volume fraction predicted by the Rietveld refinement is ~ 15%, which is in agreement with 18% determined by previous analytical electron microscopy (AEM) and atom-probe tomography (APT) analyses [27]. The precipitate volume fraction doesn't change throughout the creep regime.

The bulk Young's modulus of the material at 973 K is 130.5 ± 0.2 GPa, determined from the macroscopic stress-strain curve during tensile loading from 18 to 107 MPa. Macroscopic plastic yielding didn't occur during loading period. The measured bulk Young's modulus (130.5 GPa) is slightly lower than the reported value for a low-carbon steel (145 GPa [168]) and for a NiAl intermetallics (160 GPa [153]) at 973 K. The measured value of Young's modulus

is further verified, using the model described in Section 4.4.2 which incorporates the composition and temperature dependence of the shear modulus, μ, in bcc Fe-based alloys. The data of the Fe-based matrix composition are taken from the previous published results [26]. The Young's modulus for the matrix is then calculated using $E = 2(1+\nu)\mu$ to be 126 GPa, for a Poisson's ratio ν of 0.37. The measured Young's modulus of 130.5 GPa for the material shows a 3% increase relative to the calculated value of 126 GPa for the unreinforced material.

The temporal evolution of the axial and the transverse average phase strains for β and β′ phases calculated by Eq. (29) are presented in Figure 50(a). At 107 MPa, the axial phase strains keep approximately constant at 500 ~ 600 με during primary, secondary, and tertiary creep regimes. Similar phase-strain evolution during creep has been reported in the metal-matrix composites [169]. Simultaneously, in the transverse direction, the compressive phase strains of ~ 400 με develop for the β and β′ phases during the primary creep and remain constant afterwards. Since the average phase strains keep unchanged in the secondary-creep regime, it can be inferred that the load partitioning between β and β′ phases doesn't vary throughout the secondary creep. The magnitude of the axial β phase strain is ~ 100 με higher than that of the β′ phase. In the transverse direction, both strains have roughly the same magnitude, which can be attributed to Poisson's constraints on the two phases.

Once the applied tensile stress is raised to 150 MPa, the difference between the β and β′ axial phase strains jumps to ~ 250 με, as presented in

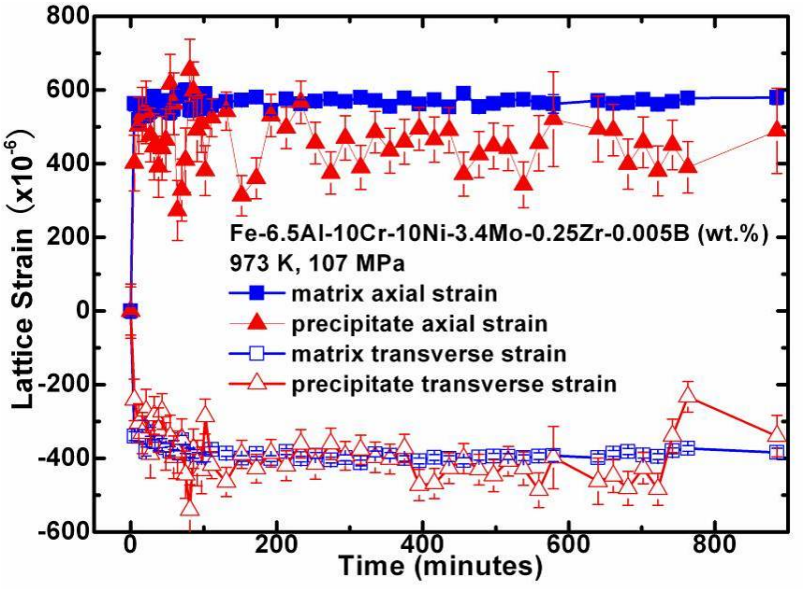

(a)

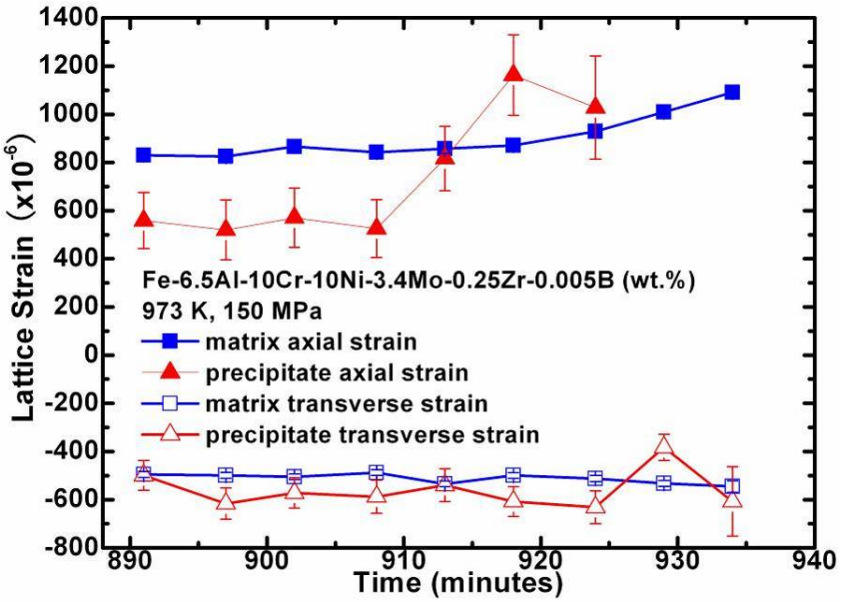

(b)

Figure 50. (a) Temporal evolution of axial and transverse average phase strains for β and β′ phases at (a) 107 and (b) 150 MPa. Error bars from the GSAS Rietveld refinement are plotted.

Figure 50(b). Note that true stress increases due to the accumulated macroscopic strain and reduction of the sample cross section, although the applied stress keeps constant at 150 MPa. In the initial 15 minutes of creep, the average phase strains in the axial and transverse directions remain approximately the same. However, a sharp increase of the axial β′ strain by a factor of 2 (from ~ 550 to ~ 1100 με) is observed after 25 minutes of creep (at a macroscopic strain of 7%). Subsequently, the average phase strain in the matrix shows a steady increase from 850 to 1100 με until the final rupture. The reduced intensity of 100 superlattice peaks made it impossible to determine the β′ average phase strain with sufficient accuracy in the axial direction after 930 minutes of creep. The large increase in the β′ strain at 150 MPa cannot be entirely attributed to the increase in the true stress, which could only account for a lattice strain change of less than 100 με in the β′ phase. Instead, this implies the generation of interphase stresses and consequently a change in the load partition between the matrix and the precipitates, which will be discussed in the following paragraphs.

The constrained lattice misfit between β and β′ phases along the axial and transverse directions are plotted in Figure 51, as a function of the macroscopic creep strain at 973 K and for the two stress levels. In the transverse direction, the misfit keeps almost unchanged throughout the two stress regimes, with an average value of -0.00054. In the axial direction, the misfit remains constant below 5% macroscopic strain with an average magnitude of 0.00008, followed by a gradual increase beyond a macroscopic strain of 5% and ultimately a rapid

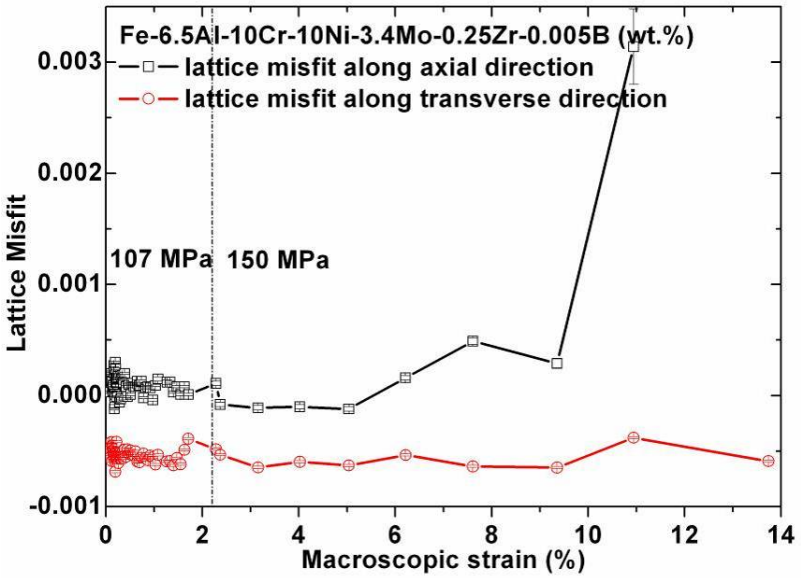

Figure 51. (a) Lattice misfit along axial and transverse directions as a function of macroscopic strain.

increase prior to the sample fracture under an applied stress of 150 MPa. The lattice mismatch increases to 0.00049 and 0.00314 along the axial direction corresponding to the macroscopic strains of 7.6% and 10.9%, respectively. The evolution of the lattice misfit confirms the accumulation of the internal stress between the two phases during creep at 150 MPa.

It is worth noting that the magnitude of the lattice misfit prior to a macroscopic strain of 5% is extremely low, suggesting negligible constraint between the two phases. For comparison, the unloaded lattice parameters of β and β´ phases are 2.8764 Å and 2.8763 Å at room temperature, which amounts to a misfit of only -0.00004. The difference in lattice misfit at room temperature and 973 K in the unloaded state can be attributed to the difference in thermal-expansion coefficients of β´ and β, consistent with the reported values are 14.6 x 10^{-6} and 15.1 x 10^{-6} K^{-1} for the pure Fe [166] and NiAl intermetallics [153], respectively. The measured lattice misfits at room temperature and 973 K are within the range of the reported values (-0.0006 ~ 0.008) at room temperature in the Fe-Ni-Al alloys [18,20-21].

To better understand the drastic increase of the β´ average phase strain above 150 MPa along with a concurrent increase in the lattice misfit, the average phase strains as a function of the true stress are also plotted in Figure 52 to clearly show this trend. The observed trend indicates that there is a load transfer from the plastically deformed matrix to the elastically-deformed precipitate. In Figure 52, shortly after the jump of the β´ phase strain, there is an obvious decrease of the instantaneous gradient for the true stress vs. phase strain curve

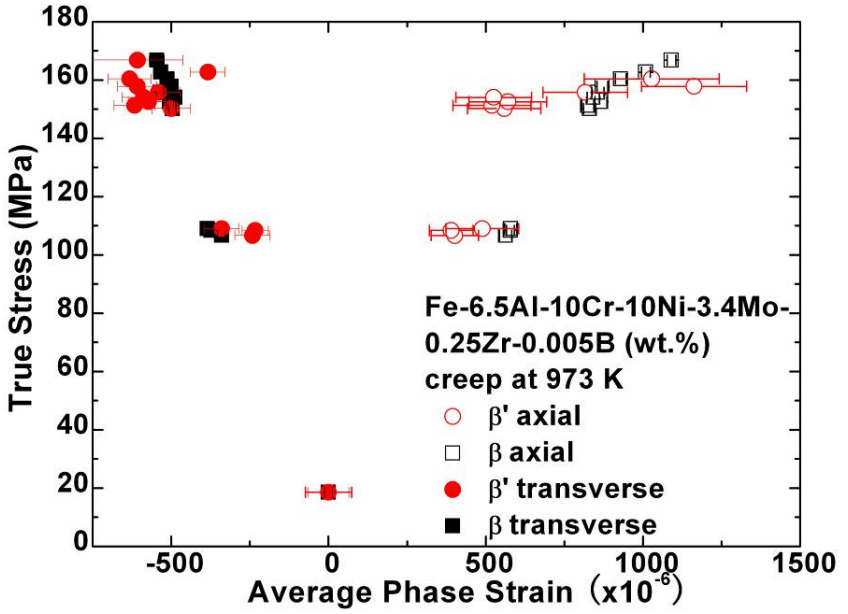

Figure 52. Average phase strain as a function of true stress along axial and transverse directions at 973 K. Selected data points for the phase strains are shown at 107 MPa.

in the matrix along the axial direction, implying hardening of the matrix during further plastic deformation. However, as compared to the matrix, the precipitate-phase strain shows a shallower slope with respect to the true stress, which verifies that more load is partitioned to the precipitate phase. It can be inferred that due to the interphase load partitioning, the precipitates are under a tensile stress, while the matrix is under a compressive stress.

The degree of load sharing between the matrix and precipitates at high temperatures is characterized by the misfit between the two phases, which depends on the combined influence of the elastic moduli and the plastic misfit of the two phases, as well as stress relaxation during creep. Stress relaxation refers to local inelastic processes (e.g., the plastic relaxation, diffusional relaxation, and particle breakage or debonding) that reduce the load transfer caused by elastic and plastic misfits. Since the two phases have similar elastic moduli, major contributions to the load transfer should come from the plastic misfit and stress relaxations, although it is not possible to identify in detail the different mechanisms involved from the ND data alone. Plastic misfit is associated with the difference of the critical resolved shear stresses in the two phases, which governs the sequence and the required applied stress for yielding. The high anti-phase boundary energy of the precipitates, e.g., an experimentally-determined lower limit of 500 mJ/m^2 on (110) planes of NiAl intermetallics [153], prevents dislocations from penetrating into the precipitates. Consequently, it can be inferred that the plastic deformation through dislocation slip occurs mainly in the matrix, while the precipitates largely remain elastic. However, even though the

precipitates remain elastic, dislocations can bypass particles by diffusion-assisted climbing, which would lead to the local misorientation in the precipitates. Such misorientation of the precipitates due to an inhomogeneous dislocation-strain field will cause peak broadening for the diffraction peaks corresponding to the β′ phase. It is indeed observed that in the late stage of creep deformation at 150 MPa, the peak intensity of the 100 superlattice peak decreases and its peak width increases.

It was reported for metal-matrix composites that stress-relaxation mechanisms can cause less efficient load transfer from the matrix to the reinforcement at elevated temperatures [169-170]. However, the stress-relaxation mechanism is not likely to dominate the load transfer at 150 MPa and 973 K, considering the observed load partition between the two phases.

5.5.3 Temporal Evolution of (hkl) Plane-Specific Lattice Strains

In a polycrystalline material, the response of the differently-oriented grains under an applied stress varies due to the effects of the elastic and plastic anisotropies. The elastic anisotropy arises from the fact that the elastic modulus depends on the grain orientation, which is manifested by the difference in the slopes of the applied stress vs. (hkl) lattice strain in the elastic region. The origin of the plastic anisotropy is that plastic deformation occurs on certain preferential slip systems, and the sequence of grain yielding relies on the magnitude of the Schmid factor determined by grain orientation. The plastic anisotropy is usually characterized by the non-linear behavior of (hkl) plane-specific lattice strain and

the tensile/compressive strain shift, relative to its elastic slope. The examination of elastic and plastic anisotropies is important to understand the interactions between grains of different orientations during creep deformation, because they provide a measurement of the internal stress state, even in the plastic region.

The temporal evolution of the (hkl) plane-specific lattice strains for differently-oriented grains along the axial and transverse directions are plotted in Figs. 53(a) - (d). At 107 MPa, the gradual increase of 200 and 310 plane-specific lattice strains occur in the primary creep regime, while all the (hkl) lattice strains remain constant during secondary and tertiary creep. The transition to constant (hkl) lattice strains corresponds well with the onset of the secondary creep (~ 70 minutes) [see Figs. 49(a) and (c)]. Similar trends in the (hkl) lattice strains during the primary regime of constant-load creep have been reported in titanium alloys [171] and γ/γ′ Ni-based superalloys [156]. Choo et al. [171] suggested that the creep-induced strain has the same trend as the evolution of (hkl) plane-specific lattice strains during tension. Similarly, our observation is in agreement with the development of (hkl) plane-specific lattice strains in the ferritic steels during room-temperature (RT) tension in the elastic-plastic region characterized by the grain-to-grain yielding phenomenon [172-174]. Specifically, it was reported that the (110) oriented grains yields first, since this is the preferred orientation for slip. Subsequently, a load transfer to (200) oriented grains occurs, leading to an increase in (200) lattice strains [172,174]. Thus, our observation can be interpreted as such: (200) and (310) oriented grains deform elastically and pick up the load from neighboring creeping grains during the primary creep. Further

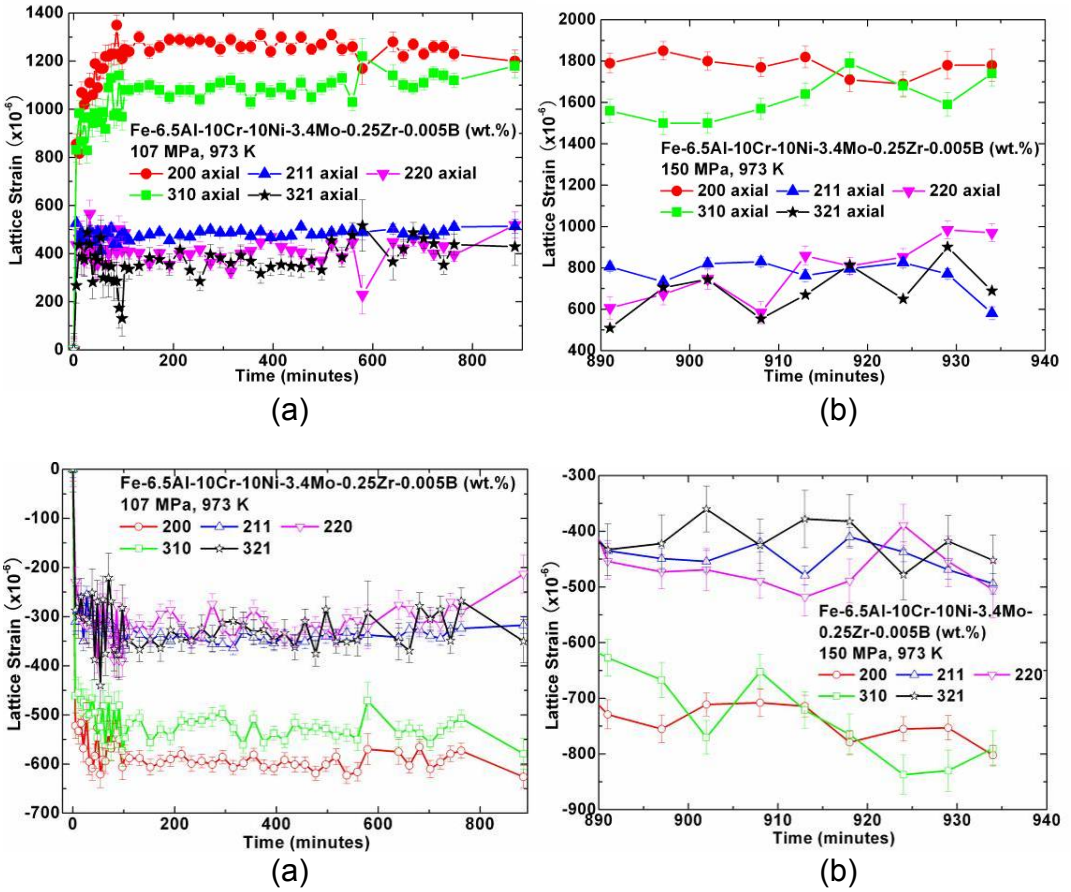

Figure 53. (a) Temporal evolution of (hkl) plane-specific strains in the axial direction for β and β′ phases at (a) 107 and (b) 150 MPa, and in the transverse direction at (c) 107 and (d) 150 MPa. Error bars from the GSAS single-peak fitting are plotted.

discussion on the grain-level load partitioning during creep deformation is presented in Section 5.6. As the stress level is increased to 150 MPa, (110)-oriented grains continue to accumulate lattice strains, while the other plane-specific lattice strains appear saturated.

It has been suggested by different authors that the (211) [175], (110) [175], and (310) [176] planes of bcc steels (textured or non-textured) can be used for macroscopic strain predictions, since these lattice strains show a linear response to the applied stress with little influence of residual intergranular strains in both elastic and plastic regions. This is consistent with our observation that for low stresses and macroscopic plastic strains < 2%, (211)-oriented grains mimic the elastic-lattice response of the average phase train in the matrix obtained by Rietveld fitting. However, at a high stress level of 150 MPa and macroscopic strain larger than 2%, (211) and (110) lattice stains deviate from the elastic response of the matrix as predicted from Rietveld refinement.

5.5.4 Axial Texture Evolution

During tensile deformation, grain reorientation occurs to maintain the geometric compatibility between the neighboring grains, which undergo different degrees of deformation owing to their plastic anisotropy. The grain rotation (or reorientation) induced by creep deformation is manifested by texture evolution. Temporal evolution of the normalized integrated intensities for different (hkl) diffraction peaks along the axial direction is plotted in Figure 54, which indicates texture evolution during creep deformation. For a specific (hkl) diffraction peak,

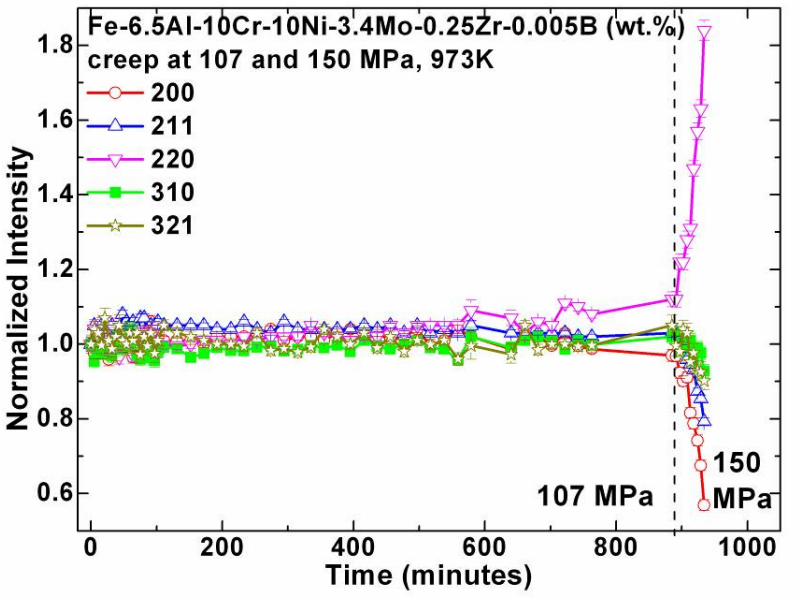

(a)

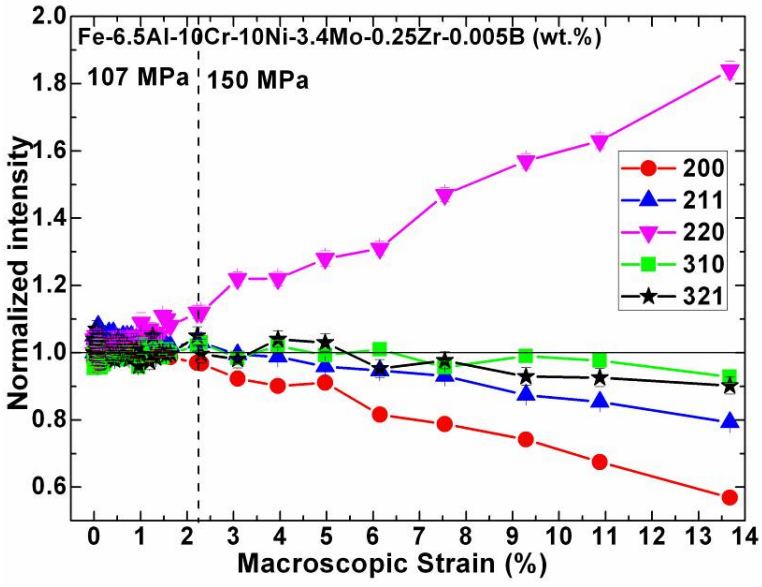

(b)

Figure 54. Intensity evolution of the hkl peaks as a function of (a) creep time and (b) plastic strain. The integrated intensity is normalized with respect to the initial integrated peak intensity at 18 MPa.

the integrated intensity at a certain stress is normalized with respect to the initial integrated intensity value at 18 MPa. It is observed that a preferred orientation for (220) planes gradually develops, as a function of the creep time at 107 MPa, and the intensity enhances by a factor of 1.1 after 880 minutes of creep. In contrast, at 150 MPa within the 45 minutes of creep, the (220)-peak intensity increases sharply by a factor of 1.6, while (200) and (211) peak intensities decrease by about 20 ~ 30%. In addition, a slight decline in (310) and (321) peak intensities is also observed. The development of a preferred orientation for (220) planes is consistent with the fact that bcc materials form a <110> fiber texture under the uniaxial tension deformation [177-178]. Intensities are observed to vary linearly with plastic strains, as exhibited in Figure 54(b).

5.6 Discussions

5.6.1 Temperature Dependence of Single Crystal Stiffness

The intrinsic elastic behavior of a material changes with increasing temperatures due to increased thermal vibrations of atoms around their mean crystallographic positions. It is therefore necessary to determine the variation of single crystal stiffness at different temperatures, as the input for CPFEM computation. Single crystal stiffness C_{11}, C_{12}, and C_{44} in the polycrystalline material have been determined through the least square methods described in Section 5.3. The calculation is based on fitting the experimentally measured diffraction elastic constants from the displacement in the principal hkl diffraction peaks. Therefore, the calculated stiffness generally represents the single crystal

elastic constants of the matrix phase. The stiffness of the precipitate phase is also calculated from the superlattice hkl peaks at 773 K, while data for other temperatures are not available due to the insufficient number of detected superlattice peaks. The results for single crystal stiffness as a function of temperature are exhibited in Figure 55. Figure 56 provides a comparison between the experimentally determined orientation dependent elastic constants and those estimated from the calculated stiffness values along the axial and transverse directions. The stiffness for matrix and precipitates at 623 K is not reported, owing to the lack of a good fitness. As shown in Figure 55 the precipitate phase shows similar values of stiffness as compared to the matrix phase, which is consistent with the observed similarity in the (hkl) orientation-dependent Young's modulus of the two phases.

The temperature effect on the matrix stiffness qualitatively agrees with the reported trend for pure α-Fe [179]. The stiffness display a parabolic decline as temperature goes up, and the softening trend becomes remarkable at temperatures above 773 K. Specifically, C_{11} at 973 K is approximately 50% of its room-temperature value. The corresponding reductions in C_{12} and C_{44} at 973 K are 50% and 40%, with respect to their values at 300 K. As expected, we observe a nonlinear relationship between stiffness and temperature, often described as the anomalous behavior of elastic constants in iron caused by magnetization [180]. The magnetic contribution (change of spin order) to the temperature dependence of elastic constants has been elaborated in past studies [179-181]. It has been reported that the normal temperature dependence

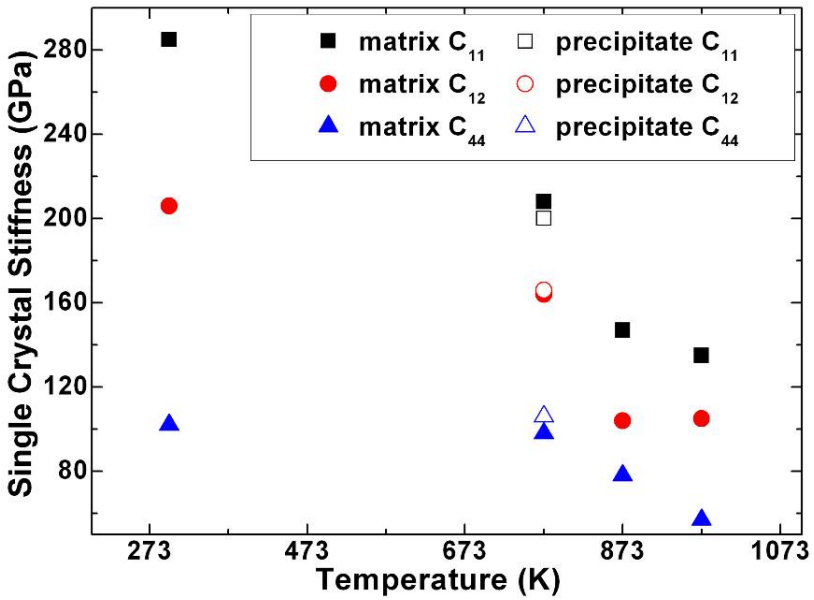

Figure 55. Single crystal stiffness in the matrix and precipitate phases as a function of temperature.

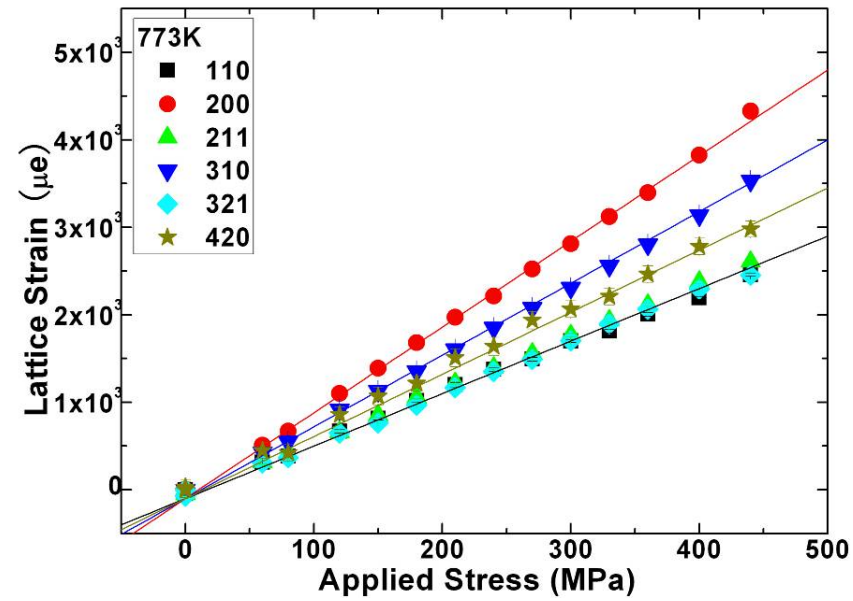

(a)

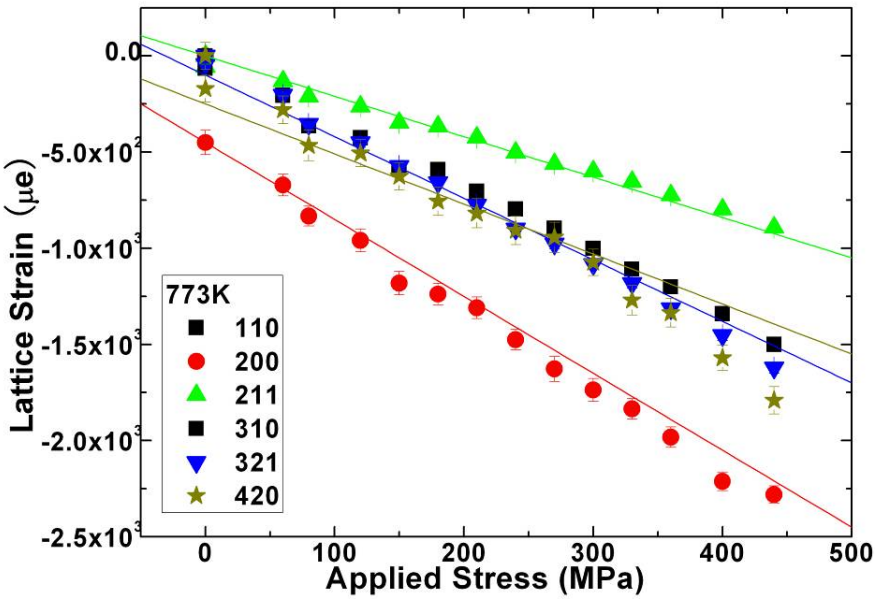

(b)

Figure 56. Calculated elastic linear response of (hkl) plane-specific lattice strains from the least-square fitted stiffness C_{11}, C_{12}, and C_{44}, which is in agreement with the experimental results in (a) axial and (b) transverse directions at 773 K.

is linear above Debye temperature (~ 470 K for pure Fe), while deviation from linearity at high temperatures suggests the effect of magnetism on the elastic constants.

The determined single crystal stiffness values are utilized as the input for CPFEM modeling and are further refined in the simulation, which will be described in Section 5.6.5.

5.6.2 Intergranular Load Transfer During Creep

As reported earlier in Section 5.5.3, the (hkl) plane-specific strains for (200) and (310)-oriented grains display a progressive increase with time along the axial direction during the primary creep at 107 MPa. In order to achieve a better understanding of the lattice-strain behavior at the grain level during creep deformation, a one-dimensional iso-strain model of two grains with different material parameters is performed to qualitatively identify the lattice strain evolution at the grain level during the loading and subsequent constant-stress regimes. A schematic of the model is shown in Figure 57. Effects of the loading rate, relative strength of grains, and stress holding time are qualitatively studied through this model. The assumptions made in the model include:

(1) Two grains are deformed under an iso-strain state, $\varepsilon_1 = \varepsilon_2 = \varepsilon$, or $\dot{\varepsilon}_1 = \dot{\varepsilon}_2 = \dot{\varepsilon}$,

(2) Two grains have the same Young's modulus of $E_1 = E_2 = E$,

(3) Two grains have the same cross-sectional area, so that the average stress on the grains equals the applied stress, $\sigma = (\sigma_1+\sigma_2)/2$, or $\dot{\sigma} = \frac{\dot{\sigma}_1 + \dot{\sigma}_2}{2}$,

(4) Grain 1 has a higher reference strength than Grain 2, that is, $Y_1 > Y_2$.

A power-law creep is employed to describe the rate-dependent plastic strain. Hooke's law is used to calculate the elastic strain. The total strain rate of one grain due to combined elastic and plastic strains can thus be given by

$$\dot{\varepsilon} = \dot{\varepsilon}^e + \dot{\varepsilon}^p = \frac{\dot{\sigma}}{E} + \dot{\varepsilon}_0 \left(\frac{\sigma}{Y} \right)^n \tag{41}$$

where $\dot{\varepsilon}_0$ is the reference strain rate, which is assumed to be equal for the two grains, *n* is the stress exponent, *Y* is the reference strength, e.g., yield stress. Using Eq. (41), and considering the equilibrium stress rate (Assumption 3) and strain rate (Assumption 1), the following set of two equations are derived as

$$\sigma = \frac{\sigma_1 + \sigma_2}{2} \quad \text{or} \quad \dot{\sigma} = \frac{\dot{\sigma}_1 + \dot{\sigma}_2}{2} \tag{42}$$

$$\frac{\dot{\sigma}_1}{E} + \dot{\varepsilon}_0 \left(\frac{\sigma_1}{Y_1} \right)^{n_1} = \frac{\dot{\sigma}_2}{E} + \dot{\varepsilon}_0 \left(\frac{\sigma_2}{Y_2} \right)^{n_2} = \dot{\varepsilon} \tag{43}$$

To simplify the calculation, the parameters are normalized as $\hat{\sigma} = \frac{\sigma}{E}$, $\hat{Y} = \frac{Y}{E}$, and $\hat{t} = t\dot{\varepsilon}_0$, so that Eqs. (42) and (43) are rewritten in the normalized form as

$$\frac{d\hat{\sigma}_1}{d\hat{t}} + \frac{d\hat{\sigma}_2}{d\hat{t}} = 2\frac{d\hat{\sigma}}{d\hat{t}} \tag{44}$$

$$\frac{d\hat{\sigma}_1}{d\hat{t}} + \left(\frac{\hat{\sigma}_1}{\hat{Y}_1} \right)^{n_1} = \frac{d\hat{\sigma}_2}{d\hat{t}} + \left(\frac{\hat{\sigma}_2}{\hat{Y}_2} \right)^{n_2} = \frac{\dot{\varepsilon}}{\dot{\varepsilon}_0} \tag{45}$$

Equations (44) and (45) can be solved for given material parameters $\hat{Y}_1$, $\hat{Y}_2$, n_1, n_2, and a loading parameter, $\frac{d\hat{\sigma}}{d\hat{t}} = \frac{\dot{\sigma}}{E\dot{\varepsilon}_0}$. Note that plotting $\hat{\sigma}$ vs. $\begin{Bmatrix} \hat{\sigma}_1 \\ \hat{\sigma}_2 \end{Bmatrix}$ is

equivalent to plotting $\frac{\sigma}{E}$ vs. $\begin{Bmatrix}\varepsilon_1^e \\ \varepsilon_2^e\end{Bmatrix}$. Since during loading at a constant normalized loading rate, $\frac{d\hat{\sigma}}{d\hat{t}}$ = constant, Eqs. (44) and (45) are reduced to

$$\frac{d\hat{\sigma}_1}{d\hat{t}} = \frac{d\hat{\sigma}}{d\hat{t}} + \frac{1}{2}\left(\frac{2\frac{d\hat{\sigma}}{d\hat{t}}d\hat{t} - \hat{\sigma}_1}{\hat{Y}_2}\right)^{n_2} - \frac{1}{2}\left(\frac{\hat{\sigma}_1}{\hat{Y}_1}\right)^{n_1} \quad \text{for Grain 1} \tag{46}$$

which can be solved with the initial condition, $\hat{\sigma}_1(t=0)=0$. A similar equation is derived for Grain 2. Subsequently, if the stress is held constant starting from the time $\hat{t}*$, Eqs. (44) and (45) become

$$\hat{\sigma}_1(t) + \hat{\sigma}_2(t) = \text{constant} = \hat{\sigma}_1(\hat{t}*) + \hat{\sigma}_2(\hat{t}*) \tag{47}$$

$$\frac{d\hat{\sigma}_1}{d\hat{t}} = \frac{1}{2}\left(\frac{\hat{\sigma}_1^* + \hat{\sigma}_2^* - \hat{\sigma}_1}{\hat{Y}_2}\right)^{n_2} - \frac{1}{2}\left(\frac{\hat{\sigma}_1}{\hat{Y}_1}\right)^{n_1} \tag{48}$$

A model situation is simulated, taking material parameters of Y_1/E = 0.005, n_1 = 10, Y_2/E = 0.004, and n_2 = 5. The calculated elastic strain as a function of the normalized loading rate (0.002, 0.02, 0.2, and 2) is exhibited in Figure 58. The following insights regarding grain-level lattice strains could be gained from the calculations.

(a) The effect of relative grain strength (Y/E)

During loading at a constant stress rate, the grain-level load-partitioning is governed by the magnitude of the relative strength of the grains (the ratio of yield stress over Young's modulus, *Y*/*E*) for different grain orientations. From Figure 58, it is obvious that the drift of the lattice strain during a stress-hold period will

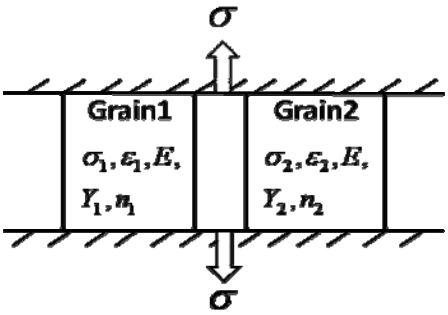

Figure 57. Schematic of the one-dimensional iso-strain model of two grains.

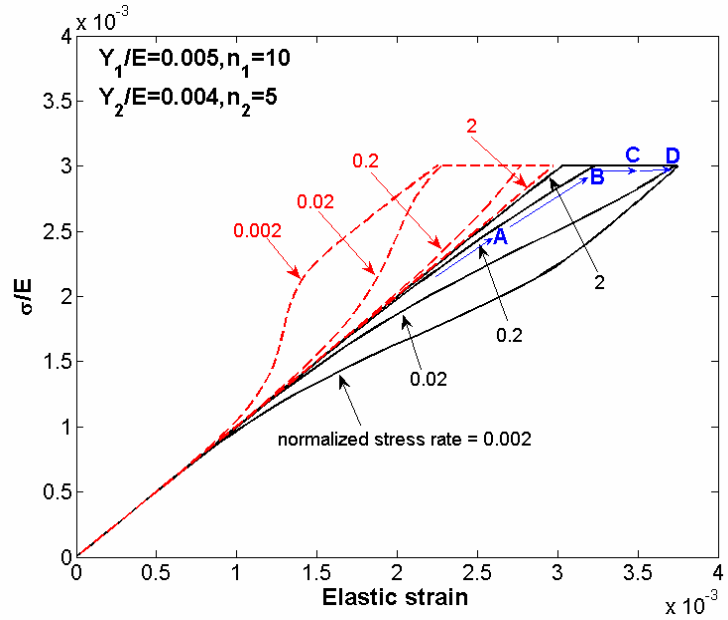

Figure 58. Elastic strain evolution at different loading rates and a subsequent constant-load creep in Grain 1 (black solid curve) and Grain 2 (red dash curve). Let's pick up black curve with a normalized loading rate of 0.2 in Grain 1. A constant loading rate is applied from O→A→B, followed by a stress holding period. Lattice strain relaxes as B→C→D during this creep period. The final state D actually corresponds to the initial lattice strain during hold on the black curve with the normalized stress rate of 0.02.

follow in opposite directions in the two grains. The direction of the drift depends on the initial "split" of the lattice strain during the loading stage. Load tends to transfer from the grain with a lower magnitude of *Y*/*E* to the grain with a higher value of *Y*/*E*, which generates a compressive intergranular stress in the soft grain (lower *Y*/*E*) and a corresponding tensile stress in the hard grain (higher *Y*/*E*).

(b) The effect of loading rate and holding time

The magnitude of the lattice-strain drift is governed by the normalized loading rate, $\frac{\dot{\sigma}}{E\dot{\varepsilon}_0}$ and the stress-holding time. Qualitatively, it can be seen that a fast loading and a long hold result in a significant amount of the elastic-strain "relaxation". For instance, we pick up the black curve with a normalized loading rate of 0.2 for Grain 1 in Figure 58. A constant loading rate is applied from O→A→B, followed by a stress holding period. The lattice-strain relaxation follows the route of B→C→D during this creep period. The final state, D, actually is equivalent to the initial lattice strain during a stress hold, with a slower loading rate of 0.02. In addition, it is observed from the calculation that the lattice-strain drifting is transient in the early stage of the stress holding, followed by a constant value as the holding time increases.

The temporal evolution of the (hkl) plane-specific lattice strain during creep measured by ND appears to be in agreement with the trends for the above mentioned modeling results. The (200) oriented grains are experimentally observed to accumulate tensile lattice strains [see Figure 53(a) and Section 5.5.3] and share the load from the neighboring grains, which is consistent with the

calculations, since (200) oriented grains show a maximal value of Y/E. Similar to the model prediction, the lattice-strain drifting in (200) and (310) oriented grains is transient within the primary creep regime [see Figure 53(a) and Section 5.5.3], followed by constant lattice strains during secondary and tertiary creep regimes. Although a concurrent decrease in other (hkl) lattice strains is not obvious from the limited resolution of the ND data, the difference among the different (hkl) plane-specific lattice strains during constant-load creep is clearly apparent.

5.6.3 Tensile Creep Mechanisms at 973 K

The stress dependence of the macroscopic creep behavior is studied to identify the creep mechanism and the precipitate strengthening caused by the resistance to dislocation motion. A stress exponent, n, of 4 and the homologous temperature of 0.56 (T/T_m where T is the creep temperature of 973 K, and T_m is the melting temperature of 1,723 K) as shown in Figure 49 provide evidence for power-law creep mechanisms in the Fe-based matrix, during which the diffusion-controlled dislocation climb is the dominant rate-controlling mechanism. This trend is consistent with the findings of previous studies on the same alloy system [35,167]. However, a significantly higher creep rate at 150 MPa falls outside the range of the linear fit for power-law creep with the stress exponent of 4, as shown in Figure 49(b). This observation suggests that the deformation mechanism in the matrix at this stress level possibly shifts from a diffusion-controlled dislocation climb power-law creep to a thermally-activated dislocation glide mechanism (a power-law breakdown) [182-183]. It is generally accepted that under high

stresses when power-law breakdown occurs, the creep-stress exponent becomes larger than the corresponding value for power-law creep. Although only a single data point for creep is measured at stress levels ≥ 150 MPa, it is indeed striking that the creep rate at 150 MPa is higher by almost an order of magnitude than the fitted line representing the stress dependence at low stresses [see Figure 49(b)]. The following discussion provides further support for the transition to a thermally-activated dislocation glide at higher stress levels. Firstly, it is reported that the transition from the power-law creep to power-law breakdown occurs at a distinct ratio between the minimal creep rate, $\dot{\varepsilon}$, and diffusion coefficient, *D*: $\dot{\varepsilon}/D \approx 10^{-13} m^{-2}$ [184-185]. Taking a self-diffusion coefficient of bcc Fe with $D = 2 \times 10^{-18}$ m^2/s, the creep rate at the transition is calculated to be approximately 2×10^{-5}/s, which compares favorably with the initial creep rate of 2.2×10^{-5}/s at 150 MPa. Secondly, the stress level of 150 MPa is close to the critical stress at which transition from the power-law creep to power-law breakdown is observed for heat-resistant ferritic steels (see Figure 59, the deformation mechanism map of ferritic Cr-Mo steels [183]). Substantial acceleration of texture evolution at 150 MPa, as described in Section 5.5.4, further indicate a greater contribution of the dislocation glide to the macroscopic creep rate. Overall, these evidence support that the creep mechanism in the matrix transits from power-law creep at 107 MPa to power-law breakdown at 150 MPa.

The precipitates strengthening effects with respect to their resistance to the dislocation motion can be studied by the threshold-stress term, σ_{th}, in Eq.

(25). The experimentally-observed threshold stress can be correlated to dislocation-particle interactions, based on theories of dislocation looping, dislocation local climb, general climb, and dislocation detachment. Among these mechanisms, dislocation detachment may be ruled out for the studied alloy, as it applies only to incoherent particles. An upper bound of a threshold stress is associated with a dislocation-looping mechanism, and is given by the Orowan stress, when dislocations bypass particles by bowing out on the glide plane. Using Eq.(26) and taking v = 0.32, b = 0.2514 nm, G = 46.1 GPa, r = 65 nm, f = 0.18, the calculated Orowan stress is equal to 188.7 MPa. The ratio of the observed threshold stress (46.1 Mpa) to the calculated Orowan stress (188.7 MPa) is ~ 0.24. The ratio of the threshold stress to Orowan stress is 0.3 ~ 0.5 for the dislocation local climb mechanism, while it is approximately an order of magnitude lower for the general climb [131]. It can therefore be concluded that dislocation local climb over particles is the dominant strengthening mechanism for dislocation-precipitate interactions during tensile creep, which shows agreement with the observed dislocation climbing over particles by TEM characterization on the compressive crept samples as described in Section 4.3.4.

5.6.4 Temperature Dependence on Deformation Micromechanisms

The present research of lattice strain evolution during in-situ tension and creep studied by neutron diffraction actually reveal the fingerprints for the different deformation mechanisms at different regimes such as low temperature/high stress levels and high temperature/low stress regimes. A

deformation mechanism map of 1% Cr-Mo-V ferritic steel [183] (material similar to the presently studied ferritic alloys) is illustrated in Figure 59, as a reference for possible deformation mechanisms in the alloys. At low temperature and high stress levels, deformation mechanism is dominated by dislocation slip. The experimental observations are summarized as below:

(1) The magnitudes of the different types of lattice strains are comparable to that of the macroscopic strain below 773 K;

(2) Intergranular strains are accumulated due to the plastic anisotropy of the grains in a polycrystalline matrix and geometric constraints imposed by the presence of grain boundaries;

(3) Interphase load transfer from the matrix to the precipitate phase is remarkable after plastic yielding of most grains;

(4) Precipitate peak broadening occurs concurrently with the accumulation of interphase lattice strains.

In contrast, at higher temperatures and lower levels of applied stress, deformation mechanism changes to the power law creep. The macroscopic plastic strain is still principally contributed by dislocation glide inside the differently oriented grains. However, the plastic deformation is rate dependent and the rate controlling factor is diffusion assisted dislocation climb process inside the grains. The experimental observations are summarized as below:

(1) The magnitudes of the different types of (hkl) lattice strains are much lower than that of the macroscopic strain above 873 K at high stress levels;

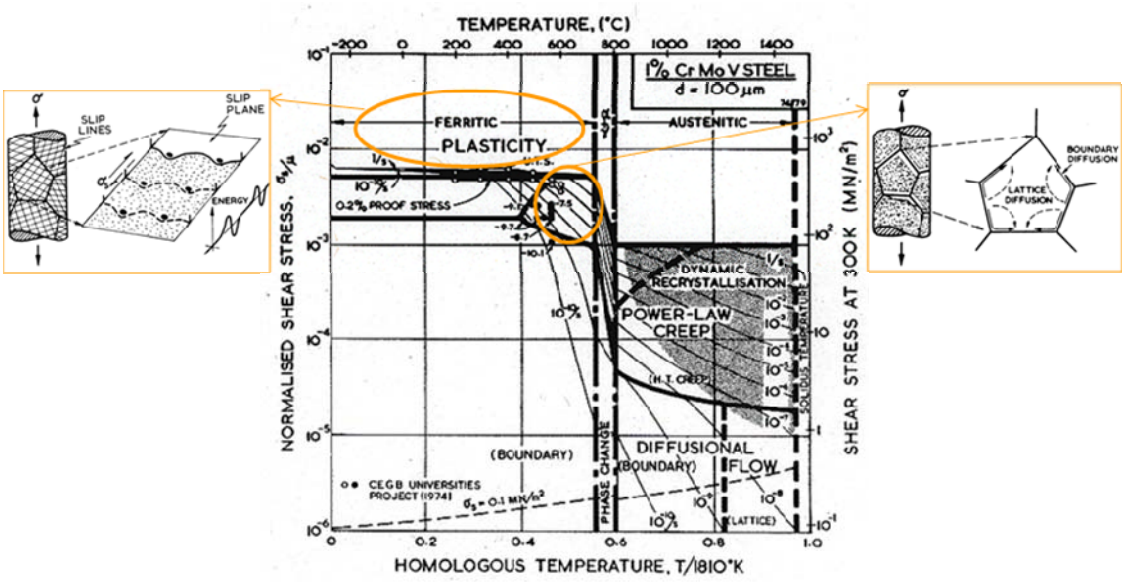

Figure 59. Deformation mechanism map of 1% Cr-Mo-V steel [183]. The circles highlight the dominant mechanism of dislocation slip at low temperature and high stress levels, and power-law creep at high temperature and low stress levels.

(2) Intergranular and interphase load transfers are not as substantial as during plastic deformation at lower temperatures.

(3) There is no evidence of precipitate peak broadening within the plastic regime.

These significant findings suggest that the geometric constrains imposed by grain boundaries become very weak at high temperatures and the possibility of grain boundary sliding and/or diffusional flow along grain boundary increases, which largely relax the accumulation of intergranular strains. Similarly, diffusional flow along the matrix-precipitate interface can also relax the interphase strain, which leads to the lowering of load transfer from the matrix to the precipitate phase. Therefore, the absence or insufficient generation of intergranular and interphase strains at high temperatures and under low stress levels suggests that plastic deformation above 873 K is assisted by grain boundary sliding, and/or diffusional flow along the grain boundaries and the interphase boundaries.

5.6.5 Comparison between CPFEM and Experimental Results

The intragranular local phase strains predicted by CPFEM are shown in Figure 60, in comparison to the experimental measurements during in-situ tension at 773 K. The input material parameters with the best fitting are listed in Table 11. The slip system we considered in the simulation is {110} slip planes and <111> slip directions, as the primary slip system for bcc materials. Quantitative agreement within the elastic deformation regime at 773 K is good. The elastic-plastic transition and subsequent load transfer from the matrix to the

precipitate are well captured by the model. However, only qualitative agreement is obtained for plastic deformation above applied tensile stress of 600 MPa. The saturation of (hkl) lattice strains in the matrix and substantial load transfer to the precipitate doesn't match perfectly with neutron diffraction measurements. The predicted compressive/tensile lattice strains accumulated in the matrix/precipitate are lower as compared to experimental results.

If we revisit Figure 27 which shows the macroscopic stress-strain behavior during quasi-static tension at 773 K, it is obvious that creep is severe over a time period of 40 minutes with an applied stress level above 600 MPa, during which neutron diffraction data were collected. As described by the iso-strain two-grain model in Section 5.6.2, lattice drifting occurs during constant stress hold and the drifting direction is compressive for soft grain/phase and tensile for hard grain/phase. Therefore, it is expected that the average lattice strain for the β′ phase during long-time stress hold will be higher than the strain without stress hold. Based on this insight, we then include the creep effects for the lattice strain evolution above 773 K. The modified model shows improvements in fitting the experimental data, as shown in Figure 50(b). In particular, the difference between the measured data and the predicted average precipitate lattice strains during stress hold at 600 and 660 MPa becomes smaller. The lattice strain drifting in both phases appears to split in opposite directions as expected, which is consistent with the results from the one dimensional model described in Section 5.6.2. However, the lattice strain saturation in the matrix is still not satisfactorily predicted.

Table 11. Input material parameters of β and β′ phases for simulating the lattice strain evolution during tension at 773 K.

	C_{11} (GPa)	C_{12} (GPa)	C_{44} (GPa)	τ_0 (MPa)	τ_s (MPa)	N	H_0	q
β	198	164	98	150	157	10	100	1.0
β′	190	165	106	500	800	10	100	1.0

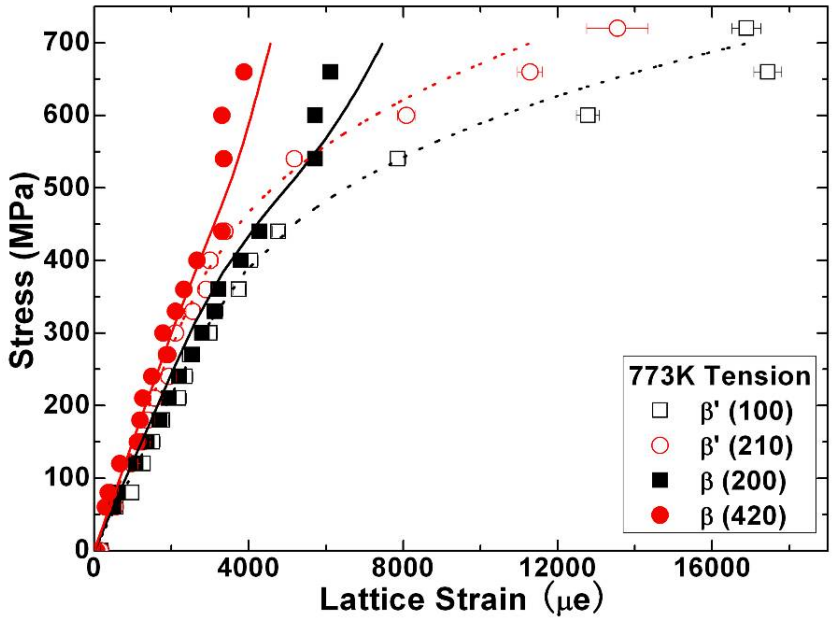

(a)

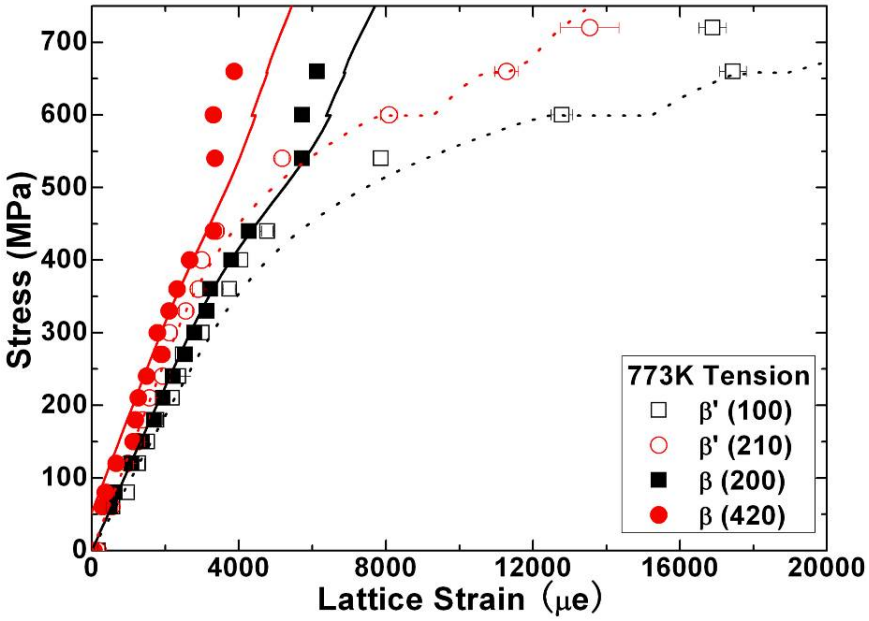

(b)

Figure 60. Simulated lattice strain evolution by CPFEM through (a) continuous loading, and (b) continuous loading and stress hold at 600 and 660 MPa which considers the creep effects during stress hold. Measured intragranular phase strains inside (200) and (420) oriented grains are also plotted for comparison.

5.7 Summary

In-situ tension and creep experiments studied by neutron diffraction provide insights into the deformation micromechanisms at elevated temperatures.

The following micromechanisms could be determined for creep deformation in the (Ni,Fe)Al-strengthened ferritic superalloy at 973 K from macroscopic-strain measurements and in-situ ND. At a low stress level of 107 MPa, the material undergoes power-law creep, which is dominated by dislocation climb as the rate-controlling factor. The β and β´ average phase strains and lattice misfit remain essentially constant during the primary and secondary creep regimes. However, load transfer occurs at the intergranular level along the axial direction during the primary creep, with increased load sharing by the (200) and (310) oriented grains. The experimentally-observed grain-level lattice strain evolution is in agreement with the predictions of an iso-strain two-grain model, which indicates a transient increase in the lattice strains during primary creep. At a high stress level of 150 MPa, the creep-deformation mechanism shifts to a power-law breakdown regime and deformation is governed by thermally-activated dislocation glide, along with an accelerated development of (110) grain orientation texture along the axial direction. During this regime, load is transferred from the plastically-deformed matrix to the elastically-deformed precipitates.

In-situ neutron diffraction experiments during tension provide fingerprints for the deformation micromechanisms at elevated temperatures. Under

dislocation slip mechanism at high stress levels and low temperatures (below 873 K), intergranular and interphase load transfer from matrix to precipitates are effective in the plastic regime. The superposition of the intragranular local phase strain on the (hkl) plane-specific lattice strain has been clearly revealed by neutron diffraction. Precipitate peak broadening is observed during plastic regime, which is possibly associated with the misorientation of the precipitates subsequent to dislocation climb bypassing the precipitates. Under power-law creep mechanism at low stresses and high temperatures (above 873 K), the lack of apparent intergranular and interphase load transfers in the plastic regime suggests that deformation is assisted by grain boundary sliding or diffusional flow along matrix-precipitate interface that largely relax the intergranular and interphase lattice strains. Crystal-plasticity finite-element simulations show qualitative agreement with neutron diffraction measurements.

CHAPTER VI
CONCLUSIONS AND RECOMMENDATIONS

Combined computational and experimental techniques have been utilized to investigate the structure-property relationships and deformation micromechanisms of newly-designed ferritic superalloys. The alloys are strengthened by coherent ordered NiAl precipitates, and show good creep and coarsening resistance for potential applications in ultra-supercritical steam turbines.

The first-principles method has been applied to calculate Fe self-diffusivity, and impurity diffusivities for various transition element solutes in bcc Fe. The current computational study is motivated by the need for identifying the slow diffusing solutes in the bcc Fe matrix that is desirable for the optimization of coarsening and creep resistance. Calculated and measured self and impurity diffusivities are found to agree with the available experimental data, within a factor of five over a temperature range of 800 to 1184 K. The results from first-principle calculations show that all the solutes have lower diffusion activation energies and, therefore, higher diffusivities as compared to Fe self-diffusion. For W the calculated impurity-diffusion coefficient is comparable to and larger than the Fe self-diffusivity in the paramagnetic and ferromagnetic phases, respectively. The accuracy of the results obtained in this study suggests that the proposed computational approach should provide a useful tool to aid in the development of kinetic databases for such alloy-design efforts.

Experimentally, the effects of Al on the precipitate attributes and compressive creep properties have been studied in model ferritic superalloys with varying amounts of Al, in order to establish the baseline information of composition-structure-property relationships. The precipitate size, spacing, and volume fraction have been quantified by synchrotron-based ultra small angle X-ray scattering in conjunction with transmission electron microscopy. As the amount of Al increases from 4 to 10 wt.% in the alloys, ~ 40% decrease in the average inter-particle spacing and ~ 30% reduction of the particle diameter were observed. The effect of Al on the precipitate size is discussed with respect to the precipitation nucleation and coarsening behavior. The alloy with the optimal creep resistance has been identified as the alloy containing 6.5 wt.% Al. Orowan looping and dislocation climb are detected by TEM as the dislocation-particle interaction modes. The magnitude of the Orowan stress, governed by the particle radius and volume fraction, suggests a correlation between microstructure and creep properties. A maximal Orowan stress associated with the optimal creep resistance in FBB6.5 alloy implies an optimal precipitate configuration that provides a strong resistance to dislocation motion.

In addition, in-situ neutron diffraction studies have been performed on the optimal creep-resistant alloy with the aim to gain insight into the deformation micromechanisms at elevated temperatures. Intergranular and interphase load transfers during high-temperature tension and creep are clearly revealed from neutron diffraction experiments. From the measured (hkl) lattice strains and peak-profile changes, we are able to interpret the crucial information of

deformation micromechanisms at elevated temperatures. Under the dislocation-slip mechanism (below 873 K), intergranular and interphase load transfers from the matrix to precipitates are effective in the plastic regime, with corresponding peak broadening in the precipitate phase. Under power-law creep mechanisms (above 873 K), the lack of apparent intergranular and interphase load transfers suggests that plastic deformation is assisted by grain-boundary sliding or diffusional flow along the matrix-precipitate interface that largely relaxes the intergranular and interphase lattice strains. Crystal-plasticity finite-element simulation shows qualitative agreement with neutron diffraction measurements. Futher improvement in finite-element simulation results are achieved after the creep effect on the lattice-strain drifting is incorporated in the model.

The major conclusions in this work as summarized above are focused on the bulk material and mechanical behavior at elevated temperatures up to 973 K. The following topics will be recommended as future work, to further explore the potential structural application of ferritic superalloys at elevated temperatures. Completion of these works will lead to a crucial understanding of the structure-property relationships at higher temperatures and lower stresses, before a decision on the detailed structural components can be made for USC steam turbine applications.

(1) Calculation of diffusivities in non-dilute alloying system using first principles in conjunction with kinetic Monte Carlo method, and prediction of the solute diffusivities as a function of element concentration;

(2) Mechanical properties (creep, tension, and thermal fatigue) above 973 K, especially the creep property at stress levels close to 35 MPa;

(3) Characterization of the matrix-precipitate interface and grain boundaries as a function of temperature and stress using in-situ TEM or high-resolution TEM;

(4) Detailed microstructure and dislocation characterizations using TEM in the creep deformed samples as a function of temperature, stress, and creep time;

(5) Development of a creep model which incorporates temporal evolution of microstructures that affect the creep resistance (e.g., precipitate coarsening) to quantitatively predict the long-term creep behavior at low stresses;

(6) Oxidation and steam corrosion behavior at and above 973 K;

(7) Exploration of other neutron/synchrotron X-ray techniques and/or new interpretation ways to boost the material information that can be directly or indirectly obtained from scattering methods.

LIST OF REFERENCES

[1] Wright IG. Materials issues for turbines for operation in ultra-supercritical steam. Proceedings of the 29th Internat. Conf. on Coal Utilization and Fuel Systems. Clearwater, FL: Coal Technology Association, 2003.
[2] Steinmet P, Wright IG, Galeri A, Monceau D, Mathieu S. Steam oxidation of advanced steam turbine alloys. Materials Science Forum 2008;595-598:299.
[3] Bhadeshia H. Design of ferritic creep-resistant steels. ISIJ Int. 2001;41:626.
[4] Hagen IV, Bendick W. Creep resistant ferritic steels for power plants. Proceedings of the International Symposium on Niobium. Orlando, FL, 2002. p.753.
[5] Eleno L, Frisk K, Schneider A. Assessment of the Fe-Ni-Al system. Intermetallics 2006;14:1276.
[6] Blavette D, Martin C, Gallot J. Atomic probe analysis of precipitates in a FeCr20Ni2Al2 alloy. Scripta Metallurgica 1982;16:59.
[7] Bradley AJ. Microscopical studies on the Iron-Nickle-Aluminum system 1. alpha + beta-alloys and isothermal sections of the phase equilibrium diagram. Journal of the Iron and Steel Institute 1949;163:19.
[8] Bradley AJ. Microscopical studies on the Iron Nickle Aluminum system 2. the breakdown of the body-centered cubic lattice. Journal of the Iron and Steel Institute 1951;168:233.
[9] Bradley AJ. Microscopical studies on the Iron-Nickle-Aluminum system 3. transformations of the beta-phase and beta'-phase. Journal of the Iron and Steel Institute 1952;171:41.
[10] Miller MK, Hetherington MG. Atom probe analysis of beta' precipitation in a model Iron-based Fe-Ni-Al-Mo superalloy. Journal De Physique 1989;50:C8425.
[11] Seetharaman V, Sundararaman M, Krishnan R. Precipitation hardening in a PH-13-8-Mo stainless-steel. Materials Science and Engineering 1981;47:1.
[12] Yukawa N, Mizutani M, Saka H. Transmission electron microscopic observation of age-hardened structures of 17-7PH stainless steel. Transactions of the Iron and Steel Institute of Japan 1969;9:254.
[13] Yukawa N, Mizutani M, Saka H. Effect of Aluminum upon phase chnages and age-hardening behaviors in 17-7PH stainless steel. Transactions of the Iron and Steel Institute of Japan 1969;9:245.
[14] Guo Z, Sha W, Vaumousse D. Microstructural evolution in a PH13-8 stainless steel after ageing. Acta Mater. 2003;51:101.
[15] Taillard R. Twinning in 19-wt-percent Chromium steels hardened by the precipitation of the intermetallic compound NiAl. Scripta Metallurgica 1982;16:49.
[16] Taillard R. Discontinuous precipitation of an NiAl intermetallic compound in a 19-wt-percent Chromiium steel. Scripta Metallurgica 1982;16:29.

[17] Taillard R, Pineau A. Room-temperature tensile properties of Fe-19wt-percent-Cr alloys precipitation hardened by the intermetallic compound NiAl. Materials Science and Engineering 1982;56:219.
[18] Taillard R, Pineau A, Thomas BJ. The precipitation of the intermetallic compound NiAl in Fe-19wt-percent-Cr. Materials Science and Engineering 1982;54:209.
[19] Calderon H. Oswald ripening of NiAl precipitates in Fe base Ni-Al-Mo alloys. Materials Science & Engineering, vol. Ph.D.: Ph.D. thesis, Northwestern University, 1986.
[20] Calderon H, Fine ME. Coarsening kinetics of coherent NiAl-type precipitates in Fe-Ni-Al-Mo alloys. Materials Science and Engineering 1984;63:197.
[21] Calderon HA, Fine ME, Weertman JR. Coarsening and morphology of beta'-precipitates in Fe-Ni-Al-Mo ferritic alloys. Metallurgical Transactions a-Physical Metallurgy and Materials Science 1988;19:1135.
[22] Calderon HA, Weertman JR, Fine ME. Effect of cyclic plastic-deformation on elevated-temperature ostwald ripening of an alloy with coherent precipitates. Scripta Metallurgica 1984;18:587.
[23] Calderon HA, Zedalis MS, Weertman JR, Fine ME. Variation of lattice-parameter misfit with particle-size in Fe-Ni-Al-Mo and Al-Zr-V alloys. Journal of Metals 1985;37:A82.
[24] Kolesar SC. Precipitation processes in Fe-base ferritic NiAl alloys. Materials Science & Engineering, vol. Ph.D.: Northwestern University, 1971.
[25] Jung I, Sauthoff G. Creep-behavior of the intermetallic B2 phase (Ni,Fe)Al with strengthening soft precipitates. Z. Metallk. 1989;80:484.
[26] Teng ZK, Liu CT, Ghosh G, Liaw PK, Fine ME. Effects of Al on the microstructure and ductility of NiAl-strengthened ferritic steels at room temperature. Intermetallics 2010;18:1437.
[27] Teng ZK, Miller MK, Ghosh G, Liu CT, Huang S, Russell KF, Fine ME, Liaw PK. Characterization of nanoscale NiAl-type precipitates in a ferritic steel by electron microscopy and atom probe tomography. Scr. Mater. 2010;63:61.
[28] Chumak I, Richter KW, Ipser H. The Fe-Ni-Al phase diagram in the Al-rich (> 50 at% Al) corner. Intermetallics 2007;15:1416.
[29] Zhang LJ, Du Y, Xu HG, Tang CY, Chen HL, Zhang WQ. Phase equilibria of the Al-Fe-Ni system at 850 degrees C and 627 degrees C. J. Alloy. Compd. 2008;454:129.
[30] Stallybrass C, Sauthoff G. Ferritic Fe-Al-Ni-Cr alloys with coherent precipitates for high-temperature applications. Materials Science and Engineering A 2004;387:985.
[31] Jung I, Sauthoff G. Dependence of creep on the distribution of strengthening precipitates. Strength of Metals and Alloys: Proc. 7th Int. Conf. Strength of Metals and Alloys, McQueen, H.J. et al. (eds.), Pergamon Press, Montreal 1985;7:731.

[32] Rawers JC, Mattlin EM. Oxidation of Fe-7Cr-12Ni-(0-6)Al-(0-7)Si alloys. Metallurgical Transactions a-Physical Metallurgy and Materials Science 1987;18:1805.
[33] Jung I, Sauthoff G. The effect of ordered precipitates on creep in ferritic Fe-Ni-Al alloys. Creep and Fracture of Engineering Materials and Structures: proceedings of the Third International Conference held at University College, Swansea, B. Wilshire, R.W. Evans (eds.), The institute of Metals, London 1987:257.
[34] Stallybrass C, Schneider A, Sauthoff G. The strengthening effect of (Ni,Fe)Al precipitates on the mechanical properties at high temperatures of ferritic Fe-Al-Ni-Cr alloys. Intermetallics 2005;13:1263.
[35] Zhu SM, Tjong SC, Lai JKL. Creep behavior of a beta '(NiAl) precipitation strengthened ferritic Fe-Cr-Ni-Al alloy. Acta Mater. 1998;46:2969.
[36] Turchi PEA, Abrikosov IA, Burton B, Fries SG, Grimvalle G, Kaufman L, Korzhavyi P, Manga VR, Ohno M, Pisch A, Scott A, Zhang WQ. Interface between quantum-mechanical-based approaches, experiments, and CALPHAD methodology. Calphad 2007;31:4.
[37] Ruban AV, Abrikosov IA. Configurational thermodynamics of alloys from first principles: effective cluster interactions. Rep. Prog. Phys. 2008;71.
[38] Van de Walle A, Ghosh G, Asta M. In: Bozzolo G, Noebe RD, Abel P, editors. Applied Computational Materials Modeling. New York: Springer, 2007. p.1.
[39] Fahnle M, Drautz R, Lechermann F, Singer R, Diaz-Ortiz A, Dosch H. Thermodynamic properties from ab-initio calculations: New theoretical developments, and applications to various materials systems. Phys. Status Solidi B-Basic Solid State Phys. 2005;242:1159.
[40] Liu ZK. First-Principles Calculations and CALPHAD Modeling of Thermodynamics J. Phase Equilib. Diffus. 2009;30:517.
[41] van de Walle A. Multicomponent multisublattice alloys, nonconfigurational entropy and other additions to the Alloy Theoretic Automated Toolkit. Calphad 2009;33:266.
[42] Kattner UR, Campbell CE. Modelling of thermodynamics and diffusion in multicomponent systems. Mater. Sci. Technol. 2009;25:443.
[43] Lukas HL, Fries SG, Sundman B. Computational thermodynamics: the CALPHAD method. Cambridge: Cambridge University Press 2007.
[44] Ghosh G, Olson GB. Integrated design of Nb-based superalloys: Ab initio calculations, computational thermodynamics and kinetics, and experimental results. Acta Mater. 2007;55:3281.
[45] Wolverton C, Yan XY, Vijayaraghavan R, Ozolins V. Incorporating first-principles energetics in computational thermodynamics approaches. Acta Mater. 2002;50:2187.
[46] Becquart CS, Domain C. Ab initio contribution to the study of complexes formed during dilute FeCu alloys radiation. Nucl. Instrum. Methods Phys. Res. Sect. B-Beam Interact. Mater. Atoms 2003;202:44.

[47] Domain C, Becquart CS. Ab initio calculations of defects in Fe and dilute Fe-Cu alloys. Phys. Rev. B 2002;65.
[48] Domain C, Becquart CS. Diffusion of phosphorus in alpha-Fe: An ab initio study. Phys. Rev. B 2005;71.
[49] Domain C, Becquart CS, Foct J. Ab initio study of foreign interstitial atom (C, N) interactions with intrinsic point defects in alpha-Fe. Phys. Rev. B 2004;69.
[50] Gong X-F, Yang GX, Fu YH, Ming C, Xie YQ, Zhuang J, Ning X-J. Solute diffusion in the [gamma]' phase of Ni based alloys. Comput. Mater. Sci. 2009;47:232.
[51] Janotti A, Krcmar M, Fu CL, Reed RC. Solute diffusion in metals: Larger atoms can move faster. Phys. Rev. Lett. 2004;92.
[52] Krcmar M, Fu CL, Janotti A, Reed RC. Diffusion rates of 3d transition metal solutes in nickel by first-principles calculations. Acta Mater. 2005;53:2369.
[53] Mantina M, Wang Y, Chen LQ, Liu ZK, Wolverton C. First principles impurity diffusion coefficients. Acta Mater. 2009;57:4102.
[54] Sandberg N, Henriksson KOE, Wallenius J. Carbon impurity dissolution and migration in bcc Fe-Cr: First-principles calculations. Phys. Rev. B 2008;78.
[55] Simonovic D, Sluiter MHF. Impurity diffusion activation energies in Al from first principles. Phys. Rev. B 2009;79.
[56] Van der Ven A, Ceder G. First principles calculation of the interdiffusion coefficient in binary alloys. Phys. Rev. Lett. 2005;94.
[57] Wong KL, Lee HJ, Shim JH, Sadigh B, Wirth BD. Multiscale modeling of point defect interactions in Fe-Cr alloys. J. Nucl. Mater. 2009;386:227.
[58] Choudhury S, Barnard L, Tucker JD, Allen TR, Wirth BD, Asta M, Morgan D. Ab-initio based modeling of diffusion in dilute bcc Fe-Ni and Fe-Cr alloys and implications for radiation induced segregation. J. Nucl. Mater. 2011;411:1.
[59] Sandberg N, Holmestad R. First-principles calculations of impurity diffusion activation energies in Al. Phys. Rev. B 2006;73.
[60] Anand MS, Agarwala RP. Diffusion of copper in iron. J. Appl. Phys. 1966;37:4248.
[61] Graham D, Tomlin DH. Self-diffusion in iron. Philosophical Magazine 1963;8:1581.
[62] Gruzin PL. Diffuziya kobalta, khroma I volframa V zheleze I stali. Doklady Akademii Nauk Sssr 1954;94:681.
[63] Ham JL. The rate of diffusion of molybdenum in austenite and in ferrite. Transactions of the American Society for Metals 1945;35:331.
[64] Heijwege.Cp, Rieck GD. Diffusion in Mo-Ni, Mo-Fe and Mo-Co systems. Acta Metallurgica 1974;22:1269.
[65] Hirano K, Cohen M. Diffusion of cobalt in iron-cobalt alloys. Transactions of the Japan Institute of Metals 1972;13:96.

[66] Huntz AM, Aucoutur.M, Lacombe P. Volumetric and intergranular measurement of diffusion coefficients of radioactive chromium in alpha iron. Comptes Rendus Hebdomadaires Des Seances De L Academie Des Sciences Serie C 1967;265:554.
[67] James DW, Leak GM. Self-diffusion and diffusion of cobalt in alpha and delta-iron. Philosophical Magazine 1966;14:701.
[68] Kirkaldy JS, Smith PN, Sharma RC. Diffusion of manganese in paramagnetic bcc iron. Metallurgical Transactions 1973;4:624.
[69] Klugkist P, Herzig C. Tracer diffusion of titanium in alpha-iron. Phys. Status Solidi A-Appl. Res. 1995;148:413.
[70] Manayenkov VP, Lazarev VA, Kulemin AV, Golikov VM. Diffusion of carbon and chromium into iron under effect of ultrasonic vibration. Russ. Metall. 1977:99.
[71] Mortlock AJ, Ewens PM. Anisotropic diffusion of nickel in zinc studied by an autoradiographic method. Physical Review 1967;156:814.
[72] Obrtlik K, Kucera J. Diffusion of vanadium in the Fe-V system. Phys. Status Solidi A-Appl. Res. 1979;53:589.
[73] Pavlinov LV, Isadzhan.Ya, Smirnov VP. Diffusion of chromium in alloys of iron with vanadium and chromium. Physics of Metals and Metallography-Ussr 1968;25:206.
[74] Perez RA, Torres DN, Dyment F. Sb diffusion in alpha-Fe. Appl. Phys. A-Mater. Sci. Process. 2005;81:787.
[75] Richter I, Fellerkniepmeier M. Diffusion of Zn in alpha-Fe single-crystals. Phys. Status Solidi A-Appl. Res. 1981;68:289.
[76] Totemeier T, Gale W. Smithells Metals Reference Book: Butterworth-Heinemann Co. Ltd. , 2004.
[77] Treheux D, Marchive D, Delagran.J. Determination of heterodiffusion coefficients with infinite dilution of Tin in alpha-iron. Comptes Rendus Hebdomadaires Des Seances De L Academie Des Sciences Serie C 1972;274:1260.
[78] Alberry P, Haworth C. Met. Sci. 1974;8:407.
[79] Arita M, Ohyama M, Goto KS, Someno M. Measurements of activity, solubility, and diffusivity in alpha and gamma Fe-Sn alloys between 1183-K and 1680-K. Z. Metallk. 1981;72:244.
[80] Borg RJ, Birchenall CE. Self-diffusion in alpha iron. Transactions of the American Institute of Mining and Metallurgical Engineers 1960;218:980.
[81] Borisov VT, Golikov VM, Sherbedi.Gv. Diffusion of molybdenum in iron and an iron-molybdenum alloy. Physics of Metals and Metallography 1966;22:175.
[82] Buffington FS, Hirano K, Cohen M. Self diffusion in iron. Acta Metallurgica 1961;9:434.
[83] Geise J, Herzig C. Impurity diffusion of vanadium and self-diffusion in iron. Z. Metallk. 1987;78:291.
[84] Hettich G, Mehrer H, Maier K. Self-diffusion in ferromagnetic alpha-iron. Scripta Metallurgica 1977;11:795.

[85] Iijima Y, Kimura K, Hirano K. Self-diffusion and isotope effect in alpha-iron. Acta Metallurgica 1988;36:2811.
[86] Kieszniewski J. Pr. Inst. Hutn. 1967;19:252.
[87] Kucera J, Million B, Ciha K. Koveve Mater. 1969;7:97.
[88] Kucera J, Million B, Ruzickov.J, Foldyna V, Jakobova A. Self-diffusion of iron in alpha-phase of iron and Fe-Cr alloys. Acta Metallurgica 1974;22:135.
[89] Lubbehusen M, Mehrer H. Self-diffusion in alpha-iron - the influence of dislocations and the effect of the magnetic phase-transition. Acta Metall. Mater. 1990;38:283.
[90] Nitta H, Yamamoto T, Kanno R, Takasawa K, Iida T, Yamazaki Y, Ogu S, Iijima Y. Diffusion of molybdenum in alpha-iron. Acta Mater. 2002;50:4117.
[91] Nohara K, Hirano K. J. Jpn Inst. Met. 1976;50:1053.
[92] Romig AD, Goldstein JI. The diffusivity of Ni in fe-Ni and Fe-Ni-P martensites. Metallurgical Transactions a-Physical Metallurgy and Materials Science 1981;12:243.
[93] Sato K. Diffusion of Co60 into alpha-iron. Transactions of the Japan Institute of Metals 1964;5:91.
[94] Takemoto S, Nitta H, Iijima Y, Yamazaki Y. Diffusion of tungsten in alpha-iron. Philosophical Magazine 2007;87:1619.
[95] Treheux D, Guiralde.P. Study of mutual diffusion-coefficients in alpha(FeSn) solid-solution of binary iron-Tin system. Comptes Rendus Hebdomadaires Des Seances De L Academie Des Sciences Serie C 1973;277:1299.
[96] Walter CM, Peterson NL. Isotope effect in self-diffusion in iron. Physical Review 1969;178:922.
[97] Davenport AT, Honeycomhe RWK. The Secondary Hardening of Tungsten Steels. Metal Science 1975;9:201.
[98] Le Claire AD. In: Eyring H, editor. Physical Chemistry: An Advanced Treatise, vol. 10. New York: Academic Press, 1970.
[99] Girifalco LA. Activation energy for diffusion in ferromagnetics. J. Phys. Chem. Solids 1962;23:1171.
[100] Nitta H, Iijima Y. Influence of magnetization change on solute diffusion in iron. Philos. Mag. Lett. 2005;85:543.
[101] Ruch L, Sain DR, Yeh HL, Girifalco LA. Analysis of diffusion in ferromagnets. J. Phys. Chem. Solids 1976;37:649.
[102] Hanggi P, Talkner P, Borkovec M. Reaction-rate theory - 50 years after kramers. Rev. Mod. Phys. 1990;62:251.
[103] Vineyard GH. Frequency factors and isotope effects in solid state rate processes. J. Phys. Chem. Solids 1957;3:121.
[104] Crangle J, Goodman GM. Magnetization of pure iron and nickel. Proc. R. Soc. Lond. A-Math. Phys. Sci. 1971;321:477.
[105] Potter HH. The magneto-caloric effect and other magnetic phenomena in iron. Proc. R. Soc. Lond. A-Math. Phys. Sci. 1934;146:0362.

[106] Philibert J. Atom Movements: Diffusion and Mass Transport in Solids: Les Éditions de Physique, 1991.
[107] Satta A, Willaime F, de Gironcoli S. Vacancy self-diffusion parameters in tungsten: Finite electron-temperature LDA calculations. Phys. Rev. B 1998;57:11184.
[108] Satta A, Willaime F, de Gironcoli S. First-principles study of vacancy formation and migration energies in tantalum. Phys. Rev. B 1999;60:7001.
[109] Blochl PE. Projector augmented-wave method. Phys. Rev. B 1994;50:17953.
[110] Kresse G, Joubert D. From ultrasoft pseudopotentials to the projector augmented-wave method. Phys. Rev. B 1999;59:1758.
[111] Perdew JP, Burke K, Ernzerhof M. Generalized gradient approximation made simple. Phys. Rev. Lett. 1996;77:3865.
[112] Kresse G, Furthmuller J. Efficiency of ab-initio total energy calculations for metals and semiconductors using a plane-wave basis set. Comput. Mater. Sci. 1996;6:15.
[113] Kresse G, Furthmuller J. Efficient iterative schemes for ab initio total-energy calculations using a plane-wave basis set. Phys. Rev. B 1996;54:11169.
[114] Kresse G, Hafner J. Abinitio molecular-dynamics for liquid-metals. Phys. Rev. B 1993;47:558.
[115] Ekman M, Sadigh B, Einarsdotter K, Blaha P. Ab initio study of the martensitic bcc-hcp transformation in iron. Phys. Rev. B 1998;58:5296.
[116] Methfessel M, Paxton AT. High-precision sampling for brillouin-zone intergration in metals. Phys. Rev. B 1989;40:3616.
[117] Chen Y, Fu CL, Ho KM, Harmon BN. Calculations for the transverse n-point phonons in bcc Zr, Nb, and Mo. Phys. Rev. B 1985;31:6775.
[118] Wolverton C, Ozolins V, Asta M. Hydrogen in aluminum: First-principles calculations of structure and thermodynamics. Phys. Rev. B 2004;69.
[119] Horton GK, Maradudin AAe. Dynamical Properties of Solids: Phonon Physics the Cutting Edge. New York: North-Holland, 1974.
[120] Mendelev MI, Han S, Srolovitz DJ, Ackland GJ, Sun DY, Asta M. Development of new interatomic potentials appropriate for crystalline and liquid iron. Philosophical Magazine 2003;83:3977.
[121] Jonsson H, Mills G, Jacobsen KW. Nudged elastic band method for finding minimum energy paths of transitions. In: Berne BJ, Ciccotti G, Coker DF, editors. Classical and quantum dynamics in condensed phased simulations. World Scientific, 1998. p.385.
[122] Mills G, Jonsson H, Schenter GK. Reversible work transition-state theory - application to dissociative absorption of hydrogen. Surf. Sci. 1995;324:305.
[123] Fu CC, Dalla Torre J, Willaime F, Bocquet JL, Barbu A. Multiscale modelling of defect kinetics in irradiated iron. Nat. Mater. 2005;4:68.
[124] Ohnuma T, Soneda N, Iwasawa M. First-principles calculations of vacancy-solute element interactions in body-centered cubic iron. Acta Mater. 2009;57:5947.

[125] Olsson P, Domain C, Wallenius J. Ab initio study of Cr interactions with point defects in bcc Fe. Phys. Rev. B 2007;75.
[126] Fu CC, Willaime F, Ordejon P. Stability and mobility of mono- and di-interstitials in alpha-Fe. Phys. Rev. Lett. 2004;92.
[127] Soderlind P, Yang LH, Moriarty JA, Wills JM. First-principles formation energies of monovacancies in bcc transition metals. Phys. Rev. B 2000;61:2579.
[128] Nitta H, Miura K, Iijima Y. Self-diffusion in iron-based Fe-Mo alloys. Acta Mater. 2006;54:2833.
[129] Buschow KHJ, Cahn RW, Flemings MC, Ilschnew B, Kramer EJ, Mahajan S. Encyclopedia of materials: science and technology. Amsterdam: Elsevier, 2001.
[130] Bowen AW, Leak GM. Solute diffusion in alpha-iron and gamma-iron. Metallurgical Transactions 1970;1:1695.
[131] Kassner ME. Fundamentals of Creep in Metals and Alloys: Elsevier, 2004.
[132] Ilavsky J, Jemian PR, Allen AJ, Zhang F, Levine LE, Long GG. Ultra-small-angle X-ray scattering at the Advanced Photon Source. J. Appl. Crystallogr. 2009;42:469.
[133] Ilavsky J, Jemian PR. Irena: tool suite for modeling and analysis of small-angle scattering. J. Appl. Crystallogr. 2009;42:347.
[134] Zemb T, Lindner P. Neutron, X-rays and Light. Scattering Methods Applied to Soft Condensed Matter: North Holland, 2002.
[135] Huang EW, Liaw PK, Porcar L, Liu Y, Liu YL, Kai JJ, Chen WR. Study of nanoprecipitates in a nickel-based superalloy using small-angle neutron scattering and transmission electron microscopy. Appl. Phys. Lett. 2008;93.
[136] Farsaci F, Fontanella ME, Salvato G, Wanderlingh F, Giordano R, Wanderlingh U. Dynamical behavior of structured macromolecular solutions. Phys. Chem. Liq. 1989;20:205.
[137] Porod G. In: Glatter O, Kratky O, editors. Small Angle X-ray Scattering. London: Academic Press, 1982. p.17.
[138] Stevens RA, Flewitt PEJ. The dependence of creep rate on microstructure in a gamma'-strengthened superalloy. Acta Metallurgica 1981;29:867.
[139] Williams KR, Cane BJ. Creep-behavior of 1/2Cr1/2Mo1/4V steel at engineering stresses. Materials Science and Engineering 1979;38:199.
[140] Dyson BF, Gibbons TB. Tertiary creep in nickle-based superalloys - analysis of experimental data and theoretical synthesis. Acta Metallurgica 1987;35:2355.
[141] Dyson BF, McLean M. Particle-coarsening, sigma-0 and tertiary creep. Acta Metallurgica 1983;31:17.
[142] Leckie FA, Hayhurst DR. Constitutive equations for creep-rupture. Acta Metallurgica 1977;25:1059.
[143] Terada D, Yoshida F, Nakashima H, Abe H, Kadoya Y. In-situ observation of dislocation motion and its mobility in Fe-Mo and Fe-W solid solutions at high temperatures. ISIJ Int. 2002;42:1546.

[144] Kadoya Y, Shimizu E. Effect of solute Mo, W and dispersoid carbonitride on high temperature creep of ferritic steels. Tetsu To Hagane-J. Iron Steel Inst. Jpn. 1999;85:827.
[145] Porter DA, Easterling KE. Phase Transformations in Metals and Alloys: CRC Press, 2002.
[146] Raghunathan VS, Sharma BD. Self-diffusion in concentrated Fe-Al and Fe-Si alloys. Philos. Mag. A-Phys. Condens. Matter Struct. Defect Mech. Prop. 1981;43:427.
[147] Broska A, Wolff J, Franz M, Hehenkamp T. Defect analysis in FeAl and FeSi with positron lifetime spectroscopy and Doppler broadening. Intermetallics 1999;7:259.
[148] Brown LM, Ham RK. Strengthening methods in crystals. Amsterdam: Elsevier, 1971.
[149] Martin JW. Micromechanisms in Particle-Hardened Alloys. Cambridge, U.K.: Cambridge University Press, 1980.
[150] Ghosh G, Olson GB. The isotropic shear modulus of multicomponent Fe-base solid solutions. Acta Mater. 2002;50:2655.
[151] Ruggles MB, Cheng S, Krempl E. The rate-dependent mechanical-behavior of modified 9wt-percent-Cr-1wt-percent-Mo steel at 538 degrees C. Mater. Sci. Eng. A-Struct. Mater. Prop. Microstruct. Process. 1994;186:15.
[152] Magnusson H, Sandstrom R. Influence of aluminium on creep strength of 9-12% Cr steels. Mater. Sci. Eng. A-Struct. Mater. Prop. Microstruct. Process. 2009;527:118.
[153] Miracle DB. Overview No-104 - the physical and mechanical properties of NiAl. Acta Metall. Mater. 1993;41:649.
[154] Daymond MR, Preuss M, Clausen B. Evidence of variation in slip mode in a polycrystalline nickel-base superalloy with change in temperature from neutron diffraction strain measurements. Acta Mater. 2007;55:3089.
[155] Ma S, Seetharaman V, Majumdar BS. CRSS of gamma/gamma ' phases from in situ neutron diffraction of a directionally solidified superalloy tension tested at 900 degrees C. Acta Mater. 2008;56:4102.
[156] Ma S, Brown D, Bourke MAM, Daymond MR, Majurndar BS. Microstrain evolution during creep of a high volume fraction superalloy. Mater. Sci. Eng. A-Struct. Mater. Prop. Microstruct. Process. 2005;399:141.
[157] Larson AC, Von Dreele RB. GSAS-general structure analysis system, 1994.
[158] Daymond MR, Bourke MAM, VonDreele RB, Clausen B, Lorentzen T. Use of Rietveld refinement for elastic macrostrain determination and for evaluation of plastic strain history from diffraction spectra. J. Appl. Phys. 1997;82:1554.
[159] Stone HJ, Holden TM, Reed RC. On the generation of microstrains during the plastic deformation of Waspaloy. Acta Mater. 1999;47:4435.
[160] Bower AF, Wininger E. A two-dimensional finite element method for simulating the constitutive response and microstructure of polycrystals

during high temperature plastic deformation. J. Mech. Phys. Solids 2004;52:1289.
[161] Peirce D, Asaro RJ, Needleman A. An analysis of nonuniform and localized deformation in ductile single-crystals. Acta Metallurgica 1982;30:1087.
[162] Zheng LL, Gao YF, Lee SY, Barabash RI, Lee JH, Liaw PK. Intergranular strain evolution near fatigue crack tips in polycrystalline metals. J. Mech. Phys. Solids 2011;59:2307.
[163] Gnaupel-Herold T, Brand PC, Prask HJ. Calculation of single-crystal elastic constants for cubic crystal symmetry from powder diffraction data. J. Appl. Crystallogr. 1998;31:929.
[164] Date EHF. Elastic properties of steels. Journal of the Iron and Steel Institute 1969;207:988.
[165] Wong SL, Dawson PR. Influence of directional strength-to-stiffness on the elastic-plastic transition of fcc polycrystals under uniaxial tensile loading. Acta Mater. 2010;58:1658.
[166] Gale W, Totemeier T. Smithells Metals Reference Book, 8th ed., Chapter 14: Elsevier, 2004.
[167] Tjong SC, Ma ZY. Creep behaviour of precipitation-hardened ferritic Fe-19Cr-4Ni-2Al alloy. Mater. Lett. 2002;56:59.
[168] Fukuhara M, Sanpei A. Elastic-moduli and internal-friction of low-carbon and stainless-steels as a function of temperature. ISIJ Int. 1993;33:508.
[169] Winand HMA, Whitehouse AF, Withers PJ. An investigation of the isothermal creep response of Al-based composites by neutron diffraction. Mater. Sci. Eng. A-Struct. Mater. Prop. Microstruct. Process. 2000;284:103.
[170] Allen AJ, Bourke MAM, Dawes S, Hutchings MT, Withers PJ. The analysis of internal strains measured by neutron-diffraction in Al-SiC metal matrix composites. Acta Metall. Mater. 1992;40:2361.
[171] Choo H, Seo D, Beddoes J, Bourke MAM, Brown DW. In situ neutron diffraction studies on the elevated-temperature deformation behavior of a TiAl-W alloy. Appl. Phys. Lett. 2004;85:4654.
[172] Daymond MR, Priesmeyer HG. Elastoplastic deformation of ferritic steel and cementite studied by neutron diffraction and self-consistent modelling. Acta Mater. 2002;50:1613.
[173] Oliver EC, Daymond MR, Withers PJ. Interphase and intergranular stress generation in carbon steels. Acta Mater. 2004;52:1937.
[174] Tomota Y, Lukas P, Harjo S, Park JH, Tsuchida N, Neov D. In situ neutron diffraction study of IF and ultra low carbon steels upon tensile deformation. Acta Mater. 2003;51:819.
[175] Hutchings MT, Withers PJ, Holden TM, Lorentzen T. Introduction to the Characterization of Residual Stress by Neutron Diffraction: CRC Press, 2005.

[176] Lewis SJ, Truman CE. Diffraction measurements for evaluating plastic strain in A533B ferritic steel-a feasibility study. J. Phys. D-Appl. Phys. 2010;43:265501.
[177] Engler O, Randle V. Introduction to Texture Analysis: Macrotexture, Microtexture, and Orientation Mapping: CRC press, 2009.
[178] Hosford WF. The Mechanics of Crystals and Textured Polycrystals,: Oxford University Press, 1993.
[179] Isaak DG, Masuda K. Elastic and viscoelastic properties of alpha-iron at high-temperatures. J. Geophys. Res.-Solid Earth 1995;100:17689.
[180] Dever DJ. Temperature dependence of elastic-constants in alpha-iron single-crystals - relationship to spin order and diffusion anomalies. J. Appl. Phys. 1972;43:3293.
[181] Leese J, Lord AE. Elastic stiffness coefficients of single-crystal iron from toom temperature to 500 degrees C. J. Appl. Phys. 1968;39:3986.
[182] Argon AS. Physical Metallurgy, Eds., Robert W. Cahn, Peter Haasen: Elsevier, 1996.
[183] Frost HJ, Ashby MF. Deformation Mechanism Maps: the Plasticity and Creep of Metals and Ceramics, Chapter 8. Oxford, UK: Pergamon Press, 1982.
[184] Groisbock F. Creep-behavior of a heat-resistant ferritic chromium steel in terms of stress exponents. J. Mater. Sci. 1992;27:4373.
[185] Groisbock F, Ebner R. Correlation between creep-behavior and substructure of a heat-resistant ferritic Cr-steel. Z. Metallk. 1991;82:435.
[186] Vondreele RB, Jorgensen JD, Windsor CG. Rietveld refinement with spallation neutron powder diffraction data. J. Appl. Crystallogr. 1982;15:581.

APPENDIX

A.1 Mathematical Function for Gaussian Peak Profile in GSAS

The peak profile function utilized to perform Rietveld refinement and single peak fitting on the measured neutron-diffraction patterns is the Gaussian type Time of Flight (TOF) profile function, 1, as described on Page 143 in General Structure Analysis System (GSAS) manual [157]. This function is adopted from Jorgensen and Von Dreele's published work [186] as

$$H(\Delta T) = N\left[e^{u} erfcy + e^{v} erfcz\right] \tag{A.1}$$

where ΔT is the difference in TOF between the reflection position, T_{ph}, and the profile point, T; the terms N, u, v, y, and z are dependent on the profile coefficients. The function *erfc* is the complementary error function. The profile function, Eq. (A.1), is the result of convoluting two back-to-back exponentials with a Gaussian, as

$$H(\Delta T) = \int G(\Delta T - \tau) E(\tau) d\tau \tag{A.2}$$

$$E(\tau) = \begin{matrix} 2Ne^{\alpha\tau} & \text{for } \tau < 0 \\ 2Ne^{-\beta\tau} & \text{for } \tau > 0 \end{matrix} \tag{A.3}$$

where α and β are the rise and decay coefficients for the exponentials. The Gaussian function is

$$G(\Delta T - \tau) = \frac{1}{\sqrt{2\pi\sigma^2}} \exp\left[-(\Delta T - \tau)^2 / 2\sigma^2\right] \tag{A.4}$$

These functions when convoluted give the profile function in Eq.(A.1). The normalized factor, N, and coefficients of u, v, y, z in Eq. (A.1) are functions of three coefficients, α, β, and σ^2, given by

$$N = \frac{\alpha\beta}{2(\alpha+\beta)} \tag{A.5}$$

$$u = \frac{\alpha}{2}\left(\alpha\sigma^2 + 2\Delta T\right) \tag{A.6}$$

$$v = \frac{\beta}{2}\left(\beta\sigma^2 - 2\Delta T\right) \tag{A.7}$$

$$y = \frac{\alpha\sigma^2 + \Delta T}{\sqrt{2\sigma^2}} \tag{A.8}$$

$$z = \frac{\beta\sigma^2 - \Delta T}{\sqrt{2\sigma^2}} \tag{A.9}$$

The coefficients α, β, and σ^2 show different dependencies on the reflection d-spacing as

$$\alpha = \alpha_0 + \alpha_1 / d \tag{A.10}$$

$$\beta = \beta_0 + \beta_1 / d^4 \tag{A.11}$$

$$\sigma^2 = \sigma_0^2 + \sigma_1^2 d^2 + \sigma_2^2 d^4 + \left(\sigma_{1e}^2 d^2 + \sigma_{2e}^2 d^4\right)\cos^2\Phi \tag{A.12}$$

In addition, the profile function considers the deviation of diffraction lines from their positions based on the lattice parameter, which is induced by isotropic and anisotropic strain as

$$\Delta T = \left(T - T_{ph}\right) - \varepsilon_i d - \varepsilon_a d\cos\Phi - \varepsilon_A \frac{(hk)^2 + (hl)^2 + (kl)^2}{\left(h^2 + k^2 + l^2\right)^2} \tag{A.13}$$

Thus the profile function has twelve coefficients (α_0, α_1, β_0, β_1, σ_0^2, σ_1^2, σ_2^2, σ_{1e}^2, σ_{2e}^2, ε_i, ε_a, and ε_A) that are refined by GENLES subroutine in GSAS.

A.2 Methodology for Crystal-Plasticity Finite Element Modeling

The framework of CPFEM methodology and the constitutive equations governing deformation within grains were elaborately described in the papers published by Pierce et al., Bower and Wininger, and Zheng et al [160-162]. A summary of the methodology is described as follows.

From the kinematics point of view, the total deformation gradient can be decomposed into the elastic and plastic deformation gradients as

$$F_{ij} = \partial x_i / \partial X_j = F^e_{ik} F^p_{kj} \tag{A.14}$$

where the elastic deformation gradient F^e_{ik} is related to (1) the Cauchy stress σ_{ij} by $J\sigma_{ij} = F^e_{ik} T_{kl} F^e_{jl}$ and $J = \det\left(F^e\right)$, and (2) the elastic Lagrange-Green strain through $E^e_{ij} = (1/2)\left(F^e_{ki} F^e_{kj} - \delta_{ij}\right)$. T_{ij} is the material stress tensor defined by Hook's law as $T_{ij} = C_{ijkl} E^e_{kl}$. The plastic deformation gradient F^e_{ik} follows Schmid's Law to calculate the slip in the polycrystalline grains with given sets of slip systems as

$$\dot{F}^p_{ik} F^{p-1}_{kj} = \sum_{\alpha=1}^{N_{SLIP}} \dot{\gamma}^{(\alpha)} s^{(\alpha)}_i m^{(\alpha)}_j \tag{A.15}$$

where $\dot{\gamma}^{(\alpha)}$ is the slip strain rate of the α_{th} slip system, $s^{(\alpha)}_i$ is the slip direction, $m^{(\alpha)}_j$ is the slip plane normal, and N_{SLIP} is the total number of slip systems. Power-law flow rule and the Peirce-Asaro-Needleman hardening law are utilized to determine the slip strain rate as

$$\dot{\gamma}^{\alpha} = \dot{\gamma}^0 \left(\frac{\tau^{\alpha}}{g^{\alpha}} \right)^N \tag{A.16}$$

$$\dot{g}^{\alpha} = \sum_{\beta} h_{\alpha\beta} \mid \dot{\gamma}^{\beta} \mid \tag{A.17}$$

where $\dot{\gamma}^{0}$ is the characteristic strain rate, τ^{α} is the resolved shear stress expressed by $\tau^{\alpha} = m_i^{(\alpha)} F_{ij}^{e-1} J \sigma_{jk} F_{kl}^{e} S_l^{(\alpha)}$, g^{α} is the flow strength of the slip system, *N* is the stress exponent, $h_{\alpha\beta}$ is the hardening moduli. The latent and self hardening moduli are respectively given by

$$h_{\alpha\beta} = h_{\alpha\alpha} \left[q + (1-q)\delta_{\alpha\beta} \right] \tag{A.18}$$

$$h_{\alpha\alpha} = h_0 \operatorname{sech}^2 \left| \frac{h_0 \gamma}{\tau_s - \tau_0} \right| \tag{A.19}$$

where h_0 is the initial hardening modulus, τ_0 is the initial slip strength, τ_s is the saturation slip strength, and *q* is the latent hardening coefficient. The overall slip strain γ is obtained from $\gamma = \int_0^t \sum_{\alpha} \mid \dot{\gamma}^{(\alpha)} \mid dt$.

The simulation is based on a ABAQUS user-defined material (UMAT) subroutine modified by Zheng et al. [162]. The initial input parameters for CPFEM include stiffness C_{11}, C_{12}, and C_{44} as the single crystal elastic constants for cubic materials, the stress exponent *N*, the characteristic strain rate $\dot{\gamma}^{0}$, the initial hardening modulus h_0, the initial slip strength τ_0, the saturation slip strength τ_s, and the latent hardening coefficient *q*, for both the matrix and the precipitate phases.

VITA

Shenyan Huang was born and grown up in Shanghai, China. In June 2006, she obtained a Bachelor of Science degree in Materials Science & Engineering at Shanghai Jiao Tong University. She started her graduate study at University of Tennessee – Knoxville in August 2006. She received a Master of Science degree in Materials Science & Engineering (concentrated in Metallurgy) in December 2008. In December 2011, she graduated from the University of Tennessee with Doctor of Philosophy degree in Materials Science & Engineering (concentrated in Metallurgy) and a minor in Computational Science.